Published in final edited form as:
Phys Med Biol. 2010 October 21; 55(20): R111–R191. doi:10.1088/0031-9155/55/20/R01.

Dynamic single photon emission computed tomography—basic principles and cardiac applications

Grant T Gullberg[1,4], **Bryan W Reutter**[1], **Arkadiusz Sitek**[2], **Jonathan S Maltz**[1,3], and **Thomas F Budinger**[1]

[1] E O Lawrence Berkeley National Laboratory, Berkeley, CA 94720, USA

[2] Brigham and Women's Hospital and Harvard Medical School, Boston, MA, USA

[3] Siemens Medical Solutions, Inc., Concord, CA, USA

Abstract

The very nature of nuclear medicine, the visual representation of injected radiopharmaceuticals, implies imaging of dynamic processes such as the uptake and wash-out of radiotracers from body organs. For years, nuclear medicine has been touted as the modality of choice for evaluating function in health and disease. This evaluation is greatly enhanced using single photon emission computed tomography (SPECT), which permits three-dimensional (3D) visualization of tracer distributions in the body. However, to fully realize the potential of the technique requires the imaging of *in vivo* dynamic processes of flow and metabolism. Tissue motion and deformation must also be addressed. Absolute quantification of these dynamic processes in the body has the potential to improve diagnosis. This paper presents a review of advancements toward the realization of the potential of dynamic SPECT imaging and a brief history of the development of the instrumentation. A major portion of the paper is devoted to the review of special data processing methods that have been developed for extracting kinetics from dynamic cardiac SPECT data acquired using rotating detector heads that move as radiopharmaceuticals exchange between biological compartments. Recent developments in multi-resolution spatiotemporal methods enable one to estimate kinetic parameters of compartment models of dynamic processes using data acquired from a single camera head with slow gantry rotation. The estimation of kinetic parameters directly from projection measurements improves bias and variance over the conventional method of first reconstructing 3D dynamic images, generating time–activity curves from selected regions of interest and then estimating the kinetic parameters from the generated time–activity curves. Although the potential applications of SPECT for imaging dynamic processes have not been fully realized in the clinic, it is hoped that this review illuminates the potential of SPECT for dynamic imaging, especially in light of new developments that enable measurement of dynamic processes directly from projection measurements.

Preface

Today our healthcare system is facing challenges in the diagnosis and therapy of cardiovascular disease, cancer and mental disease, which affect all segments of our population. Single photon emission computed tomography (SPECT) continues to be an important tool in the clinical diagnosis of these diseases. It is the number one protocol for clinical evaluation of cardiovascular myocardial ischemia (seriously compromised blood flow) and viability (live tissue with reduced flow).

[4]Author to whom any correspondence should be addressed. gtgullberg@lbl.gov.

SPECT is an imaging procedure in which an isotope tagged to a biochemical compound is injected into a patient's vein. As the isotope decays, it emits photons from the body, and these photons are detected and recorded by a camera that provides a digital image of the distribution of the radiotracer in the body. The SPECT system may consist of one, two (as shown in figure 1) or three detector head(s). The SPECT procedure records images of the distribution of the biochemical compound in the patient's body from different projections as the detector(s) rotate around the body. The detectors only need to acquire 180° of projection images but may acquire as many as 360° of projections. Newer SPECT systems being built today are constructed in the form of a fixed array of detectors partially or fully encompassing the patient's body.

Once the biochemical compound enters the blood stream, it travels to body organs (brain, liver, kidney, heart and the peripheral vascular system) and is absorbed by these organs according to each organ's affinity for the particular compound. Dynamic SPECT is an imaging procedure that follows the dynamic process of the biochemical compound once it enters the blood—transported by the blood, absorbed in organs and body tissues, and then either trapped within cells or on cell surfaces, or released back into the blood stream or the lymph system. Dynamic SPECT imaging, acquired using detector heads that rotate or remain fixed while radiopharmaceuticals exchange between biological compartments, records the actual movement (speed) of the isotopes through the body.

The premise of this review is that special data processing methods are required to extract dynamic information directly from projection measurements of injected radioactive biochemical compounds from dynamic SPECT data acquired using detector heads that rotate while radiopharmaceuticals exchange between biological compartments. These special data processing methods can also be applied to non-rotating SPECT and position emission tomography (PET) imaging systems.

The extraction of dynamic information and estimation of model parameters directly from projection measurements were first presented in a book chapter (Gullberg *et al* 1999). The chapter also reviewed work of the conventional approach to reconstructing a sequence of three-dimensional (3D) images, drawing regions of interest (ROIs), generating time–activity curves for these regions, and then estimating kinetic model parameters from these time–activity curves. Much of this work was built upon the developments in dynamic PET imaging. Several references to the PET literature can be found in this first book chapter, as well as in more recent reviews (Lodge *et al* 2005, Heller *et al* 2009). Later, a second book chapter (Gullberg *et al* 2004) reviewed the improvements in the conventional approach resulting from equipment advancements that enabled sufficient timing resolution to obtain wash-in and wash-out rate parameters of compartment models from time–activity curves generated from a sequence of reconstructed ROIs.

This review concentrates on the problem where all kinetic model parameters and time–activity curves are estimated directly from projection measurements and illustrates examples of this approach for imaging applications in dynamic cardiac SPECT. This approach is commonly referred to as 4D or 5D imaging in the literature and presentations at scientific meetings. The terminology of 5D imaging is given to methods of estimating time varying dynamics of the tracer through the organ while the organ, such as the heart, is also moving.

The introduction to this paper evolved out of work presented at an American Society of Nuclear Cardiology meeting (Gullberg *et al* 2000). The sections following the introduction give the mathematical developments used in dynamic cardiac SPECT, comparing conventional ROI methods, direct methods and semi-direct methods. For readers who do not want to go into the mathematics, the introduction gives a good overview of dynamic cardiac

SPECT. The paper assumes a basic understanding of nuclear medicine physics as found in Cherry *et al* (2003). Other works that give the basics of nuclear medicine physics, SPECT and clinical applications can be found in the chapters of the following two books: (Wagner *et al* 1995, Henkin *et al* 2006). Also, chapters 7 and 8 in Phelps *et al* (1986) give a very good introduction to kinetic modeling and the estimation of model parameters. A glossary is presented that defines several of the terms and acronyms for radiopharmaceuticals that may not be known to the general reader. A list of symbols is also presented to help the reader understand the definition of the different variables used in the equations.

1. Introduction

Dynamic single photon emission computed tomography (SPECT) is a technique that uses tracers to obtain images that reflect fundamental biophysiologic functions of perfusion and metabolism in body organs. This is done by quantifying the temporal changes of radionuclide concentration in tomographic sections through angular sampling of projections (Carson 1986b, Gullberg *et al* 1999). This technique, in conjunction with mathematical model-based analysis of regional kinetics of the radiotracer, allows for the quantitation of functional parameters, which are estimated by utilizing a time series of dynamic reconstructed images. Physiologic parameter estimation using kinetic analysis is well established in positron emission tomography (PET). However, the methodology has not seen routine clinical application in PET or SPECT. The development and use of kinetic analysis in dynamic SPECT applications have been limited by low sensitivity, poor spatial resolution and poor temporal resolution, which are consequences of the need to mechanically rotate the detector head for most studies. The use of ring detector systems for dynamic brain SPECT applications (figure 2), along with recent advancements in dynamic cardiac SPECT instrumentation (figure 3), has demonstrated SPECT's effectiveness for extraction of physiologic values of perfusion (Smith *et al* 1994, 1996) and metabolism (Gullberg *et al* 1999). This requires measurement of the blood input to the organ of interest and observation over time of the blood input and uptake as well as wash-out from the organ of interest. One then is able to fit physiological compartment models (see section 2.1) that represent the wash-in of the radiopharmaceutical, its metabolism or catabolism, and the wash-out of the tracer and its metabolites from the organ of interest. While this procedure has been used for years with PET to study several *in vivo* biochemical and physiologic processes in health and disease, it remains a challenge with SPECT, because most data are acquired using slow camera rotations. However, with recent developments in representation of data using a multi-resolution spatiotemporal basis (see section 3), special data processing methods can be used to extract kinetics from dynamic SPECT data acquired using detectors that rotate while radiopharmaceuticals exchange between biological compartments.

1.1. History

1.1.1. Early development of dynamic SPECT—Dynamic SPECT was used in brain studies as early as 1963 (Kuhl and Edwards 1963) using two discrete detectors and later using a fixed four-headed detector system, each with a linear array of eight discrete scintillation detectors (Kuhl *et al* 1976). This was followed in 1978 by another fixed four-headed detector system (DCAT) (Stokely *et al* 1980) capable of rapid acquisition (5 s sampling) of a few transaxial sections for imaging ^{133}Xe in the brain. In 1990, brain imaging was realized with a rotating four-headed gamma camera system (Kimura *et al* 1990). Also, dedicated brain systems consisting of a ring of scintillation detectors were developed (Rogers *et al* 1982, 1988, Hirose *et al* 1982, Moore and Mueller 1986, Genna and Smith 1988, Rowe *et al* 1993, Ogasawara *et al* 2000, Komatani *et al* 2004). These included the SPRINT system (Rogers *et al* 1982, 1988) developed at the University of Michigan; the Headtome II hybrid emission/CT system (Hirose *et al* 1982) developed by Shimadzu

Corporation, which incorporated scintillation detectors arranged in a circular ring with a set of collimator vanes that swung in front of discrete detectors; a unique Cleon Brain SPECT system originally developed by the Union Carbide Corporation in the 1970s, which consisted of 12 detectors that scanned both radially and tangentially (Stoddart and Stoddart 1979) with a reconstruction method (Moore and Mueller 1986) that was later marketed by Strichman Corporation; ASPECT, a dedicated brain system (Genna and Smith 1988), later manufactured by DSI, Inc. as the CERASPECT (Komatani *et al* 2004) (figure 2); and the FastSPECT system (Aarsvold *et al* 1988, Rowe *et al* 1993) developed at the University of Arizona, which was reported to be able to acquire dynamic tomographic data with a sampling interval of 2 s. A system with multiple rings of scintillation detectors was developed for brain SPECT studies in Japan by Shimadzu (Ogasawara *et al* 2000). The system consisted of 64 NaI crystals in a 38 cm diameter circle. Early on there were two ring systems proposed for cardiac SPECT imaging—the Shimadzu whole body system (Yonekura *et al* 1985) and the cardiac FastSPECT system (Rowe *et al* 1992)—but both systems remained conceptual designs.

In 1990, dynamic SPECT (Stewart *et al* 1990) was applied to the estimation of the wash-out of ^{99m}Tc-teboroxime from the myocardium in canine cardiac studies using a single-slice ring detector (SPRINT). However, it was not until 1991 (Budinger *et al* 1991) that it was demonstrated that a reliable blood input function could be obtained from 5 s sampling intervals of reconstructed dynamic SPECT data, and that this sampling regime would be sufficient for compartment model-based analysis of the data. Using the triple-headed camera configuration (figure 3(a)) first developed in 1985 (Lim *et al* 1985), the time–activity curves of a radionuclide were quantified in canine and human experiments. The dynamic data sets were reconstructed and corrected for attenuation using a reconstructed attenuation distribution obtained from a separate transmission scan. During the same period, commercial three-headed SPECT systems were used by two groups to image the wash-out of ^{99m}Tc-teboroxime from the heart by obtaining 360° tomographic acquisitions every 1 min (Nakajima *et al* 1991, Chua *et al* 1993).

The first results of a compartment model-based analysis of dynamic cardiac SPECT data were obtained using the three-headed PRISM system (figure 3(a)) (Picker, Cleveland, OH) (Smith *et al* 1994, 1996). Using attenuation-corrected dynamic reconstructed data from canines, it was demonstrated that the estimated wash-in and wash-out of ^{99m}Tc-teboroxime correlated with microsphere-derived flow estimates. A similar approach was demonstrated in humans (Chiao *et al* 1994a). Although the work did not correct for attenuation, it was shown that the wash-in and wash-out estimates of ^{99m}Tc-teboroxime for the whole left ventricular myocardium changed significantly in response to coronary vasodilatation.

The original three-headed PRISM SPECT system (figure 3(a)) had the mechanical stability and control hardware to allow acquisition of 360° of data in 5 to 10 s. The major advantage of a system of multiple-gamma camera heads is the improvement in sensitivity afforded by better coverage of the solid angle. However, the arrangement of the detector heads is important for minimizing attenuation of posterior views for cardiac imaging. Another advantage is that multiple heads reduce the angular range of motion necessary to acquire a complete data set. Thus, only 120° of rotation is needed for a three-headed system and 90° is needed for a four-headed system. The disadvantages are that a system of multiple large field-of-view gamma cameras is expensive, and fast rotations (complete tomographic acquisitions of 10 s or less) are not available on all systems.

1.1.2. Dynamic SPECT applications—The main focus of this review is the application of dynamic SPECT to cardiac studies. However, dynamic SPECT has found significant application in pulmonary (Coates 1992, Ercan *et al* 1993, Sakaji *et al* 2001), renal (Hansen

et al 1994, Akahira *et al* 1999) and brain studies. Dynamic SPECT imaging has been used to estimate lung regional function using ^{133}Xe (Sakaji *et al* 2001). It has been used to evaluate renal plasma flow of transplanted kidneys using ^{99m}Tc-MAG3 (Akahira *et al* 1999). A simulation study also showed that dynamic SPECT could be useful for evaluating kidney function using a three-headed SPECT system to image ^{123}I-hippuran (Vanzi *et al* 2004). A major portion of the application of dynamic SPECT in the study of *in vivo* physiological function has been directed toward the study of brain disorders.

A body of recent work is directed toward the dedicated ring detector systems for brain imaging and systems with detector arrays partially encompassing the body are currently being introduced into the clinic for cardiac imaging. A ring-type dedicated brain SPECT called the Headtome was successfully used with ^{99m}Tc-HMPAO to quantitatively image brain blood flow in patients with a stroke (Toyama *et al* 1996). Another ring system, the CERASPECT (DSI, Inc. Waltham, MA) (figure 2), was used to study the retention process of ^{99m}Tc-ECD in normal and ischemic lesions, and early phase images of the tracer were found to be as useful as ^{133}Xe-rCBF SPECT for detecting mild or moderate ischemic lesions (Komatani *et al* 2004). A study using ^{123}I-iodoamphetamine (^{123}I-IMP) in patients with meningiomas, which compared lesion-to-normal ratios with angiographic vascularities and histological types, concluded that dynamic SPECT with ^{123}I-IMP was more effective than angiography for evaluating the vascularity of lesions (Nakano *et al* 1988). Studies using ring SPECT cameras have been employed to image subacute cerebral infarction (Ogasawara *et al* 2001a), herpes simplex encephalitis (Ogasawara *et al* 2002b), reperfusion hyperemia after acute cerebral embolism (Ogasawara *et al* 2002a) and Lhermitte-Duclos disease (Ogasawara *et al* 2001b).

For several years, dynamic SPECT has been used to evaluate the central benzodiazepine (BZP) receptor binding of ^{123}I-iomazenil (^{123}I-IMZ, a benzodiazepine antagonist) in the diagnosis of central nervous system disorders with abnormalities in BZP receptor binding (Ito *et al* 1997). These studies with dynamic SPECT and ^{123}I-IMZ have shown defects in the benzodiazepine receptors in brain pathologic diseases such as ischemia, epilepsy, Alzheimer's disease, Huntington's disease and schizophrenia (Moriwaki *et al* 1998), and for prognosis prior to endoreterectony (Tsuchida *et al* 1999). Recently it was reported that dynamic SPECT was used with ^{123}I-IMZ to study a rare case of slowly progressive neuronal death associated with postischemic hyperperfusion in cortical laminar necrosis (Iihara *et al* 2009). The condition was experienced after cerebral artery bypass surgery for an intracavernous carotid artery aneurysm. Studies have also shown that dynamic SPECT gives comparable results to those of dynamic PET using ^{11}C-IMZ (Bremner *et al* 1999). Kinetic model-based methods have been developed for SPECT to quantitatively measure ^{123}I-iomazenil binding to benzodiazepine receptors in the human brain (Dargham *et al* 1994). The significance of receptor-binding kinetics has generated interest in using a standard input function instead of having to perform arterial sampling to obtain the input function (Seike *et al* 2004).

It is interesting to note that in Japan, more so than in the USA, noninvasive tests are used for diagnosing brain autoregulatory abnormalities (Rudzinski *et al* 2007). Dynamic SPECT scans are used to quantify cerebral blood flow (CBF) and cerebral vascular reactivity (CVR) in a single session using a split dose administration of ^{123}I-iodoamphetamine (^{123}I-IMP)—one at rest and one during Diamox challenge (Imaizumi *et al* 2002). The rest/stress protocol is much like that performed to evaluate myocardial perfusion. First, a rest dynamic cerebral blood flow study is performed after the injection of ^{123}I-IMP. After the completion of the first study, Diamox is administered to stress the cerebral vascular system. A second study is then performed after administration of a second injection of ^{123}I-IMP. A large-scale clinical trial showed that appropriately quantifying dynamic SPECT data by correcting for

attenuation, scatter and collimator response gave values for CBF at rest and during Diamox treatment that were reproducible among institutions, and it demonstrated that the modality was useful for diagnosing brain autoregulatory abnormalities and for providing CBF and perfusion reserve from a single scanning session (Iida *et al* 2006).

1.1.3. Dynamic cardiac SPECT advances—Early work in dynamic cardiac SPECT concentrated on using systems with rotating multiple-gamma camera heads to image tracers with fast kinetics (Chua *et al* 1993, Smith *et al* 1994, 1996). However, the focus has changed, since tracers with slower wash-out kinetics, such as ^{201}Tl (Iida and Eberl 1998, Gullberg *et al* 1999) and ^{99m}Tc-sestamibi (Gullberg *et al* 2007a, Reutter *et al* 2007a), are more readily available for perfusion studies, and cardiac metabolic agents, such as ^{123}IPPA (Limber *et al* 1995, Gullberg *et al* 1999) and ^{123}I-BMIPP (Gullberg *et al* 2006), are more appealing for myocardial viability studies or for evaluating myocardial fatty acid metabolism in patients with hypertrophic cardiomyopathy (Okizakia *et al* 2007). In addition, improvements in data processing techniques have allowed processing of kinetics using only a single rotating detector that is commonly used in clinical nuclear medicine. The use of ^{99m}Tc-teboroxime (Chua *et al* 1993, Smith *et al* 1994, 1996), a rapidly exchanging agent, shows promise in the application of dynamic SPECT for imaging the heart. Also, recent results suggest that implementing a dynamic SPECT protocol can shorten clinical ^{123}I-MIBG imaging studies that are used to assess the severity of heart disease and prognosis in patients with chronic heart failure (CHF) (Takeishi *et al* 2005, Hu *et al* 2005).

Although the standard single-gamma camera configuration for SPECT is still commonly encountered in clinic inventories, it has been supplanted at many institutions by dual- or triple-headed detector systems, with dual-headed detector systems being most prevalent. Today, the dual-headed detector SPECT system (figure 1) is the most common imaging system used in nuclear cardiology because it can perform cardiac scans (the most commonly performed procedure) as well as whole body bone scans. The detectors on these dual-headed detector systems are much larger than the original three-headed detector PRISM system (figure 3(a)), but the rotational speed of the modern systems with the most robust gantries is still limited to a single tomographic acquisition every 15 s. As a result, data processing techniques have emphasized the development of methods for processing kinetics directly from projection measurements.

1.1.4. New dedicated cardiac SPECT systems—Digirad was the first company to develop and manufacture a dedicated cardiac SPECT scanner (Patton *et al* 2007). New versions of the system have small multiple-gamma cameras that rotate to obtain sufficient angular sampling along with an x-ray transmission system for obtaining an attenuation map for attenuation correction. The new dedicated cardiac system developed by Spectrum Dynamics (Caesarea, Israel) (Sharir *et al* 2007, 2008, 2010, Berman 2007, Gambhir *et al* 2009, Erlandsson *et al* 2009, Ben-Haim *et al* 2010, Patton *et al* 2007) (figure 4) is able to obtain high quality cardiac perfusion images of 2 min stress and 4 min rest acquisition times. Another newly developed dedicated cardiac scanner is the CardiARC (Lubbock, TX) (Berman 2007, Patton *et al* 2007), which is similar in concept to the original SPRINT design with a fixed ring of detectors and a rotating slit collimator. GE Healthcare (Haifa, Israel) has announced the development of a new dedicated cardiac SPECT system (figure 3(b)) (Volokh *et al* 2008, Garcia *et al* 2008, Esteves *et al* 2008, Buechel *et al* 2010). Another dedicated cardiac SPECT system called C-SPECT, being built at Rush University Medical Center, Chicago, IL, is being funded by the NIH (Chang *et al* 2008, Ordonez *et al* 2008). Ultimately, dedicated cardiac SPECT systems with total acquisition times of 2–3 min may become available. While these more recent non-rotating detector systems are ideal for dynamic cardiac SPECT, rotating three- and two-headed detector systems have been shown to provide adequate temporal resolution (Gullberg *et al* 2004).

1.2. Radiopharmaceutical considerations for dynamic cardiac and brain SPECT

This discussion of applications is not a comprehensive review of nuclear medicine imaging approaches to the brain and heart using radiopharmaceutical agents, but is intended to highlight the application of dynamic SPECT along with some comments relative to competitive approaches with PET. A 'chemical microsphere' is a term given to a radiotracer that becomes trapped within a cell. Microspheres are small spherical particles with diameters in the micrometer range, typically 15 μm for heart studies so these become trapped in small capillaries. They are used to measure absolute organ blood flow. The microsphere method is based on the principle of conservation of material (Fick principle); that is, the amount accumulating in tissue is equal to flow times concentration of the material available in the blood minus flow times concentration of the venous wash-out. In the microsphere method, there is a no wash-out of the accumulated material. If a single photon tracer is trapped in the tissue, its behavior will approximate the properties of a 'chemical microsphere'. It has been suggested that ^{99m}Tc-sestamibi (^{99m}Tc-MIBI) may be useful as a tracer for calculating coronary flow reserve (CFR) using this 'microsphere' technique (Sugihara *et al* 2001). This agent accumulates in the myocardium in proportion to flow but, unlike microspheres, washes out slowly; thus quantitation of flow requires dynamic data acquisition and an appropriate model, unless the wash-out is slow enough that the integral of uptake activity over a short time period can be used in a 'microsphere' technique. The agent ^{99m}Tc-tetrofosmin has also shown promising initial results for calculating CFR using a single-headed detector SPECT system (Sugihara *et al* 2001). ^{123}Iodorotenone (Marshall *et al* 2001) is another potential agent that has an even higher extraction fraction than the commonly used compounds of ^{99m}Tc-MIBI or ^{99m}Tc-tetrofosmin and may also be a useful tracer for calculating CFR using the microsphere analogy. Further work is required to evaluate the 'microsphere' method for calculating CFR and to compare this approach with that of using either dynamic SPECT or dynamic PET imaging of agents that have fast turnover (i.e., rapid exchange, such as $H_2{}^{15}O$).

Dynamic cardiac SPECT imaging could potentially be useful for measuring CFR, but it requires a flow agent with a large range of flow values for which the extraction fraction (arterial concentration minus the venous concentration divided by the arterial concentration) remains linear as a function of flow. It was shown (Chiao *et al* 1994a) that wash-in and wash-out estimates of ^{99m}Tc-teboroxime for the entire left ventricular myocardium change significantly in response to coronary vasodilatation. Quantitative compartmental analysis of ^{99m}Tc-teboroxime kinetics provides a sensitive indicator for changes in estimates of wash-in in response to adenosine-induced coronary vasodilatation (Gullberg *et al* 1999, 2004). It has also been shown that dynamic imaging of ^{99m}Tc-teboroxime with compartment modeling provides a better measure of flow with parametric images of better contrast between normal and decreased flow regions than can be obtained from static imaging of ^{201}Tl or, for that matter, static imaging of ^{99m}Tc-teboroxime (Gullberg *et al* 2004). In fact, dynamic SPECT may prove advantageous over static imaging because it may enable better measurement of both perfusion and viability (Gullberg *et al* 2004).

In addition, dynamic SPECT methods may be useful for evaluating myocardial function using other tracers such as the perfusion agent ^{99m}Tc-N-NOET (Calnon *et al* 1999) and metabolic agents such as the fatty acid ^{123}IPPA (Gullberg *et al* 1999). The agent ^{99m}Tc-N-NOET has features of greater redistribution (the apparent filling in of a myocardial perfusion defect over a period of time due to differential wash-in and wash-out of a tracer between ischemic and normal regions). This agent has good linearity with flow but has not yet been introduced into the clinic (Johnson*et al* 1996). ^{99m}Tc-N-NOET, like ^{99m}Tc-teboroxime, is a neutral compound but unlike ^{99m}Tc-teboroxime exhibits slower myocardial clearance. This agent is thus a potentially better alternative for dynamic cardiac SPECT imaging than

either ^{201}Tl or ^{99m}Tc-teboroxime. In PET, ^{82}Rb, $^{13}NH_3$ and $H_2{}^{15}O$ are the tracers most often used for measuring CFR.

There are also several radiopharmaceuticals used for brain SPECT that may be applicable for dynamic SPECT. For brain tumor imaging the primary modality involves using PET to image ^{18}FDG (Chen and Silverman 2008). ^{18}FDG-PET is also used to diagnose epilepsy. However, SPECT imaging with ^{99m}Tc-HMPAO or ^{99m}Tc-ECD is also able to identify the ictal (a physiologic state or event such as a seizure) onset zone in the majority of cases (Goffin *et al* 2008). Interictal (the period of time between seizures as a result of an epilepsy disorder) SPECT imaging is unreliable for determining the seizure onset zone, but interictal ^{18}FDG-PET is routinely used to detect brain areas of hypometabolism. For diagnosing major depression disorders, PET is again an important imaging modality, but ^{123}I-beta-CIT and ^{123}I-ADAM are also used with SPECT to diagnose depression (Meyer 2008). For central motor disorders, both PET and SPECT imaging agents play roles in clinical diagnosis of Parkinson's disease and other movement disorders (Kung *et al* 2003, Seibyl 2008). ^{18}F-DOPA-PET is important in the diagnosis of motor disorders. However, ^{123}I-FP-CIT, ^{123}I-beta-CIT, ^{99m}Tc-TRODAT and ^{123}I-altropane are also used. These tracers measure different aspects of dopaminergic function and may contribute different and potentially complementary information about the disease process. The focus has been on patients in the early stages of illness. However, these agents might serve as biomarkers of the progression of disease. SPECT has also been used to diagnose dementia (Pimlott *et al* 2007, Jagust *et al* 2009, Resnick *et al* 2010). Specifically, it has been used in the diagnosis of Alzheimer's disease (Wolfe *et al* 1995, Jagust *et al* 1998, 2001). Addiction is an area where there are no SPECT ligand tracers that compete with PET approaches (Volkow *et al* 2003, 2009) as in the case for dementia studies.

1.3. Data processing techniques

Compartmental modeling of tracer kinetics is utilized to extract kinetic parameters from dynamically measured data of compartment models that describe the pathways and dynamic behavior of tracers in organ tissues (see section 2). Significant work has been accomplished to improve the conventional method of analysis of dynamic cardiac SPECT data in which ROIs are specified in a sequence of reconstructed images and time–activity curves are generated from the data values in these ROIs (Gullberg *et al* 2004). These time–activity curves are input to a nonlinear estimation program (Huesman *et al* 1995) that estimates the compartment model kinetic parameters. The ROIs are usually drawn by hand, but semi-automatic programs (Di Bella *et al* 1997) can improve reproducibility from study to study. Kinetic parameters can also be calculated for every image voxel by fitting a time–activity curve generated from a dynamic reconstructed sequence to a compartment model. The parameter values are then mapped to colors or gray levels and displayed as parametric images (Sitek *et al* 2002a, Gullberg *et al* 2004).

This review highlights advancements in the estimation of kinetic parameters from projections as opposed to the conventional method of estimating kinetic parameters from dynamic reconstructed images. This approach can be readily applied to all camera systems, including those with low geometric efficiency and slow camera rotation. The possibility of performing dynamic cardiac SPECT imaging using a single slowly rotating camera head is enticing, since such scanners are both inexpensive and widely deployed. Unfortunately, the angular projections obtained are inconsistent when a rotating camera head is employed to image a distribution of emission sources whose activity varies significantly during the time necessary for the camera head(s) to complete a revolution. Consequently, application of conventional tomographic reconstruction algorithms yields inaccurate reconstructed images that are 'blurred'. This leads to biases in the estimated kinetic parameters. The inconsistent projection problem may be viewed as one of attempting to interpolate in time and space

simultaneously—in sinotimogram space (sinogram of a time-varying distribution corresponding to projection data represented by three coordinates—the angle, the projection bin and the time). Such interpolation is only feasible if *a priori* knowledge regarding the geometry and time–activity evolution of the image sources is included.

A better approach to analyzing dynamic data (SPECT or PET) than using time–activity curves generated from reconstructed regions is to estimate the time–activity curves or kinetic parameters directly from the projection data of the sinotimogram, using an accurate model of the data acquisition of the spatial and temporal distribution of the radiopharmaceutical within the field-of-view. The simultaneous estimation of blood input function and kinetic model parameters can reduce bias and improve precision by using the interrelationship between blood and tissue imposed by the compartment model to constrain the solution.

1.3.1. Estimating dynamic parameters directly from projection measurements

—The modeling of dynamic data is complicated by the combination of camera gantry motion, potential organ motion and the time-varying nature of the radionuclide distribution being imaged, resulting in inconsistent projection data sets wherein the projection from one angle is not consistent with that from another angle because the radionuclide concentration in the field of view changes between the time of acquisition for the different projections. Entire tomographic slices or volumes must be represented by some types of parameterization, and one does not have the option of analyzing a single ROI and ignoring the remainder. The estimation can be formulated as a minimization of a weighted sum of squared differences between the projection data and the model-predicted values. It was shown that biases in estimates from time–activity curves generated by dynamic reconstructions are eliminated by estimating dynamic parameters directly from the projections (Limber *et al* 1995, Gullberg *et al* 1999). Results also suggest that direct joint estimation of compartmental or other dynamic model parameters and blood input function from projections produce estimates of kinetic parameters with lower variance and bias than does the estimation of kinetic parameters from time–activity curves generated from dynamic reconstructed ROIs (Reutter *et al* 2005) (see section 5.1).

There are two main approaches for estimating dynamic parameters directly from projection measurements. One approach (semi-direct—a two step process) is to directly calculate activities for ROIs as a function of time; the results provide time–activity curves from which kinetic compartmental model parameters can be estimated (Carson 1986a, Formiconi 1993). A second approach (direct—a one step process) is to estimate dynamic parameters directly from the projection data, where it is assumed that the ROIs are specified and that expressions between the compartment model parameters and the dynamically acquired projections can be formulated in a chi-square formulation (Limber *et al* 1995, Zeng *et al* 1995). There are many variations or refinements that can be used with both methods. One refinement of both methods is the segmentation of organ boundaries or tissue types involving the joint estimation of spatial boundaries and temporal parameters. It was shown that biases of estimates are reduced by simultaneously estimating kinetic model parameters and boundary parameters of ROIs directly from projections and auxiliary boundary information (Chiao *et al* 1994b, 1994c). These boundaries may be static or dynamic. A method was proposed to estimate kinetic model parameters and boundary parameters for the heart from dynamic gated cardiac SPECT data (Gullberg *et al* 2007b). This is commonly referred to as 5D tomography.

Semi-direct approach (mathematical examples are presented in section 5): The estimation of ROI time–activity curves from projections without reconstructing the ROI was first implemented in PET and was fairly easily accomplished using a convolution

backprojection algorithm. First, a method to estimate the average activity in a 2D ROI was described (Huesman 1984). Subsequently, these ideas were extended to 3D ROIs (Defrise *et al* 1990). To compensate for physical factors such as attenuation and detector resolution, iterative algorithms that maximize a likelihood function had to be used (Carson 1986a, Formiconi 1993). An extension of this is to estimate the time–activity curves directly as continuous functions from projections, and then to estimate kinetic model parameters using the estimated time–activity curves (Reutter *et al* 2000, 2002, 2004a) (see section 5.1).

Some of the first work in SPECT to reconstruct time–activity curves from dynamically acquired projection data was accomplished by the group at the University of British Columbia (Bauschke *et al* 1999, Farncombe *et al* 1999, 2000, 2001, Farncombe 2000, Celler *et al* 2001). That work led to the development of the 'dSPECT method', which fits time–activity curves for each voxel directly from projection measurements acquired from single or multiple rotations of the gantry (see section 5.3). Initially, a version of the algorithm reconstructed time–activity curves that were constrained to monotonically rise or monotonically fall (Celler *et al* 2001). A modification led to the ability to reconstruct time–activity curves that rose to an estimated maximum value and then fell, much as would be expected, by the wash-in and wash-out of a tracer from an organ of interest (Farncombe *et al* 2001). The method required either prior knowledge or estimating the time frame when the activity peaked in each particular voxel of the object being imaged (Farncombe *et al* 2001). The main focus of dSPECT was to derive estimates of time–activity curves for studies performed using only a single rotation of a standard SPECT camera. The method has been utilized in clinical applications, including applications for reduction of bladder artifacts in pelvic bone SPECT (Wells *et al* 2004) and for estimating time–activity curves from gated cardiac SPECT data (Farncombe *et al* 2003a, 2003b, Feng *et al* 2006).

Another approach for extracting time–activity curves from dynamic data has been the method of factor analysis of dynamic structures (FADS) (see sections 3.3, 5.2). This method has been applied primarily in nuclear medicine to dynamically acquired planar data and to the dynamic sequence of reconstructions of projection data acquired with fast SPECT acquisition (Sitek *et al* 1999a, 1999b, 2000, 2002a, 2002b, Su *et al* 2007). However, it also has potential application for extraction of time–activity curves directly from dynamically acquired projections from slow rotation SPECT camera systems. For example, FADS was applied to extract time–activity curves from projections of the uptake and wash-out of ^{99m}Tc-MAG3 from the kidneys (Sitek *et al* 2001). Factor analysis was also used for extracting the blood input function in rats from dynamic SPECT data acquired with slow camera rotation (Hu *et al* 2008).

The group at LBNL has put effort into developing computationally efficient methods for estimating the time–activity curves from dynamic SPECT projection data. A direct least-squares estimation of spatiotemporal distributions from dynamically acquired SPECT projection data was developed (Reutter *et al* 2000, 2002, 2004a). Temporal B-splines (see section 3.1) providing various orders of temporal continuity, as well as various time samplings, were used to model the time–activity curves for blood pool and tissue volumes. An alternative time–activity curve model, based on a small set of orthogonal exponential basis functions and couched in a similar least-squares estimation framework, was also proposed (Maltz and Budinger 2000, Maltz 2000a).

There are several possibilities that could be used for the temporal basis functions in the spatiotemporal representation of reconstructed dynamic data. These could be exponential, spline or factor (discrete temporal function describing a time course of activity concentration for a particular organ or tissue) basis functions. Multi-resolution B-splines and penalized least-squares inversion (see section 5.1) have been used to reconstruct dynamic cardiac

SPECT data from rest/stress cardiac patient studies acquired using a clinical SPECT system with slow camera rotation (Gullberg *et al* 2007a, Reutter *et al* 2007a). By extending the support of spatial B-splines into the time dimension, estimates of time–activity curves were obtained directly from projections. The use of non-uniform time sampling with piecewise-quadratic splines yielded smooth time–activity curves that captured the relatively fast rise and fall of the tracer in the right (15 s after injection) and left ventricular blood chambers (45 s), as well as uptake and retention of the tracer in the left ventricular myocardium.

The solution to a system of differential equations which express the time varying distribution between compartments involves expressions of exponentials. Therefore, it is very natural to parameterize the kinetics of the radiopharmaceutical distribution in the tissue as a spectrum of exponential terms in time. The spectral-based approach builds on earlier work (Cunningham and Jones 1993) in which it was suggested that, instead of estimating the kinetic parameters of models, one could estimate the coefficients of a predefined spectrum of exponentially decaying factors. It is assumed that the decay constants for the exponentials span some reasonable ranges of physiological values, and those are predefined with sufficient sampling to adequately represent the kinetics of the tracer.

Efforts have been made to calculate these coefficients directly from projections for a few spectral terms, such as for two spectral terms (Hicks *et al* 1989, Hebber *et al* 1997) or for several spectral terms (Matthews *et al* 1997, Maltz 2001, 2002). This approach obviates the need for iterative estimation of the nonlinear parameters (rate constants) of a compartment model, allowing a convenient solution via linear methods (Maltz 2001).

A significant limitation of exponential spectral methods is that the solution obtained may not be unique due to the large amount of parameter redundancy, which is characteristic of sums of decaying exponential terms. Spectral coefficient estimates must therefore be interpreted with caution. Application of dimension-reducing transforms, such as the singular value decomposition (SVD), can decrease the dimension of the spectral estimation problem to approximately 1/20th of its original size while ameliorating the problem of parameter redundancy (Maltz and Budinger 2000).

Unfortunately, because sums of decaying real exponentials are not uniquely parameterized in the presence of noise, solutions in terms of spectral coefficients may not be unique (Lanczos 1956, Reich 1981). A strong dependence may consequently exist between the particular solution obtained and the noise present within the data. The parsimonious exponential spectral analysis (ESA) algorithm ameliorates the inherent problem of non-uniqueness in ESA parameters (Maltz 2002). It has been shown (Maltz 2001) that using an exponential basis with a nonuniform resolution reconstruction grid leads to a tremendous reduction in the dimension of the problem of direct dynamic emission computed tomography reconstruction from inconsistent projections. The solution coefficients, which must be non-negative, can be determined by using either a non-negative least-squares technique (Meikle *et al* 1996, 1998) or the ML-EM algorithm (Matthews *et al* 1997). Computationally, it can be performed in succession by first determining spectral components for each projection sample (Meikle *et al* 1996, 1998). The spectral components for each pixel can then be reconstructed from the spectral components of the projection ray sums. Instead of using an exponential decomposition, one can use some other parametric decomposition (Matthews *et al* 1997), some other best fit model (Hudson and Walsh 1997, Hutton *et al* 1997) or some physical factors (FADS method) (Barber 1980, Sitek *et al* 2002b).

Direct approach (mathematical examples are presented in section 4): A direct approach involves eliminating the step of estimating time–activity curves by estimating the model

parameters directly from the measured projections. This approach must apply the correct model to every voxel or region, which requires modeling the entire object. One voxel or ROI might be an input function, while another voxel or tissue region might be a one-compartment perfusion model, a two-compartment metabolic model or a multi-compartment ligand binding model. An important issue is the segmentation of organs or tissue types, especially the segmentation of the blood ROI, since a direct approach requires the simultaneous estimation of both the input function and the kinetic model parameters (Reutter *et al* 2005) (see section 4.1). If the tissue or organ moves, such as in the case of cardiac motion, this also needs to be modeled correctly. It is also necessary to model accurately the physics of the imaging detection process, such as scatter, attenuation and collimator response. One can see that this becomes a very large complex nonlinear optimization problem.

A direct approach to estimating dynamic parameters can reduce the bias and variance, but it assumes that the modeling is appropriate for the dynamic process being realized. If the locations of the tissue regions are known, it has been demonstrated that bias is reduced by estimating kinetic parameters of a compartment model directly from projections. This was demonstrated for a 3 × 3 computer-simulated image array (Zeng *et al* 1995), for a 64 × 64 computer simulation using parallel geometry (Gullberg *et al* 1999) and for a 48 × 48 × 30 computer simulation using cone-beam geometry (Huesman *et al* 1998). These studies assumed a one-compartment model with a blood input function (see section 2.2).

The most direct approach is to derive the kinetic model parameters directly from the projection data for each pixel (Kadrmas and Gullberg 2001) (see section 4.3). This could be one or multi compartments. Multiple compartments could be represented by a spectral decomposition (see section 4.4). However, the low signal-to-noise ratio of dynamic SPECT, and the poor condition number of the inverse problem, severely limit the number of regions that may be resolved. To reduce the dimensionality of the problem so that it is not necessary to specify a compartment model for each voxel, methods of presegmentation of particular tissue regions based on anatomical and physiological considerations have been proposed (see section 4.1). For myocardial studies, typical regions might include healthy blood pool, myocardium, myocardial defect, liver and background (Huesman *et al* 1998, Reutter *et al* 1998a, 2000) (see section 4.2). The accuracy of the kinetic models depends on an accurate initial segmentation, which might not be easily accomplished. For example, in a clinical study the location of a defect is not known *a priori*. The most obvious way of ameliorating this problem is to segment the myocardium into several regions such that the smallest physiologically significant defect might be detected. Another approach would be to spatially parameterize the entire myocardium or a small number of regions of the myocardium. However, as the number of regions is increased, the statistical advantages of anatomically or physiologically motivated presegmentation are lost.

Joint estimation of spatial boundaries and dynamic parameters: A refinement in the estimation of dynamic parameters from projections involves simultaneously estimating the geometric regions and the time–activity of the regions directly from the inconsistent projection data. Progress toward the development of practical joint spatial and temporal algorithms has been limited because of the severely ill-conditioned nature of this nonlinear problem. The first joint spatial and temporal algorithm for dynamic emission computed tomography (Chiao *et al* 1994b, 1994c) enabled the fitting of a single dynamic region (the myocardium) to simulated myocardial data in the presence of noise and background activity. The myocardial activity was described using a first-order single-compartment model, and the geometry of the myocardium was described by a parameterized concentric polygonal model. A local optimization strategy was able to recover the joint parameter set, which consisted of the endocardial and epicardial radii at the vertices of the respective polygons,

and compartment model parameters. It was demonstrated that biases in the kinetic parameter estimates were reduced by allowing for estimates of the boundary of the ROI to be included in the estimation process.

Extension of joint spatial and temporal algorithms to multiple regions proves non-trivial because the parameter estimation problem becomes multimodal. Its solution consequently requires a computationally intensive, multi-start optimization algorithm. Such an algorithm was developed at the University of California, Berkeley, and is able to fit more than ten dynamic regions to data acquired with the slow rotation of a single-gamma camera operating at realistic photon count rates (Maltz *et al* 1998). A set of spatially constrained ellipses is used to model regions within the image where the activity of each region is described using a single-compartment model. It appears that it is the poor condition of the inverse problem rather than a low number of photon counts per resolution element that limits the accuracy of the recovered regional time–activity curves (Maltz 2000b). The ill-conditioning is due, in part, to the well-known problem of parameter redundancy in sums of real exponential functions (Lanczos 1956, Reich 1981). When several sources within the image follow first-order single-compartment tracer kinetic models, the projection measurements are composed of weighted sums of decaying exponential functions convolved with a blood input function. When joint estimation is performed, it is the parameters of these exponentials, along with the geometric model parameters, that are sought. Since vastly different parameterizations of these sums may yield resultant functions that are indistinguishable at realistic noise levels, there can be no certainty that a unique solution exists. This condition may be improved by replacing the exponential functions with orthogonal basis functions that, when convolved with the blood input function, are able to represent all physiologically feasible time–activity curves using a less redundant parameterization (Reich 1981, Maltz *et al* 1998). The quality of the reconstruction that may be obtained using joint spatial and temporal algorithms applied to single slow rotation data is dependent on the quality of the constrained geometric and kinetic models used to restrict the set of solutions to those that are physiologically feasible.

5D processing of dynamic gated cardiac SPECT data: The estimation of dynamic parameters from projections that model the deformation of the organ as a function of time and the change in the concentration of the tracer as a function of time is referred to as 5D tomography. For the heart, it is assumed that the data are acquired dynamically with cardiac phase information either by list mode acquisition or by binning into gated dynamic frames over the cardiac cycle. The groups at the University of Massachusetts and the University of British Columbia extended the dSPECT method to obtain reconstructions of the time variation of the concentration of the tracer in the heart from dynamically acquired gated cardiac SPECT data (Farncombe *et al* 2003a, 2003b, Feng *et al* 2003a, 2006).

The group at the Massachusetts Institute of Technology (Feng *et al* 2003b, Shi and Karl 2003, 2004, Jin *et al* 2005, 2006a, 2006b) took a different approach from that used in the dSPECT method by using the level set method (a numerical technique for tracking interfaces and shapes) to delineate boundaries of moving organs, such as the heart, while simultaneously estimating the time variation of the tracer concentration in the organ. 5D tomography has all of the challenges of modeling both rigid and non-rigid body deformation simultaneously with the modeling of a time varying tracer concentration from tomographic projections (Gravier *et al* 2007, Gullberg *et al* 2007b). In the future, this will have important applications in diagnostic medicine and in radiotherapy with injected radioisotopes.

1.3.2. Input function—One of the most difficult problems in applying kinetic modeling is estimation of the blood input function (see section 2.3 for a more extensive discussion). The sampling of the blood input at a high temporal resolution is more important than sampling

the tissue response with a high temporal resolution. Estimation of the input function from the imaging data is problematic due to partial volume effects, scatter and cardiac and lung motion that tends to contaminate the blood data with data from the myocardium, liver and other surrounding tissues. The input function is especially difficult to measure in pinhole SPECT imaging of small animals using a rotating large field-of-view gamma camera (Hu *et al* 2005). The blood volume is small, and thus it can be difficult to obtain the blood input function (Laforest *et al* 2005). Furthermore, limited system resolution can make ROI sampling of the ventricular cavity problematic. In addition, the recirculation time is of the order of seconds (6–8 s in a rat). Therefore, it is difficult to capture the true time–activity curve because the full tomographic acquisition requires 90 s. For this application, it has been shown that factors can be estimated directly from projections but it requires the estimation of greater than a million unknowns (Hu *et al* 2005). An intriguing approach is to estimate the kinetic model parameters for the myocardium from projections without *a priori* knowledge of the input function—blind estimation (Di Bella *et al* 1999). However, this method limits which kinetic parameters can be estimated absolutely.

1.3.3. Multigridding approaches—An advantage of spatiotemporal modeling is the ability to reduce the number of unknown parameters by using multi-resolution or multigridding approaches to represent spatial and temporal distributions of dynamic data. Three possible spatial basis functions involve the use of (1) uniform voxels, (2) splines or (3) point cloud distributions of tetrahedral finite elements. These spatial basis functions can be combined with temporal basis functions using, for example, exponential, spline or factor basis functions or time–activity functions that fit a particular compartment model.

Multigridding approaches using splines: The spatial parameterization can involve a multi-resolution or multigridding approach where inside the organ boundaries the changing tracer kinetics are modeled with high resolution and outside the organ the distribution is modeled with a more coarse resolution (Boutchko *et al* 2006b, Reutter *et al* 2006, Sitek *et al* 2006). B-spline spatial basis functions can be used to model continuous 3D tracer distributions in the heart (Reutter *et al* 2006, 2007b), and this approach improves signal-to-noise and increases computational efficiency compared to methods based on small cube-shaped voxels. Uniform B-spline basis functions have the property that splines of larger support can be composed from a linear combination of splines of smaller support, thus facilitating creation of a multi-resolution spatial model. B-splines can be evaluated quickly when calculating projection data models or displaying reconstructed images, and there is no image ‘blockiness’ because B-splines yield a spatially continuous representation. A negativity penalty can be incorporated into the estimation of the spline coefficients so that these coefficients that tend to have negative values are constrained to stay near zero, with use of a quadratic penalty that penalizes nonzero contributions to the projection data model (Reutter *et al* 2007b). Use of the penalty reduces image noise when employing more compact splines to maintain good resolution throughout the body.

Multigridding approaches using point clouds: Another multigridding image representation is the use of point clouds where the points are distributed on an irregular grid that adapts to the information content in the projection data (Sitek *et al* 2006). The points serve as vertices of a tetrahedral mesh formed using the Delaunay tessellation algorithm (de Berg *et al* 2008) or some other finite element representation. Inside each tetrahedron, a continuous function is represented by the linear interpolation of the vertex values. An original reconstruction is performed (using the ML-EM algorithm) on a coarse Cartesian grid with the grid points distributed randomly with their density proportional to the second directional derivative of the Cartesian image. The number of points is increased by the user in the regions where high resolution is required. The point cloud is then allowed to deform

and increase in density to achieve optimal correspondence with the Cartesian image. The image is reconstructed on the new irregular grid directly from projections. Small deformations of the grid are also allowed during the reconstruction. A reduction in the number of grid points by a factor of 100 was achieved when the heart was reconstructed with high spatial resolution (Boutchko *et al* 2006a), and other volumes with lower resolution. In the reconstruction of low signal-to-noise ratio dynamic data, the application of the point cloud grid significantly reduced the number of grid points and improved visual perception of single frame images (Boutchko *et al* 2007). The process can also incorporate the optimization of the grid geometry by optimizing the number of sampling points and their positions. Point clouds constitute a convenient representation of SPECT images, which allows a significant reduction in the number of unknowns (reduces computation time, relaxes memory requirements and improves the stability of the solution) without loss in the image resolution and signal-to-noise ratio.

1.4. Synopsis

Some of the special data processing techniques used for the estimation of dynamic parameters directly from projections is presented in the following sections. The challenge is the accurate estimation of the blood input function. A key to making these techniques robust is the use of multi-resolution (multigridding) approaches to the spatiotemporal modeling of the tracer kinetics. There is significant interest in developing dedicated cardiac SPECT systems for acquisition of dynamics data. These data processing methods will become even more powerful with data acquired with new, dedicated cardiac SPECT cameras, as well as with currently available PET cameras. Finally, the development of hardware and data processing techniques for dynamic SPECT will play a significant role in diagnosing cardiovascular disease and diseases of other organs but will be especially important in preclinical evaluation of diagnostic and therapeutic methodologies in small animals.

2. Principles of tracer kinetic modeling

Tracer kinetic modeling is used in several areas of biological research to follow dynamic processes of blood flow, tissue perfusion, transport, metabolism and receptor binding. The underlying physical principle is conservation of mass wherein the input activity must be balanced by the accumulated activity and the output activity of a tracer within a system. The second principle is that, for a tracer experiment to reflect the true physiology of a biological system, that tracer must not itself perturb the system. These principles are reflected in many early contributions (Fick 1870, Stewart 1897, Hamilton *et al* 1928 and Kety and Schmidt 1948). Model equations developed from these principles and known physiology are found in Meier and Zierler (1954) and Zierler (1965). In these works, general equations were formulated to estimate flow using tracers for both the injection inflow/outflow detection technique and the injection inflow/residue detection technique (Bassingthwaighte *et al* 1993). An example of the injection inflow/outflow technique is found in the hanging heart experiment (Marshall *et al* 2001). Tracer exchange has been modeled down to the scale of actually calculating exchange between blood and extravascular spaces as a function of the length along the capillary (Rose *et al* 1977).

While physiologic studies in the past used direct sampling of input tracer concentration, tissue concentration and output concentration, it is possible to make all these measurements using external detection methods. Specifically, dynamic SPECT can be used to measure the time sequence of tracer content in tissues of the body from which physiologic parameters can be derived.

2.1. Principle of compartmentalization

The modeling of tracer kinetics relies on the principle of indicator dilution, whereby models are developed that compartmentalize the dilution of a measurable tracer that is introduced into the biological system to be studied in order to follow a physiologic or biochemical process of a particular biochemical substance (Huang and Phelps 1986). An appropriate tracer must be chosen to ensure that it follows the dynamic process of interest, it is measurable and it does not perturb the process being measured. The tracer is required to be of low mass concentration such that it does not affect any saturable process. Upon introduction, the tracer distributes throughout the sample. Measurements of the tracer are taken as a function of time.

The compartmentalization is based on *a priori* knowledge of structural or configurational information about the process or the organ system. Based on this information, a compartment model is developed that gives a mathematical description of the pathways and dynamic behavior of the tracer in the biological tissue of interest. The model is represented by a number of compartments (volumes where the tracer is uniformly distributed) (Huang and Phelps 1986) linked by arrows indicating transport between the various compartments or network that relates the compartments based on known or assumed physiology. The compartment may be a physical space such as an organ or may represent a metabolic or bound state of the tracer. The amount of tracer leaving a compartment is usually assumed to be proportional to the total amount in the compartment. The constant of proportionality (the rate constant) has the unit of inverse time and denotes the fraction of the tracer that is in one compartment that will leave the compartment per unit time. The kinetics between compartments are described by a system of differential equations. A general formulation and solution for n compartments is presented in Gunn *et al* (2001).

For example, assume that the concentration in the blood $B(t)$ is known. (Throughout we are going to assume that blood and plasma are the same. See section 2.3 for a discussion about the bias incurred when the tracer exchanges between red blood cells and the blood plasma.) The rate equation for the extravascular compartment (intracellular and extracellular space in the extravascular tissue, figure 5) with concentration $C_{\mathrm{EV}}(t)$ is

$$\frac{\mathrm{d}}{\mathrm{d}t}C_{\mathrm{EV}}(t) = -\frac{P_2 S}{V_{\mathrm{EV}}}C_{\mathrm{EV}}(t) + \frac{P_1 S}{V_{\mathrm{EV}}}B(t), \tag{1}$$

where V_{EV} is the volume of the extravascular compartment, P_1 and P_2 (in units of cm min^{-1}) are the permeability coefficients for flux out of and into the capillary, respectively, and $S(\mathrm{cm}^2)$ is the surface area of the capillary in the sampled voxel. Setting $K_1 = (P_1 S)/V_{\mathrm{EV}}$ and $k_2 = (P_2 S)/V_{\mathrm{EV}}$, the rate constants in and out of the extravascular compartment are in units of volume per minute per extravascular volume (V_{EV}). If $B(t)$ is the blood input, the value of K_1 includes flow as well as extraction. Throughout this review, we refer to it as flow times extraction. (In the literature, others have used the terminology ‘flow extraction product’.) Substituting K_1 and k_2 into equation (1), the differential equation describing the exchange between the blood and extravascular compartment can be rewritten as

$$\frac{\mathrm{d}}{\mathrm{d}t}C_{\mathrm{EV}}(t) = -k_2 C_{\mathrm{EV}}(t) + K_1 B(t), \tag{2}$$

where the rate of change in and out of the extravascular compartment is proportional to the concentration in the blood and in the extravascular compartment, respectively.

Note that blood is not considered a compartment. For a compartment, the change in concentration as a function of time is specified by a differential equation. In the applications presented in this review, blood is not specified by a differential equation but instead is estimated from the projection data. Also, the flow times extraction K_1 is specified using a capital letter instead of a lower case letter. Even though this is commonly found in the literature, some authors will still use a lower case letter. The parameter K_1 differs from k_2 in that it is a macro parameter (Gunn *et al* 2001), which is a function of flow (a global system parameter) and the rate of extraction of the tracer from the blood into the extravascular compartment. The parameter K_1 is generally more stable with respect to parameter estimation. We will see later that the estimation of k_2 involves nonlinear estimation but if known then K_1 can be estimated using linear estimation techniques (see section 4.2).

The amount of tracer in a volume of tissue can deviate significantly in value from the chemical concentration in individual spaces if the tracer does not distribute uniformly within all spaces in the tissue. Thus, the 'apparent distribution volume' V_D (see figure 6) is defined at equilibrium as the volume of space that a tracer would occupy in the tissue extravascular space V_{EV} with the same concentration as in the blood (Huang and Phelps 1986),

$$V_D = \lambda V_{\mathrm{EV}}, \tag{3}$$

where

$$\lambda = \frac{C_{\mathrm{EV}}(\infty)}{B(\infty)}.$$

Here, λ is known as the partition coefficient. The partition coefficient analogy comes from the fact that a tracer might have different solubilities in different tissue types.

Strictly speaking, one should define the distribution volume or partition coefficient only in terms of the definition given in equation (3). If we assume equilibrium, we can set equation (2) to zero, which implies that $K_1 B(\infty) = k_2 C_{\mathrm{EV}}(\infty)$ or the partition coefficient $\lambda = C_{\mathrm{EV}}(\infty)/B(\infty) = K_1/k_2$ and the distribution volume is $V_D = (K_1/k_2)\cdot V_{\mathrm{EV}}$. Distribution volume is a measure of how much is extracted by extravascular tissue at equilibrium. If a volume of tissue has no net extraction, it is zero; but if all the material is extracted like a microsphere, it is infinity. Thus the distribution volume concept is limited to situations where the wash-out rate is greater than 0. In the literature, the distribution volume may be given the same value as the partition coefficient by dropping the volume V_{EV} from the expression.

2.2. Compartment modeling of cardiac perfusion

It is assumed that $B(t)$ is known, either by fitting the input function to the measured projections or by measuring plasma samples (figure 7). In this case, we have a one-compartment model (figure 8) instead of a two-compartment model, since the kinetics of the blood are estimated using an independent model. Thus, the differential equation in equation (2) completely describes the kinetics of the model. It is assumed that the blood concentration measured in the left ventricular cavity represents the blood concentration of the particular radiopharmaceutical that is available to perfuse into the myocardium.

The activity concentration in the tissue at the time point t is modeled as

$$A_T(t) = f_v B(t) + (1 - f_v) C_{EV}(t), \tag{4}$$

where A_T is the model of the myocardial tissue activity concentration (e.g. MBq/cc) in the ROI, f_v is the vascular fraction of blood in the tissue, $B(t)$ is the measured activity concentration in the blood at time t, $C_{EV}(t)$ is the activity concentration in the extravascular compartment at time t and $(1 - f_v)$ is the fractional volume of the extravascular space. The blood activity concentration $B(t)$ is measured using an ROI drawn inside the left intraventricular cavity. The fractional blood volume f_v accounts for blood in the myocardium capillaries as well as spill-in from the ventricular cavities due to partial volume effects, scatter, and lung and cardiac motion. This can be as high as 35–45% in dynamic SPECT applications. The septum will contain spill-in from both right and left ventricular cavities, whereas the lateral wall of the left ventricle will contain contamination primarily from the left ventricular cavity. The spill-in varies with the tomographic resolution and motion compensation accuracy. There can also be significant contamination from scattered events detected from the liver since myocardial perfusion agents have high liver uptake. Using the RV cavity as a source for an input function does not work well because of the dispersion through the lungs, the time difference from RV to LV, and potential loss of tracer from the blood into the lungs.

The activity concentration $C_{EV}(t)$ from the extravascular compartment is given by the first-order ordinary differential equation in equation (2), which describes the kinetic exchange between the blood and the extravascular space for the compartment model shown in figure 8. If all concentrations are zero at $t = 0$, the solution to the differential equation in equation (2) is

$$C_{EV}(t) = K_1 C(t) \tag{5}$$

$$C(t) = \int_0^t e^{-k_2(t-\tau)} B(\tau)\, d\tau. \tag{6}$$

The transfer function (response to an impulse) for $C_{EV}(t)$ is $H_1(t) = K_1\, e^{-k_2 t}$ (Gunn *et al* 2001). The parameters K_1 and k_2 represent the respective wash-in and wash-out rate constants of the radiopharmaceutical. The units of K_1 and k_2 are (ml min^{-1})/(ml of extravascular space), but the units of K_1 and k_2 will be stated simply as min^{-1}. It is common in the literature to give units for K_1 as (ml g^{-1} min^{-1}). For tissue, a milliliter of tissue has a mass of approximately 1 g, therefore the units of min^{-1}.

The perfusion model presented here has been used to follow the dynamics of the myocardial perfusion agents ^{201}Tl, ^{99m}Tc-teboroxime and ^{99m}Tc-sestamibi. ^{201}Tl is a potassium analog that accumulates in myocardial cells by active transport associated with the Na^+/K^+ adenosine triphosphatase pump (Iida *et al* 2003). It primarily exchanges between the high concentration potassium pool in the cytoplasma of the myocytes and the lower concentration of potassium in the blood pool. ^{201}Tl has a high transcapillary extraction fraction and is rapidly cleared from arterial blood and taken up into myocardial tissue. Its half-life in the human subject can vary with the time dependent blood concentration. ^{99m}Tc-labeled sestamibi (Maublant *et al* 1992, Allman *et al* 1992, Williams and Taillon 1995, Gioia *et al* 1996, Maunoury *et al* 1996, Flamen *et al* 1995) is more widely used to image perfusion in clinical studies and in some cases is used with ^{201}Tl in rest(^{201}Tl)/stress(^{99m}Tc-sestamibi) protocols. Sestamibi has a biological half-life in the myocardium of 6 h. ^{99m}Tc-teboroxime (Leppo and Meerdink 1989, Leppo *et al* 1991, Rumsey *et al* 1992, Maublant *et al* 1993, Rosenspire *et al* 1993) is a boronic acid of technetium dioxime (BATO) complex that is

stable, neutral and lipid soluble. Teboroxime has the fastest clearance time (a 10–15 min half-life in the myocardium) (Leppo and Meerdink 1989) of the three tracers and is 90% extracted in the first pass. It is highly linear with flow. However, even though teboroxime is highly extracted on the first pass, there is an indication that extraction from subsequent passes may be affected by the binding of teboroxime to blood cells and plasma proteins (Rosenspire *et al* 1993), as well as by any changes it might undergo from the chloro to the hydroxide form, which has a lower affinity for the myocardium (Rumsey *et al* 1992). Dynamic cardiac SPECT studies (Smith *et al* 1994, 1996, Di Bella *et al* 2001) indicate that the wash-in rate constant for teboroxime is greater than that for thallium and in one case indicated that the wash-in rate constant for thallium ($K_1 = 0.44\ \text{min}^{-1}$) was half that for teboroxime ($K_1 = 0.94\ \text{min}^{-1}$) (Gullberg *et al* 1999). Thallium distributes as an analog of potassium, thus should follow the membrane polarization/depolarization activity. If this is compromised in ischemic tissues, the wash-in rate constant is expected to decrease. Research indicates that teboroxime has a lower degree of sensitivity to cellular metabolic impairment (Leppo *et al* 1991, Maublant *et al* 1993) when compared to sestamibi or ^{201}Tl.

It has been well recognized for years that ^{201}Tl imaging is a sensitive measure of tissue viability. Dynamic imaging of ^{201}Tl may prove to be an even more sensitive measure of tissue viability using volume of distribution measurements [$V_D = (K_1/k_2)$] instead of static imaging (Gullberg *et al* 2004). These studies indicated that the distribution volume of teboroxime was an indicator of tissue viability but that the distribution volume of thallium provided an even better contrast of tissue viability. Dynamic SPECT may simultaneously enable measurement of both cardiac tissue perfusion and tissue viability.

The one-compartment model shown in figure 8 assumes the following: (1) the time–activity curve of the blood can be measured independently of the extravascular compartment of the myocardial tissue, (2) all myocardial tissue regions exchange the tracer with blood, (3) the distribution of the tracer is homogeneous throughout the ROI and (4) the tissue ROI contains only regions of blood and extravascular compartments. In dynamic cardiac SPECT, the kinetic parameters are estimated for multiple 3D regions in the left ventricular myocardium.

Due to the low sensitivity of dynamic SPECT and the complexity of the physics of the image detection process, a one-compartment model is usually used to model perfusion in the heart. However, it has been proposed that a two-compartment model is more appropriate for ^{201}Tl kinetics and that it is important to sample plasma (blood void of red cells) to obtain an accurate input function (Eberl 2000). In some earlier work, two- and three-compartment models were used to model cardiac glucose and fatty acid metabolism of ^{123}I-labelled IPPA in cardiac studies (Gullberg *et al* 1999). However, there is the issue of which is the optimum model for the data presented (Coxson *et al* 1997). Recent cardiac metabolic studies (Okizakia *et al* 2007) have demonstrated that fewer compartments may be more optimal even though the kinetics are best represented by more than two compartments.

2.3. Blood and tissue time–activity functions

If the input function is measured from an intraventricular ROI, there are partial volume effects that contaminate the blood with adjacent tissue activity photons and the tissue with blood activity photons. The contamination of the blood data with tissue activity photons is especially evident with high liver uptake where there can be contamination (crosstalk), not only due to partial volume effects but also due to the background from scatter. Cardiac motion will also make it difficult to obtain a pure blood input function (Ross *et al* 1997a). Models of these effects were used to correct for the spillover of radioactivity both from the myocardium into the LV ROI and from the blood into the myocardial ROI in PET $H_2{}^{15}O$ flow studies (Iida *et al* 1991, 1992, 1995b). The partial volume effect in $H_2{}^{15}O$ studies was also measured using data from a $C^{15}O$ (effectively labeled red cells) intravascular study in

combination with the transmission data. Another problem is acquisition of the correct data from plasma versus from whole blood. If there is exchange of the tracer with blood cells but the wash-out is relatively slow, then measuring the blood time–activity curve in the ventricular cavity may provide the wrong input function for myocardial tissue unless the fraction trapped in the red cells is known. For ^{201}Tl myocardial perfusion studies, it has been shown that this can bias K_1 (Iida *et al* 2008). In the delineation of the tissue ROI, care is needed to avoid extending the borders beyond the anatomical myocardial volume. This too can increase the partial volume effect (Welch *et al* 1995b).

Imaging results can be improved by optimizing the shape and sampling intervals of the time activity curves. From linear system theory, it is important to match the spectrum of the input function to the frequency response of the organ (Chen 1984). One also needs to select an acquisition (sampling) interval long enough to maximize statistics but short enough to have the timing resolution necessary to accurately capture the time–activity curves during the first few minutes of rapid change in the tracer distribution. Optimization of time sampling intervals is important for achieving best estimates of kinetic parameters in terms of bias and variance. Measuring the input dynamics rapidly is probably more important than measuring organ dynamics rapidly. In SPECT, hardware limitations hinder achieving short acquisition intervals, which results in trade-offs between bias and variance. A study (Ross *et al* 1997b) has shown that longer acquisition intervals (10, 20, 40 s) result in the most accurate estimates of kinetic parameters when flow times extraction is high, such as during stress. At rest, with low statistics, a rapid infusion always provides optimal estimates of kinetic parameters. The smallest amount of bias is observed with a 10 s acquisition interval, and the smallest amount of variance is seen with a 20 s acquisition interval. When the count rates are doubled, longer infusions and shorter acquisition intervals provide more accurate estimates of kinetic parameters during a resting state. When flow times extraction is increased during stress, longer acquisition intervals result in better estimates, indicating that good statistics are more important than temporal sampling resolution when estimating fast kinetics.

To alleviate some of the problems of having to measure the input function either from the imaging data or from frequent arterial blood samples, it has been proposed to develop a library of input functions. It has been shown that population-based input functions calibrated with one or two blood samples could be used as the input function in brain blood flow studies using SPECT (Iida *et al* 1994, Onishi *et al* 1996). Also, library-based input functions could be used for measuring myocardial blood flow using ^{201}Tl (Eberl 2000). Another approach is to first fit the noisy blood sampled data to a physiological model of the input function, then use the fitted input function to estimate the kinetic model parameters (Feng *et al* 1993).

Methods of blind estimation eliminate the need to measure an input function. Blind estimation usually limits which kinetic parameters can be estimated absolutely. For the one-compartment model, the flow times extraction K_1 and the blood fraction f_v are not estimated absolutely (Di Bella *et al* 1999, Fluckiger *et al* 2009). This has also been studied for a three-compartment model (Riabkov and DiBella 2004).

Many of the issues discussed in this section have been studied for conventional methods of estimating kinetic parameters from time–activity curves generated from a dynamic sequence of reconstruction images. The focus of this review is the estimation of these kinetic parameters from projection measurements, and the same issues raised here will be important in the estimation of blood input time–activity curves and kinetic model parameters from projections.

2.4. Estimation of kinetic parameters

The goal of parameter estimation in dynamic SPECT is to extract quantitative physiologic information about organ function from dynamically measured data. Parameter estimation is a branch of mathematics and statistics (Zar 1984, Brownlee 1984, Deutsch 1965, Beck and Arnold 1977, Bard 1974) that involves the development of methods that make efficient use of data in the process of estimating parameters of mathematical models. The process of parameter estimation involves the interplay between experimental design, model specification and techniques of data collection (Carson 1986b). The collected data are used in the estimation process to produce parameter estimates of the model. On the basis of a statistical model of the data, the estimation procedure produces improved parameter estimates and statistical measures of their accuracy and precision. Careful statistical analysis and hypothesis testing of the results provide a feedback mechanism whereby the model, the data collection protocol and the parameter estimation process can be evaluated and modified.

The model is a mathematical formulation that uses a set of parameters that reflect local rates of physiologic transport and biochemical reactions. Because of physical complexities of the image detection process, the models used in dynamic cardiac SPECT must necessarily be relatively simple. The process of estimating the model parameters requires maximizing a likelihood function with a statistical model that appropriately represents the statistics in the data. In general, statistical models for the data can be very complex if the data are reconstructed time–activity curves that contain correlations between the curve values in both time and space. The maximization of the likelihood function may involve either nonlinear or linear methods to estimate the parameters (see below).

Careful analysis of the parameter estimates provides useful information about the appropriateness of the entire estimation process (Carson 1986b). Tests for goodness-of-fit can be used to determine whether the model has captured all of the deterministic characteristics of the data (Draper and Smith 1966, Dixon and Massey 1969, Brownlee 1984, Zar 1984). If the noise level is known, one quick and easy test is to determine whether the chi-square of the fit is equal to the number of degrees of freedom (see chapter 12 of Taylor (1982)).

2.4.1. Nonlinear methods—Model parameters are estimated directly from dynamically acquired SPECT projection data or from blood and tissue curves of a particular ROI estimated directly from projections. The process of estimating kinetic parameters of the compartment model is a nonlinear estimation problem (Deutsch 1965, Bard 1974). An iterative algorithm is used to solve the model parameters. If time–activity curves have been estimated, an iterative algorithm, such as that found in the computer software package RFIT (Huesman *et al* 1995), may be used to fit the model parameters so that the sampled time–activity curves in the tissue ROIs fit the predicted time–response curves of the model. The program estimates the model parameters and the statistical errors.

In the development presented later (see section 5), blood and tissue time–activity curves are estimated directly from the projection measurements. Because this function is known only from measurements of the dynamic reconstructions, it has statistical fluctuations. The kinetic parameters are estimated for each ROI by fitting the measured tissue data to a model of the dynamic emission tomographic reconstructions with a noisy input function (Huesman and Mazoyer 1987).

2.4.2. Linear methods—The Patlak method (Patlak *et al* 1983, Patlak and Blasberg 1985, Gambhir *et al* 1989, Kordower 2000, Choi *et al* 1991, 1993, Maguire *et al* 1997, Gill *et al* 2003, Wang *et al* 2008) is a linear approach to estimating kinetic parameters. The Patlak

analysis depends on irreversible trapping of at least a portion of the tracer. It is a simplified linear kinetic modeling technique that was originally developed as a graphic method performed by linear regression of time–activity curves (Patlak and Blasberg 1985). The method does not assume any particular kinetic model and involves only linear estimation techniques. The limiting slope of the Patlak plot is the uptake rate constant of the system (or the steady state response of the system), a very useful quantitative index for characterizing the kinetic properties of tracers. The Patlak method has been applied in the analysis of blood flow (Choi *et al* 1993), FDG kinetics (Choi *et al* 1991) and has found application in many disease studies (Gill *et al* 2003). The linear parameters of the Patlak model have also been estimated directly from projection data (Maguire *et al* 1997, Wang *et al* 2008).

The Logan method (Logan 2000) is another linear method that assumes the kinetics have reached an equilibrium. Whereas the Patlak method applies to irreversible systems, the Logan method applies to reversible systems. The method transforms the system of differential equations into a form in which the distribution volume is the slope of a linear equation, which in the case of a one-compartment model is K_1/k_2. The estimation of linear coefficients is much more straightforward than estimating the nonlinear parameters of kinetic compartment models.

3. Spatiotemporal modeling of dynamic image data

Spatiotemporal basis functions are the basic building blocks for modeling the variation in the reconstructed spatial distribution with time. Time-varying activity concentrations within volumes can be modeled by selecting a set of temporal basis functions that are capable of representing typical time variations and have desired smoothness properties. These may be splines, FADS, curves that fit compartment models, polynomial expansions or several other possible spectral decompositions. Similarly, the spatially nonuniform activity concentration within a particular volume can be modeled by selecting an appropriate set of spatial basis functions defined within the volume. These could be splines, point clouds of tetrahedral elements, blobs, various types of polynomial expansions or indicator functions corresponding to voxels. The number of basis functions and their spatial and temporal extents can be varied so that the spatiotemporal basis can optimally model the spatial and temporal content of the data with the fewest number of basis functions. This provides a multi-resolution structure that is ideal for estimating the parameters from projection data. Given a set of temporal basis functions and a set of spatial basis functions, coefficients for the resulting spatiotemporal basis functions can be estimated directly from the projections (Reutter *et al* 2000).

Mathematically, the activity distribution $A(x, t)$ in image space is modeled using the following spatiotemporal basis functions,

$$A(x,t)=\sum_{m,n} a_{mn} S^m(x) V^{mn}(t), \tag{7}$$

where $S^m(x)$, $m = 1, \ldots, M$, are spatial basis functions; $V^{mn}(t)$, $m = 1, \ldots, M$; $n = 1, \ldots, N$, are temporal basis functions and a_{mn} are the coefficients of the basis expansion. The temporal basis representation is generalized so that it is indexed with the spatial basis function $S^m(x)$.

Previously, we denoted $A_T(t)$ (equation (4)) to specify a particular one-compartment model for myocardial tissue. Here, we provide a general representation of the activity concentration as a function of space x and time t in terms of spatial and temporal basis functions. The following discussion provides examples of different selections of bases and includes

examples where the spatial and temporal basis functions are completely independent, being connected only by the coefficient indexed by both types of basis functions, whereas in equation (7) the temporal basis functions are dependent on the index of the spatial basis function.

The goal is to parameterize spatially non-uniform activity within segmented volumes and to include smooth temporal changes within volumes, and so provide 4D and 5D representations of dynamic reconstructions. The approach is to model continuous anatomy throughout continuous time rather than through the use of small image voxels at discrete time segments. This reduces the size of the parameter space and reduces noise. The following exposition contains some examples of temporal and spatial modeling using spatiotemporal basis functions.

The projections of the activity $A(x, t)$ are written as a function of the detector position d at time t (see figure 9),

$$P(d(t), t) = \int_{\chi} F[x, d(t)] A(x, t)\, \mathrm{d}x, \tag{8}$$

where $A(x, t)$ is the spatiotemporal distribution of tracer with $x \in$ image space χ. The weighting function $F[x, d(t)]$ maps the activity $A(x, t)$ into the projection $P(d, t)$ with detector position $d(t)$ at time t. Therefore, in terms of the spatiotemporal basis functions, the projections are expressed as

$$\begin{aligned} P(d(t), t) &= \int_{\chi} F[x, d(t)] \sum_{m,n} a_{mn} S^m(x) V^{mn}(t)\, \mathrm{d}x \\ &= \sum_{m,n} a_{mn} U^m(d(t), t) V^{mn}(t), \end{aligned} \tag{9}$$

where

$$U^m(d(t), t) = \int_{\chi} F[x, d(t)] S^m(x)\, \mathrm{d}x \tag{10}$$

is the projection of the spatial basis function $S^m(x)$ at the detector sampling position $d(t)$.

The projection data can be recorded as individual events of radioactive emissions of the radioisotope (list mode) or the accumulation of events in a detector bin $d_i(t)$ over the acquisition time interval Δt_k divided by Δt_k so that the value at all time points is in terms of activity concentration in units of counts per unit time. The projection at t_k in projection bin i is the activity acquired over time Δt_k,

$$p_i(t_k) = \int_{t_k - \Delta t_k}^{t_k} P(d_i(t), t)\, \mathrm{d}t \tag{11}$$

$$\begin{aligned} p_i(t_k) &= \int_{t_k - \Delta t_k}^{t_k} \int_{\chi} F[x, d_i(t)] A(x, t)\, \mathrm{d}x\, \mathrm{d}t \\ p_i(t_k) &= \int_{t_k - \Delta t_k}^{t_k} \sum_{m=1}^{M} \sum_{n=1}^{N} a_{mn} U^m(d_i(t), t) V^{mn}(t)\, \mathrm{d}t, \end{aligned} \tag{12}$$

where t_k, $k = 1, \ldots, K$ is the time at which the projection samples $p_i(t_k)$, $i = 1, \ldots, I$, are acquired (figure 9). The number of projection rays per projection angle is denoted by I. The

total number of time samples is K. This expression is a general parameterization of both space and time. This can be represented in matrix form as

$$p = Fa, \tag{13}$$

where p is an IK-element column vector of modeled dynamic projection data values, F is an $(I\,K) \times (MN)$ system matrix containing the elements

$$f_{ik(mn)} = \int_{t_k - \Delta t_k}^{t_k} U^m(d_i(t), t) V^{mn}(t)\, \mathrm{d}t, \tag{14}$$

a is an MN-element column vector of coefficients, I is the total number of projection measurements acquired by the SPECT detectors and MN is the number of basis functions that span the space and time to be reconstructed.

The forward projection operator F is a linear transformation from the image space with elements a into the projection space with elements p. The matrix F includes effects of the physics of the imaging detection process, which include attenuation (Gullberg *et al* 1985, 1989, King *et al* 1995, 1996), geometric response of the collimator (Tsui *et al* 1988, Zeng *et al* 1991, 1994, Formiconi *et al* 1989, Penney *et al* 1990, McCarthy and Miller 1991, van Elmbt and Walrand 1993, Glick *et al* 1994) and scatter (Welch *et al* 1995a, Zeng *et al* 1999, Bai *et al* 2000, Laurette *et al* 2000, Floyd *et al* 1985, Liang *et al* 1992, Frey and Tsui 1993, Meikle *et al* 1994, Beekman *et al* 1996, 2002, Kadrmas *et al* 1998). A photon is emitted by a radioactive nucleus traveling in all possible 4π directions. The geometric acceptance of the collimator holes is of the order of 10^{-5}. Also, the photon could be attenuated, meaning that it is not detected at all by the camera, or the photon could be scattered and detected incorrectly on the detector, thus making it unclear as to where the photon originated and blurring the projected image. These effects are modeled by the system matrix, such that the system matrix contains elements $f_{ik(mn)}$ that are proportional to the probability that the photon emitted from the support of the basis function $S^m(x)$ during the time t corresponding to the intersection of $(t_k - \Delta t_k, t_k)$ and the support of $V^{mn}(t)$ is detected in a projection bin i.

3.1. Spatial and temporal modeling using splines

The use of splines provides an efficient and accurate method of composing continuous functions from discrete samples. Cubic spline functions are probably the most popular. They form smooth functions from fitted data, and cubic spline interpolations do not exhibit oscillatory behavior that is characteristic of high-degree polynomial interpolation.

There are various examples where splines have been used to model dynamic data. Work was done in which five piecewise polynomial spline functions defined over four contiguous time segments were used to fit the blood input function (Chen *et al* 1991). The segments were determined by varying their endpoints in a prescribed fashion and using the set that yielded the smallest weighted sum of squared errors, averaged over 100 simulated data sets. Others (Nichols *et al* 1999) first calculated the temporal histogram for all of the data to model the time course of activity in voxels reconstructed from dynamic list-mode PET data. The segmented endpoints for cubic B-splines were defined by selecting a set that yielded approximately equal arc lengths along the resulting time–activity curve.

For the modeling of dynamic cardiac SPECT data, constant, linear, quadratic and cubic B-splines were compared (Reutter *et al* 2000). A basis of 16 B-splines (see figure 10) spanning 15 time segments that have geometrically increasing lengths were used such that the length

of the initial time segment was varied, and the errors in the time–activity curve estimates and the subsequent kinetic model parameter estimates were compared.

In the examples in section 5.1, the temporal spline representation will be independent of the spatial representation, i.e.

$$V^{mn}(t)=V^{n}(t). \tag{15}$$

Therefore, the model given in equation (7) can be represented as

$$A(x,t)=\sum_{m,n} a_{mn} S^{m}(x) V^{n}(t), \tag{16}$$

where the set of temporal basis functions is independent of each of the spatial basis functions and the coupling of the two basis functions is through the coefficients a_{mn}.

3.2. Temporal modeling using compartment models

Imposing a compartmental relationship (defined by a first-order differential equation) between blood and tissue activities into the spatiotemporal model will provide more temporal regularization than is provided by splines alone. The general temporal model has two components (blood and extravascular),

$$V^{mn}(t)=f_v^m V^n(t) \quad \text{(blood)} + (1-f_v^m) K_1^m \int_0^t V^n(\tau)\, e^{-k_2^m (t-\tau)} d\tau \quad \text{(extravascular)}, \tag{17}$$

where equation (17) is precisely a generalization of $A_T(t)$ in equations (4)–(6) in section 2 by coupling the temporal basis to a spatial basis with index m, and where f_v^m is the blood volume fraction, K_1^m is the wash-in rate constant, k_2^m is the wash-out rate constant for the tissue region m and $V^n(t)$ is a temporal basis function for a blood input function $B(t)=\sum_n a_n^B V^n(t)$. The spatiotemporal representation is

$$A(x,t)=\sum_{m,n} a_{mn} S^{m}(x) V^{mn}(t), \tag{7}$$

$$A(x,t)=\sum_{m,n} a_{mn} S^{m}(x) \left[f_v^m V^n(t) + (1-f_v^m) K_1^m C_{mn}(t;k_2^m) \right], \tag{18}$$

where

$$C_{mn}(t;k_2^m)=\int_0^t V^n(\tau)\, e^{-k_2^m (t-\tau)} d\tau. \tag{19}$$

In Reutter *et al* (2005), splines were used to model the blood input function and a physiological compartment model was used to model changes in activity for tissue volumes. In Kadrmas and Gullberg (2001), a compartment model was used as a Bayesian prior to constrain the time–activity curves for each voxel to fit a one-compartment model.

3.3. Temporal modeling using factors of dynamic structures (FADS)

Factor analysis of dynamic structures (FADS) (Barber 1980, Di Paola *et al* 1982, Buvat *et al* 1993, Sitek *et al* 2002a) is a semi-automatic technique used to extract time–activity curves from a series of dynamic images. In applying the method, the goal is to extract time–activity curves that are physiological in that they represent blood activity or an uptake and wash-out of a particular tissue region. The FADS method can separate partially overlapping regions that have different temporal behaviors (Nijran and Barber 1985, Nakamura *et al* 1989, Houston and Sampson 1997). FADS can also separate different physiological regions and automatically define regions in the image that have the highest concentrations of blood or tissue components. For cardiac studies, the estimation of factors from dynamic SPECT data was originally accomplished using a dynamic sequence of reconstructed images (Sitek *et al* 1999b, 2000, Hu *et al* 2008). However, the method has been shown to be effective in estimating factors directly from projection measurements as well (Hu *et al* 2008, Sitek *et al* 2001).

Factors are temporal functions that have physiological interpretation (one possibility is a blood input function) so that the elements of the factor curves are non-negative. In the factor model, it is assumed that activity in each tissue region m is a linear combination of factors. The general temporal model has the form

$$V^{mn}(t)=V^{n}(t)=\sum_{k=1}^{K}F_{nk}\chi_{k}(t), \tag{20}$$

where for each index n there is a factor F_{nk} ($k = 1, \ldots, K$) which is a discrete time–activity function, and $\chi_k(t)$ is a characteristic function with $\chi_k(t) = 1$ for $t_k - \Delta t_k \leq t \leq t_k$ and 0 otherwise. Note that for a given factor $V^n(t)$, this temporal model is the same for all spatial elements m. The total activity as a function of space and time can be written as

$$A(x,t)=\sum_{m,n}a_{mn}S^{m}(x)V^{n}(t), \tag{15}$$

$$A(x,t)=\sum_{m=1}^{M}\sum_{n=1}^{N}\sum_{k=1}^{K}a_{mn}F_{nk}S^{m}(x)\chi_{k}(t), \tag{21}$$

where M is the number of spatial basis functions (e.g., may be voxels), N is the number of factors and K is the number of time samples. Usually, the number of factors N is equal to the number of physiologic factors—that is, volumes exhibiting unique kinetics that are actually present in the medical image—but this need not always be the case (Nakajima *et al* 1991). Note that even though the representation in equation (21) is discrete in time and thus corresponds to a spline representation of zero order, higher order splines can also be used.

3.4. Summary

The material in this section presents the foundation for spatial and temporal representation of the evolution of *in vivo* physiological processes. An important aspect of the formulation is the flexibility to allow multigridding of both spatial and temporal domains in order to reduce the indeterminacy of the problem of estimating dynamic parameters directly from tomographic projection measurements. The next sections show how direct and semi-direct methods use the basic building blocks of spatiotemporal basis functions to estimate dynamic processes directly from dynamically acquired projection data. The ultimate goal is the

eventual quantification of physiological processes (perfusion, metabolic rate, etc) by estimating kinetic parameters of compartment models.

4. Estimation of kinetic model parameters from projections—direct methods

The time–activity curves and kinetic model parameters are estimated directly from dynamic SPECT projection data by modeling the spatial and temporal distributions of the radiopharmaceutical throughout the projected field-of-view for all time. In section 4.2, a compartmental model-based approach is presented for estimating kinetic parameters directly from projections. The organs are assumed segmented (see section 4.1) so that the blood input can be identified and the appropriate models can be formulated for each tissue type.

The segmentation step is not essential but it can reduce dimensionally and the accuracy of the procedure is critical in reducing bias. If the segmented ROI is larger than the desired organ of interest, there could be cross talk from other organs. If the other organ has lower counts, then the time–activity curve for the organ of interest will be too low. If the other organ has higher counts, then the time–activity curve will be too high. The effect on the bias would be the same as that experienced when manually sampling ROIs in the heart (Welch *et al* 1995b).

4.1. Segmentation

4.1.1. Static segmentation of ungated data using 4D differential boundary detection—The estimation process begins with an image segmented into blood pool, *S* tissue types of interest and background, as shown in figure 11. In this example, a differential 4D segmentation method was used to automatically create geometric models of the surfaces bounding volumes of time-varying tracer uptake in the myocardium, liver and body from dynamic SPECT images in a late time frame. This method was previously used to automatically segment the time-varying body and lung surfaces in human respiratory-gated PET transmission images (Reutter *et al* 1997). Bilinear interpolation is used to obtain sub-voxel spatial localization of the zero crossing points. In the output of a second directional derivative operator, the zero-crossing points are linked together to form contours in each spatial plane (Wallin 1991). These contours are linked together to form 3D surfaces. Information about the centroid, bounding box and average image intensity gradient across each contour, as well as each surface, is stored to facilitate identifying the surfaces. The myocardium, liver and body surfaces are identified as being relatively large surfaces associated with relatively high image intensity gradients. Data are analyzed efficiently in 4D over appropriate spatial and temporal scales to extract and to physically model the surfaces bounding volumes of time-varying tracer uptake. This structured analysis imposes spatial and temporal continuity that complement the information which is available from unstructured image voxel intensity alone.

4.1.2. Dynamic segmentation of cardiac-gated data using level sets—The organ boundaries can also be determined using level set methodology (Osher and Sethian 1988, Sethian 1996, Osher and Fedkiw 1999), which is a simple method for computing and analyzing motion of a surface in two or three dimensions. The surface is specified as the zero level set of a smooth function. This approach allows importation of mechanical constraints, and it simultaneously segments organ boundaries and estimates model parameters of changing activity concentration (Shi and Karl 2003, Feng *et al* 2003b, Shi and Karl 2004).

4.2. Compartmental model-based approach

From the segmentation into anatomical structures of blood, background and myocardial tissue, the activity is modeled by the following spatiotemporal basis functions,

$$A(x,t)=B(t)\chi_B(x) \quad \text{(blood pool)}+gB(t)\chi_G(x) \quad \text{(background tissue)}+\sum_m a_m^T S^m(x)A_T^m(t) \quad \text{(myocardial tissue)}, \tag{22}$$

where $\chi_B(x)$ and $\chi_G(x)$ are characteristic functions for the segmented blood pool and background defined on the entire image, i.e. these functions equal 1 if x is an element of the region and zero otherwise. Also, it is assumed that the background tissue follows some constant fraction g of the blood input.

For a one-compartment kinetic model (figure 8, equation (4)), the expression for the uptake in the tissue type m is

$$A_T^m(t)=f_v^m B(t)+(1-f_v^m)C_{\mathrm{EV}}^m(t;K_1^m,k_2^m), \tag{23}$$

where

$$C_{\mathrm{EV}}^m(t;K_1^m,k_2^m)=K_1^m C_m(t;k_2^m)$$

and K_1^m is the wash-in parameter, f_v^m is the fraction of blood in the tissue and $C_m(t;k_2^m)$ is given by

$$C_m(t;k_2^m)=\int_0^t B(\tau)\,\mathrm{e}^{-k_2^m(t-\tau)}\mathrm{d}\tau,$$

where k_2^m is the wash-out parameter and $B(\tau)$ is the blood input function. In the following, the blood input function is parameterized by the expression

$$B(t)=\sum_n a_n^B V^n(t), \tag{24}$$

where $V^n(t)$ the temporal basis functions and a_n^B are coefficients of the expansion for $B(t)$. Therefore

$$C_m(t;k_2^m)=\sum_n a_n^B C_{mn}(t;k_2^m), \tag{25}$$

where

$$C_{mn}(t;k_2^m)=\int_0^t V^n(\tau)\,\mathrm{e}^{-k_2^m(t-\tau)}\mathrm{d}\tau \tag{19}$$

and

$$A_T^m(t)=f_v^m\sum_n a_n^B V^n(t)+(1-f_v^m)K_1^m\sum_n a_n^B C_{mn}(t;k_2^m) \tag{26}$$

$$A_T^m(t)=f_v^m\sum_n a_n^B V^n(t)+(1-f_v^m)K_1^m C_m(t;k_2^m). \tag{27}$$

Substituting this expression for $A_T^m(t)$ and the expression for $B(t)$ in equation (24) into equation (22) gives

$$\begin{aligned}A(x,t)=&\sum_n a_n^B V^n(t)\chi_B(x)\quad\text{(blood pool)}+\sum_n g a_n^B V^n(t)\chi_G(x)\quad\text{(background tissue)}\\&+\sum_m\left(f_v^m\sum_n a_n^B V^n(t)+(1-f_v^m)K_1^m C_m(t;k_2^m)\right)\chi_m(x)\quad\text{(myocardial tissue)},\end{aligned} \tag{28}$$

where the spatial basis functions in equation (22) are assumed to be $a_m^T S^m(x)=\chi_m(x)$, i.e. the spatial basis functions are taken to be voxels or tissue regions of unit weight.

The projections are written as a function of detector position d at time t (figure 9)

$$P(d(t),t)=\int_\chi F[x,d(t)]A(x,t)\,\mathrm{d}x, \tag{8}$$

where $A(x, t)$ is the spatiotemporal distribution of the tracer with $x \in$ image space χ. From the segmented image, a model of the attenuation distribution is created and the attenuated unit activity projections of the blood pool, tissue and background regions are calculated for each projection ray of each projection angle. That is, the number of events that would be detected from each region, given a unit concentration of activity within the region, is calculated for each projection bin acquired at each projection angle.

Substituting the expression for $A(x, t)$ in equation (28) into equation (8) gives the following expression for the projection,

$$\begin{aligned}P(d(t),t)=&\sum_n a_n^B V^n(t)\int_\chi \chi_B(x)F[d(t),x]\,\mathrm{d}x\quad\text{(blood pool)}+\sum_n g a_n^B V^n(t)\int_\chi \chi_G(x)F[d(t),x]\,\mathrm{d}x\quad\text{(background tissue)}+\sum_m\Bigg(f_v^m\sum_n a_n^B V^n(t)+(1-\\&P(d(t),t)=\sum_n a_n^B V^n(t)U^B(d(t),t)\quad\text{(blood pool)}+\sum_n g a_n^B V^n(t)U^G(d(t),t)\quad\text{(background tissue)}+\sum_m\Bigg(f_v^m\sum_n a_n^B V^n(t)+(1-f_v^m)\end{aligned} \tag{29}$$

$$U^B(d(t),t)=\int_\chi \chi_B(x)F[d(t),x]\,\mathrm{d}x \tag{30}$$

$$U^G(d(t),t)=\int_\chi \chi_G(x)F[d(t),x]\,\mathrm{d}x \tag{31}$$

$$U^m(d(t),t)=\int_\chi \chi_m(x)F[d(t),x]\,\mathrm{d}x. \tag{32}$$

The sampling of the data can be very irregular in time. Therefore, it is assumed that the time t_k specifies some projection angle $\theta(t_k)$. The model does not imply that the detector needs to

be stationary or that the tracer distribution is constant during the time interval Δt_k. The projection $p_i(t_k)$, $i = 1, \ldots, I$ is the activity acquired over a time Δt_k for projection bin i,

$$p_i(t_k)=\int_{t_k-\Delta t_k}^{t_k} P(d_i(t), t)\,\mathrm{d}t. \tag{11}$$

Substituting $P(d_i(t), t)$ from equation (29) into equation (11),

$$p_i(t_k)=\int_{t_k-\Delta t_k}^{t_k}\left[\sum_n a_n^B V^n(t)U^B(d_i(t), t)+g a_n^B V^n(t)U^G(d_i(t), t)\right]\mathrm{d}t+\int_{t_k-\Delta t_k}^{t_k}\left[\sum_m\left(f_v^m\sum_n a_n^B V^n(t)+(1-f_v^m)K_1^m C_m(t;k_2^m)\right)U^m(d_i(t),$$

$$p_i(t_k)=\sum_n a_n^B\int_{t_k-\Delta t_k}^{t_k} V^n(t)U^B(d_i(t), t)\,\mathrm{d}t+\sum_n g a_n^B\int_{t_k-\Delta t_k}^{t_k} V^n(t)U^G(d_i(t), t)\,\mathrm{d}t+\sum_m f_v^m\sum_n a_n^B\int_{t_k-\Delta t_k}^{t_k} V^n(t)U^m(d_i(t), t)\,\mathrm{d}t+\sum_m(1-f_v^m)K_1^m\sum_n a_n^B\int_{t_k-\Delta t_k}^{t_k} C_m$$

Note: $C_m(t;k_2^m)=\sum_n a_n^B C_{mn}(t;k_2^m)$ from equation (25). Simplifying

$$p_i(t_k)=\sum_n a_n^B u_i^n(t_k)+\sum_n g a_n^B v_i^n(t_k)+\sum_m\sum_n f_v^m a_n^B w_i^{mn}(t_k)+\sum_m\sum_n(1-f_v^m)K_1^m a_n^B\Gamma_i^{mn}(t_k;k_2^m), \tag{33}$$

where

$$u_i^n(t_k)=\int_{t_k-\Delta t_k}^{t_k} V^n(t)U^B(d_i(t), t)\,\mathrm{d}t \tag{34}$$

$$v_i^n(t_k)=\int_{t_k-\Delta t_k}^{t_k} V^n(t)U^G(d_i(t), t)\,\mathrm{d}t \tag{35}$$

$$w_i^{mn}(t_k)=\int_{t_k-\Delta t_k}^{t_k} V^n(t)U^m(d_i(t), t)\,\mathrm{d}t, \tag{36}$$

$$\begin{aligned}\Gamma_i^{mn}(t_k;k_2^m)&=\int_{t_k-\Delta t_k}^{t_k} C_{mn}(t;k_2^m)U^m(d_i(t), t)\,\mathrm{d}t\\ \Gamma_i^{mn}(t_k;k_2^m)&=\int_{t_k-\Delta t_k}^{t_k}\int_0^t V^n(t)\,\mathrm{e}^{-k_2^m(t-\tau)}U^m(d_i(t), t)\,\mathrm{d}\tau\,\mathrm{d}t.\end{aligned} \tag{37}$$

Note $C_{mn}(t;k_2^m)=\int_0^t V^n(\tau)\,\mathrm{e}^{-k_2^m(t-\tau)}\mathrm{d}\tau$ from equation (19). Rearranging the summations and bringing the summation over n outside, the expression for the projection bin i at t_k is given as

$$p_i(t_k)=\sum_n a_n^B\left[u_i^n(t_k)+g v_i^n(t_k)+\sum_m(f_v^m w_i^{mn}(t_k)+(1-f_v^m)K_1^m\Gamma_i^{mn}(t_k;k_2^m))\right]. \tag{38}$$

The constants $u_i^n(t_k)$, $v_i^n(t_k)$ and $w_i^{mn}(t_k)$ are pure geometrical weighting factors for blood, background and tissue type m, respectively. These equations are linear in the unknowns g, K_1^m and f_v^m. The nonlinear parameters k_2^m are contained in $\Gamma_i^{mn}(t_k;k_2^m)$. For a list mode acquisition, these weighting factors become more precise as a function of the event arrival time.

In the following equation, (38) is reformulated as a matrix equation. The wash-out parameters are elements of the vector

$$\lambda=[k_2^1,\ldots,k_2^m]^T, \tag{39}$$

the multiplicative parameters are elements of the vector

$$\mu=[f_v^1,\ldots,f_v^M,(1-f_v^1)K_1^1,\ldots,(1-f_v^M)K_1^M]^T \tag{40}$$

and the parameters of the unknown blood input function are elements of the vector

$$\beta=[a_1^B,\ldots,a_N^B]^T. \tag{41}$$

From the segmented image, the projections of the activity of the blood pool, tissue and background regions along each projection ray for each projection angle are modeled. At a particular time t_k (corresponding to a particular projection angle acquired during a particular rotation), the projections of the activity in the blood pool, background and tissue type m along each of the I projection rays are represented by the vectors

$$p(t_k)=[p_1(t_k),\ldots,p_I(t_k)]^T. \tag{42}$$

The total projection samples are represented by the vector

$$p=[p_1(t_1),\ldots,p_I(t_1),\ldots,p_1(t_k),\ldots,p_I(t_k)]^T. \tag{43}$$

Thus, a set of $I\cdot K$ equations can be written as

$$\sum_n a_n^B[R_n\mu+u^n+gv^n]=p, \tag{44}$$

where

$$R_n=\begin{bmatrix} w_1^{1n}(t_1) & \cdots & w_1^{Mn}(t_1) & \Gamma_1^{1n}(t_1;k_2^1) & \cdots & \Gamma_1^{Mn}(t_1;k_2^M) \\ \vdots & \cdots & \vdots & \vdots & \cdots & \vdots \\ \vdots & \cdots & \vdots & \vdots & \cdots & \vdots \\ w_I^{1n}(t_1) & \cdots & w_I^{Mn}(t_1) & \Gamma_I^{1n}(t_1;k_2^1) & \cdots & \Gamma_I^{Mn}(t_1;k_2^M) \\ \vdots & \cdots & \vdots & \vdots & \cdots & \vdots \\ \vdots & \cdots & \vdots & \vdots & \cdots & \vdots \\ w_1^{1n}(t_K) & \cdots & w_1^{Mn}(t_K) & \Gamma_1^{1n}(t_K;k_2^1) & \cdots & \Gamma_1^{Mn}(t_K;k_2^M) \\ \vdots & \cdots & \vdots & \vdots & \cdots & \vdots \\ \vdots & \cdots & \vdots & \vdots & \cdots & \vdots \\ w_I^{1n}(t_K) & \cdots & w_I^{Mn}(t_K) & \Gamma_I^{1n}(t_K;k_2^1) & \cdots & \Gamma_I^{Mn}(t_K;k_2^M) \end{bmatrix} \tag{45}$$

$$u^n=[u_1^n(t_1),\ldots,u_I^n(t_1),\ldots,u_1^n(t_K),\ldots,u_I^n(t_K)]^T, \tag{46}$$

$$v^n=[v_1^n(t_1),\ldots,v_I^n(t_1),\ldots,v_1^n(t_K),\ldots,v_I^n(t_K)]^T. \quad (47)$$

This gives

$$[R_1\mu+u^1+gv^1,\ldots,R_N\mu+u^N+gv^N]\beta=p, \quad (48)$$

or

$$R(\lambda,\mu,g)\beta=p, \quad (49)$$

where

$$R(\lambda,\mu,g)=[R_1\mu+u^1+gv^1,\ldots,R_N\mu+u^N+gv^N]. \quad (50)$$

To determine estimates of the model parameter vectors λ and μ, the background constant factor g and the input parameters β, the weighted sum of squares is minimized,

$$\chi^2(\lambda,\mu,g,\beta)=(\tilde{p}-R(\lambda,\mu,g)\beta)^T W(\tilde{p}-R(\lambda,\mu,g)\beta), \quad (52)$$

where $\tilde{p}$ are the measured projection data and the matrix W contains the weighting factors. Typically, W is either the inverse of the covariance matrix for the residual vector $\tilde{p}-R(\lambda,\mu,g)\beta$ or an identity matrix (for an unweighted least-squares fit).

Previously, efficient estimates of dynamic cardiac SPECT kinetic parameters of a one-compartment cardiac perfusion model were obtained using weighted least-squares estimates of dynamic reconstructions that were obtained from the inversion of the Fisher information matrix (Gullberg *et al* 1999, Kadrmas *et al* 1999). Each reconstruction in the dynamic sequence was implemented using matrix inverse reconstruction. The reconstruction was a solution to a weighted least-squares optimization problem (where the weights were equal to the measured projections assuming these to be the variances of a Poisson distribution), which provided a weighted least-squares estimate of the reconstructed values and estimates of the covariances between the reconstructed values. These estimates were used to generate time–activity curves for (1) activity in a blood region inside the left ventricle and a cardiac tissue region, (2) the variance of the two estimates of the sums in the two regions and (3) the covariance between the two ROI estimates. The weighted least-squares estimates and covariances for the reconstructed time–activity curves were fitted to a one-compartment perfusion model to obtain weighted least-squares estimates of the kinetic model parameters (wash-in, wash-out and fractional blood volume). It was shown that the weighted least-squares estimates of the kinetic model parameters gave lower variance than the unweighted least-squares estimates. Typically, the image matrices are large and, therefore, it is difficult to invert the Fisher information matrix to obtain a weighted least-squares estimate of the reconstruction and the covariance matrix. Typically, the sequence of reconstructions is obtained using ML (Lange and Carson 1984) or MAP (Levitan and Herman 1987) iterative algorithms, which properly model the Poisson statistics and the physics of the data acquisition. Work by Barrett *et al* (1994), Fessler (1996), Wang and Gindi (1997), Qi and Leahy (2000), Stayman and Fessler (2000) and Qi (2003) has developed formulas for estimating the errors in the reconstructions obtained from iterative reconstruction algorithms.

The appealing thing about estimating the kinetic parameters from projections is that the weighting matrix in equation (52) is directly related to the measurement errors, which are often assumed to be independent Poisson random variables with variance equal to the measured data provided the manufacturer has not preprocessed the data.

If the input function is known, then the least-squares problem can be simplified (Huesman *et al* 1998, Gullberg *et al* 1999). It has been shown that, if there is no wash-out from the compartment, that is, $k_2^m=0$, the estimation from projections can be reduced to a linear estimation problem (Vanzi *et al* 2004).

In some cases, the wash-out parameters k_2^m associated with a one-compartment model may be known then the multiplicative parameters associated with the model can be estimated directly using linear estimation methods. Compartmental modeling imposes constraints on the relationship between blood and tissue time–activity curves. For example, if the tracer or radiopharmaceutical is a physical or a chemical microsphere that is trapped in blood capillaries, within the cell or on a surface membrane protein, then it would be natural to let k_2^m be zero. With agents such as ^{123}I-iodorotenone and ^{99m}Tc-sestamibi, the wash-out is very slow and in the early phase of the study it can be assumed that the wash-out parameter is zero. This is the case when the data acquisition may not be extended long enough to acquire the wash-out phase of the tracer.

4.3. 4D maximum a posteriori reconstruction of dynamic data (one-compartment model for every voxel)

In the previous section, segmentation was performed to obtain like tissue regions for fitting a compartment model from projections. This was done to reduce the dimensionality of the problem. Another approach is to allow each voxel to be a separate tissue region that is constrained to fit a compartment model. Every voxel can be constrained to fit a compartment model given in equation (4). If the voxel is in the intraventricular cavity, for example, then f_v in equation (4) will be 1.00. This approach significantly increases the dimensionality of the problem from that of the previous section.

The activity distribution in each voxel m is represented by spatiotemporal basis functions

$$A(x,t)=\sum_m \chi_m(x)[f_v^m B(t)+(1-f_v^m)C_m(t)] \tag{53}$$

$$A(x,t)=\sum_m \chi_m(x)\left[f_v^m \sum_n a_m^B V^n(t)+(1-f_v^m)K_1^m \sum_n a_n^B C_{mn}(t;k_2^m)\right]. \tag{54}$$

The projection equations are

$$p_i(t_k)=\sum_m \sum_n f_v^m a_n^B w_i^{mn}(t_k)+\sum_m \sum_n (1-f_v^m)K_1^m a_n^B \Gamma_i^{mn}(t_k;k_2^m), \tag{55}$$

where the $p_i(t_k)$ are the modeled projections, f_v^m are the fraction of blood in tissue m, a_n^B are the linear coefficients associated with the blood temporal basis functions $V^n(t)$, $w_i^{mn}(t_k)$ are given in equation (36) and $\Gamma_i^{mn}(t_k;k_2^m)$ are given in equation (37).

As in section 4.2, the solution (a, f_v, K_1, k_2) can be determined by minimizing the weighted sum of squares function,

$$\chi^2(a^B, f_v, K_1, k_2)=\sum_{k=1}^{K}\sum_{i=1}^{I}\frac{(\tilde{p}_i(t_k)-p_i(t_k))^2}{1/W_{ik}}, \tag{56}$$

where $\tilde{p}_i(t_k)$ are the measured projections, W_{ik} are the weighting factors, I is the number of projection rays per angle and K is the number of projection samples over all time. The weighting factors are either unity for an unweighted fit or the reciprocal of the estimated variances of the projections for a weighted fit.

Instead of solving equation (56), consider the application of Bayes' theorem,

$$P(A(x,t)|\tilde{p})=\frac{P(\tilde{p}|A(x,t))\cdot P(A(x,t))}{P(\tilde{p})}, \tag{57}$$

where the probability density function $P(A(x, t))$ is

$$P(A(x,t))=\prod_{k=1}^{K}\prod_{m=1}^{M}\frac{1}{\sqrt{2\pi\sigma_{mk}}}\exp[-(A_T^m(t_k)-\bar{\mu}_{mk})^2/2\sigma_{mk}^2] \tag{58}$$

and

$$A_T^m(t_k)=f_v^m\sum_n a_n^B V^n(t_k)+(1-f_v^m)K_1^m\sum_n a_n^B C_{mn}(t_k;k_2^m) \tag{59}$$

is the activity at time t_k in tissue type m for an assumed one-compartment model, $\bar{\mu}_{mk}$ is the mean activity for tissue type m at time t_k and σ_{mk}^2 is the variance for the activity for tissue type m at time t_k. Equation (58) imposed an *a priori* constraint on the solution.

The likelihood function in equation (57) can be written as

$$P(\tilde{p}|A(x,t))=\prod_{k=1}^{K}\prod_{i=1}^{I}e^{-p_i(t_k)}\frac{[p_i(t_k)]^{\tilde{p}_i(t_k)}}{\tilde{p}_i(t_k)!}, \tag{60}$$

where

$$p_i(t_k)=\sum_m\sum_n f_v^m a_n^B w_i^{mn}(t_k)+\sum_m\sum_n(1-f_v^m)K_1^m a_n^B\Gamma_i^{mn}(t_k;k_2^m). \tag{61}$$

Substituting equation (61) into the following expression for the *a posteriori* probability distribution in equation (57),

$$P(A(x,t)|\tilde{p})=\frac{\left[\prod_{k=1}^{K}\prod_{i=1}^{I}e^{-p_i(t_k)}\frac{[p_i(t_k)]^{\tilde{p}_i(t_k)}}{\tilde{p}_i(t_k)!}\right]}{P(\tilde{p})}\times\prod_{k=1}^{K}\prod_{m=1}^{M}\frac{1}{\sqrt{2\pi}\sigma_{mk}}\exp[-(A_T^m(t_k)-\bar{\mu}_{mk})^2/2\sigma_{mk}^2], \tag{62}$$

and taking the natural logarithm gives

$$\begin{aligned}\Phi(a^B, f_v, K_1, k_2) &= \ln[P(A(x,t)|\tilde{p})] \\ &= \sum_{k=1}^{K}\sum_{i=1}^{I}\left\{\tilde{p}_i(t_k)\ln\left[\sum_m\sum_n f_v^m a_n^B w_i^{mn}(t_k) + \sum_m\sum_n (1-f_v^m)K_1^m a_n^B \Gamma_i^{mn}(t_k;k_2^m)\right]\right. \\ &\quad - \sum_m\sum_n f_v^m a_n^B w_i^{mn}(t_k) \\ &\quad \left. - \sum_m\sum_n (1-f_v^m)K_1^m a_n^B \Gamma_i^{mn}(t_k;k_2^m) - \ln(p(t)!)\right\} \\ &\quad + \sum_{k=1}^{K}\sum_{m=1}^{M}\left[\ln\left(\frac{1}{\sqrt{2\pi}\sigma_{mk}}\right) - \frac{(A_T^m(t_k)-\bar{\mu}_{mk})^2}{2\sigma_{mk}^2}\right] - \ln(P(p)).\end{aligned} \tag{63}$$

The $(\hat{a}^B, \hat{f}_v \hat{f}_1, \hat{k}_2)$that maximizes equation (63) can be determined by directly maximizing equation (63) using an optimization algorithm such as the conjugate gradient algorithm, or using an ordered-subset implementation of the expectation-maximization approach to maximizing the *a posteriori* probability distribution in equation (57) (Kadrmas and Gullberg 2001).

4.4. Spectral approach (multi-compartment model for every voxel)

Suppose the tissue region *m* satisfies a multi-compartment model instead of a one-compartment model assumed in sections 4.2 and 4.3. One could specify the model for the tissue region by specifying the number of compartments (Gunn *et al* 2001), or allow it to be a spectrum of exponentially decaying factors (Cunningham and Jones 1993). This is a more general parameterization of the kinetics, independent of any particular compartment model architecture that allows for a series of exponential terms with linear coefficients. The spectral analysis involves the estimation of the coefficients of these pre-selected exponential functions. This approach allows convenient solutions via linear methods.

Suppose that each tissue region has a transfer function $H_m(t)$. For a one-compartment model, $H_m(t)=K_1^m\,\mathrm{e}^{-k_2^m t}$. For several compartments, the transfer function would be a sum of several exponentials, $H_m(t)=\sum_{r=1}^{R}\gamma_r^m\,\mathrm{e}^{-\lambda_r t}$Gunn *et al* (2001). Note that here we do not identify a λ_r with a tissue region *m* but instead allow the coefficient γ_r^m to give the appropriate weight to the exponential with a decay constant λ_r. One could also write this as $H_m(t)=\sum_{r=1}^{R}\gamma_r^m\,\mathrm{e}^{-\lambda_r^m t}$ where the exponential basis functions change from tissue region to tissue region. The coefficients γ_r^m of the basis functions are all greater than or equal to $0{:}\gamma_r^m \geq 0$, the decay constants are bounded below by the decay constant λ of the radioisotope, $\lambda \leq \lambda_r^m \leq 1$, and *R* is the maximum number of basis functions allowed in the model. The problem is determining the values of γ_r^m that best fit the measured data given predefined values for λ_r^m. We know from Gunn *et al* (2001) that $K_1^m=\sum_{r=1}^{R}\gamma_r^m$. In the case of a one-compartment model, λ_r^m provide a spectral representation of k_2^m in a particular region or voxel.

In the following formulation, it is assumed that each voxel or tissue region has a transfer function specified by a series of exponentials. The tissue time–activity curve $A_T^m(t)$ for the voxel *m* is modeled as a fraction f_v^m of the arterial blood time–activity function $B(t)=\sum_n a_n^B V^n(t)$ plus a linear combination of single exponential basis functions in time,

convolved with the same arterial blood function $B(t)$. The expression for uptake in voxel m is

$$A_T^m(t)=f_v^m B(t)+(1-f_v^m)C_{\mathrm{EV}}^m(t;\gamma^m,\lambda^m), \tag{64}$$

where γ^m and λ^m are vectors $\gamma^m=(\gamma_1^m,\ldots,\gamma_R^m)$ and $\lambda^m=(\lambda_1^m,\ldots,\lambda_R^m)$ and

$$C_{\mathrm{EV}}^m(t;\gamma^m,\lambda^m)=\int_0^t B(\tau)\sum_{r=1}^R \gamma_r^m\, \mathrm{e}^{-\lambda_r^m(t-\tau)}\mathrm{d}\tau. \tag{65}$$

Substituting $B(\tau)=\sum_n a_n^B V^n(\tau)$, we obtain

$$C_{\mathrm{EV}}^m(t;\gamma^m,\lambda^m)=\sum_n a_n^B \sum_{r=1}^R \gamma_r^m C_{mn}^r(t;\lambda_r^m), \tag{66}$$

where

$$C_{mn}^r(t;\lambda_r^m)=\int_0^t V^n(\tau)\,\mathrm{e}^{-\lambda_r^m(t-\tau)}\mathrm{d}\tau. \tag{67}$$

The projection equations for activity accumulated over $[t_k-\Delta t_k,\ t_k]$ are expressed as

$$P(d(t),t)=\int_\chi F[x,d(t)]A(x,t)\,\mathrm{d}x, \tag{8}$$

$$p_i(t_k)=\int_{t_k-\Delta t_k}^{t_k} P(d_i(t),t)\,\mathrm{d}t. \tag{11}$$

For the activity in equation (64), the projection is

$$p_i(t_k)=\sum_m\sum_n f_v^m a_n^B w_i^{mn}(t_k)+\sum_m\sum_n (1-f_v^m)a_n^B\sum_{r=1}^R \gamma_r^m \Gamma_i^{mnr}(t_k;\lambda_r^m), \tag{68}$$

where $w_i^{mn}(t_k)$ is given in equation (36) and

$$\Gamma_i^{mnr}(t_k;\lambda_r^m)=\int_{t_k-\Delta t_k}^{t_k} C_{mn}^r(t;\lambda_r^m)U^m(d_i(t),t)\,\mathrm{d}t \tag{69}$$

$$\Gamma_i^{mnr}(t_k;\lambda_r^m)=\int_{t_k-\Delta t_k}^{t_k}\int_0^t V^n(\tau)\,\mathrm{e}^{-\lambda_r^m(t-\tau)}U^m(d_i(t),t)\,\mathrm{d}\tau\,\mathrm{d}t. \tag{70}$$

Rearranging terms in equation (68), we have

$$p_i(t_k)=\sum_n a_n^B \sum_m \left(f_v^m w_i^{mn}(t_k)+(1-f_v^m)\sum_{r=1}^{R}\gamma_r^m \Gamma_i^{mnr}(t_k;\lambda_r^m)\right). \tag{71}$$

The total projection samples are represented by the vector

$$p=[\,p_1(t_1),\ldots,p_I(t_1),\ldots,p_1(t_K),\ldots,p_I(t_K)]^T. \tag{72}$$

Thus, a set of $I \cdot K$ equations can be written as

$$\sum_n a_n^B [R_n(\lambda)\mu]=p, \tag{73}$$

where

$$R_n(\lambda)=\begin{bmatrix} w_1^{1n}(t_1) & \cdots & w_1^{Mn}(t_1) & \Gamma_1^{1n1}(t_1;\lambda_1^1) & \cdots & \Gamma_1^{1nR}(t_1;\lambda_R^1) & \cdots & \Gamma_1^{Mn1}(t_1;\lambda_1^M) & \cdots & \Gamma_1^{MnR}(t_1;\lambda_R^M) \\ \vdots & \cdots & \vdots & & \vdots & & \cdots & & \vdots & \\ \vdots & \cdots & \vdots & & \vdots & & \cdots & & \vdots & \\ w_I^{1n}(t_1) & \cdots & w_I^{Mn}(t_1) & \Gamma_I^{1n1}(t_1;\lambda_1^1) & \cdots & \Gamma_I^{1nR}(t_1;\lambda_R^1) & \cdots & \Gamma_I^{Mn1}(t_1;\lambda_1^M) & \cdots & \Gamma_I^{MnR}(t_1;\lambda_R^M) \\ \vdots & \cdots & \vdots & & \vdots & & \cdots & & \vdots & \\ \vdots & \cdots & \vdots & & \vdots & & \cdots & & \vdots & \\ w_1^{1n}(t_K) & \cdots & w_1^{Mn}(t_K) & \Gamma_1^{1n1}(t_K;\lambda_1^1) & \cdots & \Gamma_1^{1nR}(t_K;\lambda_R^1) & \cdots & \Gamma_1^{Mn1}(t_K;\lambda_1^M) & \cdots & \Gamma_1^{MnR}(t_K;\lambda_R^M) \\ \vdots & \cdots & \vdots & & \vdots & & \cdots & & \vdots & \\ \vdots & \cdots & \vdots & & \vdots & & \cdots & & \vdots & \\ w_I^{1n}(t_K) & \cdots & w_I^{Mn}(t_K) & \Gamma_I^{1n1}(t_K;\lambda_1^1) & \cdots & \Gamma_I^{1nR}(t_K;\lambda_R^1) & \cdots & \Gamma_I^{Mn1}(t_K;\lambda_1^M) & \cdots & \Gamma_I^{MnR}(t_K;\lambda_R^M) \end{bmatrix}, \tag{74}$$

$$\lambda=\begin{bmatrix} \lambda_1^1 & \cdots & \lambda_R^1,\ldots,\lambda_1^M & \cdots & \lambda_R^M \end{bmatrix}^T, \tag{75}$$

$$\mu=[f_v^1,\ldots,f_v^M,(1-f_v^1)\gamma_1^1,\ldots,(1-f_v^1)\gamma_R^1,\ldots,(1-f_v^M)\gamma_1^M,\ldots,(1-f_v^M)\gamma_R^M]^T. \tag{76}$$

This gives the following expression

$$[R_1(\lambda)\mu,\ldots,R_N(\lambda)\mu]\beta=p. \tag{77}$$

or

$$R(\lambda,\mu)\beta=p, \tag{78}$$

where

$$R(\lambda,\mu)=[R_1\mu,\ldots,R_N\mu], \tag{79}$$

$$\beta=[a_1^B,\ldots,a_N^B]^T. \tag{80}$$

This is the most general formulation for fitting a multi-compartment model for each voxel to projection measurements.

The parameters λ, μ and β are solved by least-squares minimization. Constraints imposed are $\lambda_r^m \geq 0$ and $f_v^m \geq 0$. The spectral components for every pixel in the image are determined directly from the projections by non-negative least squares technique. Computationally, this can be a large problem. It can be broken up by first determining spectral components for each projection sample (Meikle *et al* 1996, 1998). The spectral components for each pixel can then be reconstructed from the spectral components of the ray sums. Alternatively, a reduced-basis set can be formed and the Moore-Penrose pseudoinverse can be used to find the coefficients of the basis (Maltz 2000a).

4.5. Summary

In Zeng *et al* (1995), the parameters of a one-compartment model were fitted directly from the projection measurements. It was shown that biases in parameters estimated from the time–activity curves generated from the reconstructions were eliminated by estimating the parameters directly from the projections. The estimation from projections was performed by (1) first estimating the multiplicative factors using a linear estimation technique and (2) then estimating the exponential factors by reducing the nonlinear estimation problem to a linear estimation problem by using linear time-invariant system theory. The estimation was performed on the sum of the counts in a projection.

Later, the problem was formulated as a minimization of a weighted sum of squared differences between the projection data and the model predicted values (Huesman *et al* 1998). A one-compartment model was assumed for the simulated myocardium tissue, and the blood input function was assumed to be known. Simulated data were used to show that unbiased kinetic parameter estimates for one-compartment models could be obtained directly from parallel-beam and cone-beam SPECT projections with proper segmentation of volumes encompassing the projected field-of-view. These simulations systematically incorporated physical effects, such as attenuation, and led to the development of methods that were used to analyze a dynamic ^{99m}Tc-teboroxime patient study (Reutter *et al* 1998b). For this patient study, the blood input function was estimated directly from the projections, and spatial models for the left ventricular myocardium blood pool, liver and background tissue were determined (as shown in figure 11) by automatically segmenting a dynamic volumetric image sequence reconstructed from the projection data.

Later on, a 4D maximum *a posteriori* (MAP) approach with a compartmental-model-based temporal prior that constrains each voxel's behavior in time to conform to a compartmental model was developed for dynamic cardiac SPECT application (Kadrmas and Gullberg 2001). No *a priori* limitations on kinetic parameters were applied, but the parameter estimates evolved as the algorithm iterated to a solution. The estimated parameters and time–activity curves were used within the reconstruction algorithm to model changes in the activity distribution as the camera rotates, avoiding artifacts that could result from inconsistencies of data between projection views. The ordered-subsets maximum *a posteriori* (OSMAP) algorithm resulted in images with better myocardial uniformity and definition, yielded time–activity curves with reduced noise variations, and provided wash-in parameter estimates with better accuracy and lower statistical uncertainty than those obtained from conventional ordered-subsets expectation-maximization (OS-EM) processing followed by compartment modeling. The algorithm removed the bias in K_1 estimates that can be caused by inconsistent projections from sampling schedules as slow as 60 s per time frame. However, no improvement in wash-out parameter estimates was observed. Incorporation of the compartmental relationship between blood and tissue activities into the spatiotemporal model provides a temporal regularization. Such an approach is desirable for

cameras with slow rotation protocols that result in poor temporal sampling and aggravate the problems of data inconsistency. The temporal prior encourages the time behavior of the image values to match a compartmental model. It also provides a means for modeling how the distribution of the tracer changes as the camera rotates during the acquisition, thereby addressing the problem of inconsistent projections. The framework is also well suited for accepting spatially regularizing priors, and such priors could readily be applied to either reconstructed voxel intensities or kinetic parameter estimates, as desired.

The 4D maximum *a posteriori* approach in section 4.3 assumes the time–activity curve for each voxel is constrained by a one-compartment model. A generalization to multiple compartments is presented in section 4.4, where it is assumed that the kinetics in each voxel can be represented by a spectral decomposition of exponential terms. The solution can be determined by least squares or by maximum *a posteriori* algorithms. However, the computational effort increases significantly the more general the model.

In summary, the combination of camera gantry motion and the time-varying nature of the radionuclide distribution being imaged results in inconsistent projection data sets. The estimation of kinetic parameters from reconstructed time–activity curves results in biases. Estimating the kinetic parameters directly from projections reduces these biases.

5. Estimation of kinetic model parameters from projections—semi-direct methods

While the estimation of kinetic model parameters directly from projections can potentially provide better variance and bias, it is more computationally demanding. Direct methods involve solving a nonlinear estimation problem (Zeng *et al* 1995, Huesman *et al* 1998), and the computational resources required for the straightforward solution of the embedded linear least-squares subproblem grow linearly with the number of SPECT projection measurements. These are nontrivial for typical patient datasets. To make matters worse, the computational requirements for the straightforward solution increase quadratically with the number of linear parameters. A more computationally efficient solution is to use semi-direct methods in which spatiotemporal modeling of the kinetics of the radiopharmaceutical tracer is implemented.

Semi-direct methods reduce the number of parameters and involve the process of solving a linear problem before solving a nonlinear problem to determine the kinetic model parameters. Semi-direct methods first estimate time–activity curves,

$$A(x,t)=\sum_{m,n} a_{mn} S^m(x) V^{mn}(t), \tag{7}$$

from projections

$$P(d(t),t)=\sum_{m,n} a_{mn} U^m(d(t),t) V^{mn}(t). \tag{9}$$

Then, the estimation of compartment model parameters is performed subsequent to direct estimation of time–activity curves.

The following gives various examples of the formation of spatiotemporal basis functions. First, splines are presented. These are used in many scientific applications to fit a continuous

smooth function to discrete data. The estimation of spline coefficients is computationally efficient; splines are free form and have finite support. Second, factors which are physiological time–activity curves that are inherent in the data are presented. Then, time–activity curves that rise to a maximum and then decrease monotonically (dSPECT method) are presented.

5.1. Spline spatiotemporal basis functions

For the activity $A(x, t)$ represented using splines as basis functions,

$$A(x,t)=\sum_{m,n} a_{mn} S^m(x) V^n(t), \tag{16}$$

the projection equations can be expressed as

$$P(d(t),t)=\int_{\chi} F[x,d(t)] \sum_{m,n} a_{mn} S^m(x) V^n(t)\,\mathrm{d}x \tag{81}$$

$$=\sum_{m,n} a_{mn} U^m(d(t),t) V^n(t), \tag{82}$$

where

$$U^m(d(t),t)=\int_{\chi} F[x,d(t)] S^m(x)\,\mathrm{d}x. \tag{10}$$

Integrating over the time interval Δt_k yields

$$p_i(t_k)=\int_{t_k-\Delta t_k}^{t_k} P(d_i(t),t)\,\mathrm{d}t \tag{11}$$

$$p_i(t_k)=\int_{t_k-\Delta t_k}^{t_k} \int_{\chi} F[x,d_i(t)] A(x,t)\,\mathrm{d}x\,\mathrm{d}t \tag{12}$$

$$\begin{aligned} p_i(t_k)&=\int_{t_k-\Delta t_k}^{t_k} \sum_{m=1}^{M}\sum_{n=1}^{N} a_{mn} U^m(d_i(t),t) V^n(t)\,\mathrm{d}t, \\ f_{ik(mn)}&=\int_{t_k-\Delta t_k}^{t_k} U^m(d_i(t),t) V^n(t)\,\mathrm{d}t, \end{aligned} \tag{83}$$

$$p_i(t_k)=\sum_{m=1}^{M}\sum_{n=1}^{N} a_{mn} f_{ik(mn)}, \tag{84}$$

where $p_i(t_k)$ are the modeled projections, a_{mn} are the linear coefficients associated with the time integrals of the projections of the spatiotemporal basis functions, M is the number of spatial basis functions and N is the number of temporal basis functions. The criterion that is minimized by varying the linear coefficients a_{mn} associated with the time integrals of the projections of the spatiotemporal basis functions is the weighted sum of squares function,

$$\chi^2(a_{mn})=\sum_{k=1}^{K}\sum_{i=1}^{I}\frac{(\tilde{p}_i(t_k)-p_i(t_k))^2}{1/W_{ik}}, \tag{85}$$

where $\tilde{p}_i(t_k)$ are the measured projections, W_{ik} are the weighting factors usually taken to be the reciprocal of the measurement errors, I is the number of projection rays per angle and K is the number of projection samples in time.

Equation (84) can be rewritten in the matrix form as

$$p=Fa, \tag{13}$$

and equation (85) in the form

$$\chi^2=(\tilde{p}-Fa)^T W(\tilde{p}-Fa), \tag{86}$$

respectively, where $\tilde{p}$ is an IK element column vector whose [i + (k − 1) I]th element is $p_i(t_k)$, F is an $I\,K \times MN$ matrix whose {[i + (k − 1) I], [m + (n − 1) M]}th element is $f_{ik(mn)}$, a is an MN element column vector whose [m + (n − 1) M]th element is a_{mn}, $\tilde{p}$ is an IK element column vector whose [i + (k − 1) I]th element is $\tilde{p}_i(t_k)$ and W is an $I\,K \times I\,K$ diagonal matrix whose [i + (k − 1) I]th diagonal element is $1/W_{ik}$. The criterion χ^2 is minimized by the vector of spatiotemporal basis function coefficients,

$$\widehat{a}=(F^T WF)^{-1}F^T W\widehat{p}. \tag{87}$$

The covariance matrix for the coefficients $\hat{a}$ is

$$\mathrm{cov}(\widehat{a})=(F^T WF)^{-1}F^T W\mathrm{cov}(\tilde{p})WF(F^T WF)^{-1}, \tag{88}$$

where cov($\tilde{p}$) is the covariance matrix for the measured projections. Given an estimate of cov($\tilde{p}$), estimates of the statistical uncertainties of the coefficients $\hat{a}$ are the square roots of the diagonal elements of the covariance matrix given by Kimura *et al* (1990). In general, the errors in the coefficients are correlated and the covariance matrix given by Kimura *et al* (1990) has nonzero elements off the diagonal. If $W = \mathrm{cov}(\tilde{p})^{-1}$,

$$\mathrm{cov}(\widehat{a})=(F^T WF)^{-1}. \tag{89}$$

A preliminary study reported on the biases that result from modeling various orders of temporal continuity and using various time samplings when estimating time–activity curves directly from dynamic cone-beam and parallel-beam SPECT projection data (Reutter *et al* 2000). Piecewise cubic, quadratic, linear and constant B-splines were used to model the time–activity curves for the blood input, three myocardial volumes of interest, liver and background tissue in simulated data. Segmented volumes encompassing the projected field-of-view were modeled to contain spatially uniform activity concentrations. The effects of spatial segmentation errors were also studied.

5.1.1. Comparison of conventional, semi-direct and direct methods using computer simulations—Computer simulations were performed to compare a semi-direct

method using splines with a direct method of estimating kinetic model parameters from projections and with a conventional method of obtaining time–activity curves from a sequence of dynamic reconstructions for a particular ROI. A dynamic version of the MCAT phantom (Tsui *et al* 1993, Pretorius *et al* 1999) in figures 12(a) and (b) was created for the simulations. A single 2D slice of the phantom was used for the experiment. The dynamic phantom was constructed by summing each organ of the static phantom using weights derived from the time–activity curves shown in figure 12(c) for each time frame. In this way, a series of 2D phantoms were constructed, one for each time frame of the dynamic acquisition. The time–activity curves shown in figure 12(c) were generated to mimic those seen in patient studies. The myocardium time–activity curve was constructed using blood as the input function while assuming a one-compartment model (figure 8) with wash-in and wash-out rate constants and a blood fraction given in table 1. Each time–activity curve was numerically integrated over the active acquisition time for each time frame. Projection data were formed by projecting each time frame of the 64 × 64 dynamic phantom. A 15 min data acquisition was simulated consisting of 15 revolutions of a single-head SPECT system, acquiring 120 angles per revolution and 64 parallel projection samples per angle. The simulated projections included the effects of attenuation and geometric point response, but neither scatter nor noise. Dynamic sequences of 120 projections (complete revolution) every 60 s were reconstructed using a conjugate gradient algorithm to minimize an unweighted least-squares criterion. Time–activity curves were generated from the reconstructed dynamic sequence (conventional method). These data were submitted to RFIT (Huesman *et al* 1995) to obtain the unweighted least-squares fit for the kinetic parameters. The regions selected for the fit to the compartment model are shown in figure 12(a). From the known regions of the intraventricular blood, myocardium and background, equations for the projections were formulated using the reconstructed attenuation distribution to obtain expressions for the attenuated projections. Using the system of projection equations for all regions, the kinetic parameters for each region were simultaneously estimated directly from the projections (direct method) (Reutter *et al* 1998a). Next, B-splines for time–activity curves were estimated directly from projections using the same projection model (Reutter *et al* 2000), and for these curves kinetic parameters were then estimated using RFIT (Huesman *et al* 1995) (semi-direct method). In each of the methods, the blood input function was assumed to be known.

One can see in table 1 that the direct approach gives the best results, even though they are only slightly better than those of the semi-direct method but significantly better than those of the conventional method. The conventional method did poorly in the defect and did reasonably well in the normal myocardium. The bias is primarily due to artifacts resulting from inconsistent projection data and partial volume effects in the sampled ROI of the reconstructed defect. Noise was purposely not included in the simulations. It was assumed that the measured projections corresponded to the true mean and variance of a Poisson random process. If noise had been added, assuming a Poisson distribution with mean and variance equal to the random variable of the sampled projection, the results of an estimated weighted least-squares reconstruction would have been biased.

5.1.2. Comparison of semi-direct and direct methods using data acquired from a patient study—Data from a patient study were used to compare the estimation of kinetic model parameters using semi-direct and direct methods for the estimation of kinetic model parameters from projection measurements (Reutter *et al* 1998a, 1998b). Patient data were acquired on a PRISM 3000XP SPECT system at the University of Utah using a fast data acquisition protocol. First, a transmission scan was performed using a ^{153}Gd line source as the transmission source. The patient was stressed using adenosine. A dynamic acquisition obtaining 120 projections over 360° every 10 s was initiated at the same time as the injection of 925 MBq (25 mCi) of ^{99m}Tc-teboroxime. The attenuation map was reconstructed using

20 iterations of the transmission ML-EM algorithm (Lange and Carson 1984). The attenuation-corrected emission results were reconstructed using 20 iterations of the ML-EM algorithm. A 4D second directional derivative operator was applied to the attenuation-corrected dynamic image data set containing ninety 10 s frames to segment the regions of the myocardial tissue, intraventricular blood, liver and background tissue. Figure 13 shows the myocardial, liver and body surfaces extracted automatically at time frame 31 (corresponding to the interval 300–310 s).

The spatial activity concentration within these volumes was modeled by indicator functions. From the segmented results, equations for the projections were formulated using the reconstructed attenuation distribution to obtain expressions for the attenuated projections. Using these equations, the kinetic parameters for the patient study were estimated directly from the projections (direct) (Reutter *et al* 1998a). B-splines of time–activity curves were estimated directly from projections using the same model for the projection measurements (Reutter *et al* 2000, 2002, 2004a). Compartment model parameters were then estimated using RFIT (Huesman *et al* 1995) for these fitted time–activity curves (semi-direct). The results are in table 2. Here it is difficult to make a statement as to which is better.

5.1.3. Dynamic SPECT image reconstruction of projections acquired with slow rotation using multi-resolution spatiotemporal B-spline image representation —In the previous example, the data were acquired with a relatively fast camera rotation. This study was performed to see how well time–activity curves could be estimated from projections acquired with a relatively slow camera rotation (Gullberg *et al* 2007a, Reutter *et al* 2007a). Projection data were acquired in 1 s time frames with an angular step of 5° per frame on a GE Millennium VH Hawkeye SPECT-CT scanner at UCSF. The acquisition was started immediately at the time of the injection of 740 MBq (20 mCi) of ^{99m}Tc-sestamibi. Attenuation and depth-dependent collimator response were modeled, but not scatter. The 4D B-splines were piecewise trilinear in space and piecewise quadratic in time. The splines were organized on a 3D spatial grid that provided uniform sampling of 17.7 mm in each dimension, and on a 1D temporal grid that provided nonuniform sampling intervals of 0–4, 4–15, 15–48 and 48–144 s during the first two gantry rotations. The 4D spatiotemporal distribution was reconstructed via direct matrix inversion to minimize a penalized least-squares criterion. Figure 14 shows results of the blood in the right ventricle at 15 s (figure 14(a)), in the left ventricle at 45 s (figure 14(b)), and the summed image (figure 14(c)) for one transaxial slice. The use of nonuniform time sampling with piecewise-quadratic splines yielded smooth time–activity curves that captured the relatively fast rise and fall of tracer in the right and left intraventricular blood chambers, as well as uptake and retention of tracer in the left ventricular myocardium (figure 14(d)).

5.1.4. Estimation of kinetic parameters directly from projections provides more efficient estimators—Computer simulations of a human dynamic ^{99m}Tc-teboroxime cardiac SPECT study using the MCAT phantom (figure 12) showed that the additional temporal regularization provided by jointly estimating compartmental model and blood input function parameters directly from projections resulted in improved precision of parameter estimates, as well as comparable or improved accuracy (Reutter *et al* 2005). Four hundred realizations of cone-beam SPECT projection data having Poisson noise were generated. The simulation consisted of a 15 min dynamic cardiac data acquisition by a single-headed SPECT detector system with cone-beam collimator (70 cm focal length) providing 120 angles per revolution and 15 revolutions. The projection data were generated from a mathematical phantom that was composed of 128 contiguous 1.75 mm thick slices and contained $M = 6$ volumes of interest of uniform activity: the blood pool, three myocardial tissue volumes (normal myocardium, septal defect, lateral defect), liver and background tissue. Attenuation and geometric point response were modeled but scatter was

not modeled. The simulated time–activity curves shown in figure 12(c) mimicked the kinetics of ^{99m}Tc-teboroxime (Narra *et al* 1992).

Initially, time–activity curve models for all six volumes were estimated directly from noisy projection data with use of 16 B-spline basis functions spanning 15 time segments having geometrically increasing length. Piecewise quadratic B-splines were used with an initial time segment length of 10 s. For noiseless projections, the modeling error was less than 2%, where the error was defined to be the root mean square (RMS) difference between the simulated curve and the spline model, normalized by the RMS value of the simulated curve (Reutter *et al* 2000). Compartmental models were then fitted to the curves for the three myocardial tissue volumes and the liver. These semi-direct compartmental model fits were used as starting points for direct joint estimation of refined compartmental models and B-spline time–activity curves for the blood pool and background tissue. The results in table 3 show that using B-splines to model the input function and directly estimating compartmental model parameters and blood input function can improve quantitation of dynamic SPECT by reducing the standard deviation of uptake and wash-out parameters for the septal and lateral defects by 17% to 41%, compared to semi-direct methods that estimate time–activity curves first and then fit compartmental models to the curves. Of course, the accuracy of the model depends upon appropriately modeling the effects of the physics (attenuation, scatter, geometric response) of the imaging detection process and defining the appropriate compartment model for each tissue type. This also has important implications for the estimation of kinetic parameters using dynamic PET.

5.2. Factor basis functions—factor analysis of dynamic structures (FADS)

Factor basis functions are estimated automatically from the data. They correspond to curves which are derived from the data that exhibit a direct physiological interpretation. In the factor model, each image is built from groups of voxels that have similar temporal behavior (Chua *et al* 1993). These groups may or may not overlap. Identification of these groups (voxels highly correlated in space and time) provides a segmentation of the imaged distribution into organs that have similar physiological behavior. This differs significantly from that of the dSPECT method discussed in the next section where there is no assumed temporal correlation between voxels, but only a spatial correlation imposed by tomography (i.e. each voxel has a separate independent time–activity curve).

One of the limitations of this approach is that the number of factors (number of groups with similar time behaviors) needs to be specified *a priori*. By limiting the number of these factors (usually not more than four are used), an approximation is used that all voxels are a linear combination of a limited number of temporal basis functions. Increasing the number of factors is difficult and probably not feasible, largely due to effects of non-uniqueness (Sitek *et al* 2000, 2002b), which are very hard to address. This is especially true when estimating factors from projections where it is difficult to spatially restrict the region that is analyzed because the entire volume is seen on projections and thus the number of factors may have to be limited more than the number used for FADS analysis of reconstructed images.

For the factor model in equation (21), the number of unknowns is equal to $N(K + M)$, which is substantially lower than the NMK unknowns for the complete inverse problem (K is the number of time points (projections), M is the number of spatial basis functions and N is the number of factors or temporal basis functions). For renal studies (Sitek *et al* 2001), N was chosen to be equal to 2 or 3. Although the number of unknowns is reduced by introducing the factor model, we will see that the objective function becomes nonlinear.

The counts in the projection bin i taken at the time t_k, $p_i(t_k)$ are expressed by the following projection equations,

$$P(d(t),t)=\int_{\chi}F[x,d(t)]\sum_{m,n,k'}a_{mn}S^m(x)F_{nk'}\chi_{k'}(t)\,\mathrm{d}x = \sum_{m,n,k'}a_{mn}U^m(d(t),t)F_{nk'}\chi_{k'}(t), \tag{90}$$

where

$$U^m(d(t),t)=\int_{\chi}F[x,d(t)]S^m(x)\,\mathrm{d}x \tag{10}$$

$$p_i(t_k)=\int_{t_k-\Delta t_k}^{t_k}P(d_i(t),t)\,\mathrm{d}t \tag{11}$$

$$p_i(t_k)=\int_{t_k-\Delta t_k}^{t_k}\int_{\chi}F[x,d_i(t)]A(x,t)\,\mathrm{d}x\,\mathrm{d}t \tag{12}$$

$$p_i(t_k)=\int_{t_i-\Delta t_k}^{t_k}\sum_{m=1}^{M}\sum_{n=1}^{N}\sum_{k'=1}^{K}a_{mn}U^m(d_i(t),t)F_{nk'}\chi_{k'}(t)\,\mathrm{d}t, \tag{91}$$

$$f_{ik(mk')}\delta_k^{k'}=\int_{t_k-\Delta t_k}^{t_k}U^m(d_i(t),t)\chi_{k'}(t)\,\mathrm{d}t, \tag{92}$$

$$p_i(t_k)=\sum_{m=1}^{M}\sum_{n=1}^{N}a_{mn}F_{nk}f_{ik(mk)}. \tag{93}$$

Estimates for a and F can be determined by constructing and minimizing the weighted least-squares objective function,

$$\chi^2(a,F)=\sum_{i,k}^{I,k}\frac{(p_i(t_k)-\tilde{p}_i(t_k))^2}{1/W_{ik}} \tag{94}$$

$$\chi^2(a,F)=\sum_{i,k=1}^{I,K}\frac{\left(\sum_{m,n=1}^{M,N}f_{ik(mk)}\cdot a_{mn}\cdot F_{nk}-\tilde{p}_i(t_k)\right)^2}{1/W_{ik}}. \tag{95}$$

The value of $\tilde{p_i}(t_k)$ is the experimental value of counts in the ith projection bin collected at the projection taken at time t_k. I is the number of bins in each projection and K is the number of projections or the total number of time samples. The value of $f_{ik(mk)}$ is an element of the system matrix. The element $f_{ik(mk)}$ is proportional to the probability that the photon emitted from the support of the basis function $S^m(x)$ pixel i at time t_k is detected in bin i of the projection taken at time t_k. N is the number of factors and M is the number of basis functions representing the spatial distribution of the image. The elements W_{ik} are elements of the weighting matrix W.

To ensure the non-negativity of the resulting matrix a and F, non-negativity constraints are imposed by adding the term $f_{\text{neg}}(a, F)$ to the objective function,

$$f_{\text{neg}}(a, F) = \sum_{m,n=1}^{M,N} H(a_{mn}) + \sum_{n,k=1}^{N,K} H(F_{nk}), \tag{96}$$

where

$$H(x) = \begin{cases} \alpha x^2 & x<0 \\ 0 & x \geq 0, \end{cases} \tag{97}$$

with α being a penalty constant.

In the above formulation, the non-uniqueness of the factor model (Sitek *et al* 2002b) was not addressed. Even without this, the estimation of factors from projection measurements was proven to be successful in renal studies (Sitek *et al* 2001). This approach also shows promise for analyzing dynamic cardiac studies in rodents using pinhole collimators mounted on patient SPECT systems with slow rotation (Hu *et al* 2005, 2008) (see next section).

5.2.1. Direct estimation of factors from projection measurements in small animal studies—One of the greatest difficulties in applying kinetic modeling in small animal studies is measuring the blood input function. The blood volume is small and thus it is difficult to draw blood samples, and the resolution of the ventricular cavity is inadequate for ROI sampling. The following demonstrates that, if factors and factor coefficients are estimated directly from projections, a blood input function can be obtained even with a slowly rotating camera. A dual-headed pinhole SPECT-CT system at LBNL (figure 15(a)) was used for imaging the distribution and kinetics of ^{123}I-MIBG in the myocardium of spontaneously hypertensive rats (SHR) and control Wistar Kyoto (WKY) rats to study the function of the sympathetic nervous system in heart failure (Hu *et al* 2005, 2008). A dynamic acquisition was performed by injecting 185 MBq (5 mCi) of ^{123}I-MIBG into rats immediately after initiating data acquisition. The detectors rotated, continuously traversing 360° every 90 s for a total acquisition time of 90 min. For the first 90 s rotation of the study, factor analysis estimates of the time–activity curves for the blood pool were obtained directly from the projections. This required the estimation of 1 024 180 unknowns. After the first rotation, the blood input was measured every 90 s from the ROI in the left ventricular blood volume of a contiguous sequence of dynamic tomographic reconstructions. The time resolution was equal to 1 s for the first 90 s and equal to 90 s for the remainder of the 90 min acquisition. By merging the blood input obtained over the first rotation with estimates of blood and tissue curves estimated from the subsequent sequence of dynamic reconstructions, compartmental model parameters were estimated. Figure 15 illustrates the resulting input function for four rats calculated using factor analysis with two factors. For these particular studies, there was no validation with blood samples. This is a semi-direct method in which time–activity curves were first estimated for the blood and the myocardial tissue. Kinetic parameters shown in table 4 were subsequently estimated by fitting the estimated time–activity curves to a one-compartment model.

5.3. dSPECT

The ‘dSPECT method’ fits time–activity curves for each voxel directly from projection measurements. These may only be acquired over a single rotation (Farncombe *et al* 1999, 2000, 2001, Farncombe 2000, Celler *et al* 2001). The method does not involve any

assumptions about the location of the dynamic regions. However, for the case of bimodal time–activity curves that increase and then decrease, it requires prior knowledge of the time frame in which the activity peaks in each particular image voxel (Farncombe *et al* 2001). Otherwise, as we explain below, the peak is estimated as part of the optimization problem. This is one approach of constraining the time–activity curves.

For the projections

$$\begin{aligned} P(d(t),t) &= \int_{\chi} F(x,d(t)) \sum_{m,n} a_{mn}\chi_m(x)\chi_n(t)\,\mathrm{d}x \\ &= \sum_{m,n} a_{mn}\left[\int_{\chi} F(x,d(t))\chi_m(x)\,\mathrm{d}x\right]\chi_n(t) \\ p(t_k) &= \sum_{m,n} a_{mn}\int_{t_k-\Delta t_k}^{t_k}\int_{\chi} F(x,d(t))\chi_m(x)\chi_n(t)\,\mathrm{d}x\,\mathrm{d}t, \end{aligned}$$

the dSPECT method is formulated as the solution to the following optimization problem,

$$\mathrm{Min}\,\chi^2(a_{mn}) = \sum_{i,k} W_{ik}[\tilde{p}_i(t_k) - p_i(t_k)]^2 \tag{98}$$

subject to

$$a_{m1} \le \ldots \le a_{mp} \ge \ldots \ge a_{mK}\,\forall m. \tag{99}$$

In different applications of the dSPECT method, the constraints have been formulated in other ways. In the expression given in equation (99), the reconstructed (optimum) time–activity curve monotonically increases to a maximum at time t_p and then monotonically decreases (Farncombe *et al* 2001). In some cases, the time–activity curve only decreases or increases monotonically (Celler *et al* 2001).

5.4. Other methods

Most of the methods implemented for calculating kinetic parameters from dynamic data are based on fitting a compartment model to the change in the tracer concentration in tissue regions over time. Most of these methods demand dynamic data acquisition following the tracer administration and then either a nonlinear or linear least-squares fitting to estimate the kinetic parameters. Other methods have been proposed where a weighted-integration technique is used instead to minimize the data processing time in generating functional maps of cerebral blood flow and distribution volume for ^{15}O water administration studies (Alpert *et al* 1984, Carson *et al* 1986). In this technique, the dynamic images are integrated after multiplication by two time-dependent weight functions, and two functional parameters are calculated by means of a table look-up procedure for each image pixel. For example, once the value of k_2 is determined, then the value of K_1 can be determined from linear equations. This eliminates the need to collect and store dynamic data. The kinetic parameters are calculated from the weighted integrals of the projection data, which are adequate for measuring the time-varying activity changes during the projection sampling, provided that the integrals are calculated with sufficient numerical accuracy.

This technique was extended to calculate up to six independent weighted-integrated sinograms (Iida *et al* 1995a). Values from the weight-integrated sinograms are inserted into operation equations to generate functional parameter images for $H_2{}^{15}O$ and ^{18}FDG. The two-compartment model of ^{18}FDG uses three independent time-weighted integrated images

that are inserted into the operation equations. The solution requires integration of the acquired counts over time. The time points for the acquired samples need not be at the same time for each projection, which accommodates the rotation of the camera head. The use of weighted integration to solve kinetic equations is suitable for certain models.

Application of weighted integration has been explored in dynamic SPECT (Tan *et al* 1994). The advantage of the weighted-integration approach is that it provides a straightforward solution calculated directly from projections that, assuming adequate numerical integration, are independent of the sampling limitations.

6. Discussion and future developments

This review has focused on special data processing techniques of dynamic SPECT highlighting cardiac perfusion imaging. The mathematical methods presented here are applicable to other dynamic imaging applications as well. Research continues in the development of hardware, radiopharmaceuticals and data processing techniques which will enable the realization of the full potential of dynamic SPECT.

6.1. Estimation from projections may produce less bias and variance and has potential even for PET

The estimation of kinetic parameters from projections may produce less bias and less variance than the conventional method of estimating kinetic parameters from time–activity curves generated from reconstructed ROIs. This review presents some examples demonstrating this fact. However, more work is needed to verify these results. Simulations have demonstrated that the simultaneous estimation of the input function and parameters of compartment models for tissue regions reduces variance and bias. A comparison of direct with indirect methods must be done carefully in order to be sure that weighting of the reconstructed data is done reasonably. However, this can be difficult because covariance matrices of reconstructed images or time–activity curves can be difficult to obtain and this requires a solution to an estimation problem with a large number of parameters. Models for dynamic imaging should be constructed so that the parameters are fitted directly to the original acquired data, not as a conventional two- or three-step process that first requires reconstruction followed by time–activity curve generation and then model parameter estimation. This should be accomplished for both consistent and inconsistent tomographic data. The modeling of the time variation in the projection data attempts to remove the inconsistency in the data of the inverse problem. It is also much easier to directly incorporate weighting by the noise in the data in the estimation process. Moreover, it has been demonstrated from simulations that direct estimation of model parameters produces less variance and less bias than the conventional method mentioned above, and also less than the two-step semi-direct methods in which the time–activity curves are estimated directly from projections and then kinetic parameters are estimated from those time–activity curves. This suggests that all kinetic parameters should be estimated directly from dynamic data. It is anticipated that all the completely consistent tomographic data acquired with a stationary SPECT detector system or a PET scanner will produce less bias and less variance than is produced with a rotating SPECT camera.

6.2. Optimum spatiotemporal basis functions

For the models that represent the tracer activity variation directly using the projection data for non-deforming media, the challenge is to determine optimal spatiotemporal basis functions. Splines have been demonstrated to efficiently represent both spatial and temporal variations in the data (Reutter *et al* 2000, 2002, 2004a, 2007a). There are various orders of splines that can be used depending upon the frequency content of the data. Multigridding (a

higher resolution representation used when necessary, and less so otherwise) is required to reduce the number of unknowns so that the system of acquired projection data is not underdetermined. This is especially important when developing models for slow camera rotation. Spherical harmonics could also be used for spatial basis functions. It has also been demonstrated that factors can provide excellent temporal basis functions. However, the solution can require a large number of unknowns, and non-uniqueness is a problem that must be considered (Hu *et al* 2005, 2008). Still another approach is to use a spectral method for the temporal representation based upon exponential functions as a basis which requires linear estimation of the parameters (Maltz 2000b, 2001, 2002).

6.3. Tomographic reconstruction of tracer kinetics in the heart using a spatiotemporal mechanical model

In organs such as the heart, which deform while the intensity of the signal changes as a result of radiotracer redistribution, both space and time need a parameterization that deforms with the organ. It is necessary to consider these changes as data are taken in order to reduce the bias and variance of model parameters. A generalized model for specifying time changes of tracer activity and mechanics on a deforming differential manifold has been developed (Gullberg *et al* 2007b). The proposed model is a large optimization problem that seeks to find a number of optimum parameters by focusing on organs, such as the heart, that have rapid simultaneously changing tracer concentrations and organ configurations. The spatial parameterization can be accomplished using smooth functions relative to the Euler frame that can easily be transformed to the differential manifold of the deforming heart. The temporal parameterization can be accomplished using appropriate parameterization of the spatial deformation as a function of time. The temporal basis functions could be splines (Reutter *et al* 2000), factors of dynamic structures (Sitek *et al* 2002b) or time–activity curves of a compartment model (Kadrmas and Gullberg 2001). The spatial parameterization can also involve a multi-resolution approach, where inside the organ boundaries the changing tracer kinetics are modeled with high resolution and outside the boundaries the distribution is modeled with a more coarse resolution (Boutchko *et al* 2006b, Reutter *et al* 2006, 2007b, Sitek *et al* 2006). This has been shown to actually reduce the number of parameters of the tomographic problem (Reutter *et al* 2004a). The accuracy of the model depends upon appropriately modeling the effects of the physics of the imaging detection process (attenuation, scatter, geometric response). The accuracy also depends on the use of appropriate models for the physiology of the tracer kinetics and for the mechanical properties of the heart.

The proposed method involves simultaneous segmentation and estimation of the dynamic parameters. It is assumed that the data are acquired dynamically with cardiac phase information, either by list mode acquisition or by framing into gated dynamic frames over the cardiac cycle. The differential manifold of the heart deforms according to a mechanical model (Sitek *et al* 2002c, Veress *et al* 2005, Sitek *et al* 2005) and incorporates methods (Feng *et al* 2003b, Shi and Karl 2003, 2004) for determining the boundary of the heart. It also includes a dynamically changing organ boundary and intensity represented by spatiotemporal basis functions within the boundary, defined by a deforming manifold. The organ boundaries are determined using level set methodology, which was devised as a simple method for computing and analyzing motion of a surface in two or three dimensions (Osher and Sethian 1988, Sethian 1996, Osher and Fedkiw 1999). The body within the surface is defined in an Euler reference frame using either Cartesian or curvilinear coordinates. The body within the surface is a differential manifold that is allowed to deform based on a mechanical model. Therefore, the surface is specified as the zero level set of a smooth function, where the spatial parameters are either Cartesian or curvilinear coordinates defined in the deformed space. This approach imposes constraints based upon a mechanical

model, and it simultaneously segments the boundary of the organ and estimates model parameters of changing activity.

6.4. Estimation of scatter from dynamic imaging data

Dynamic imaging may help in estimating the physical properties of the imaging detection process, such as scatter, by using the different kinetics of the tracer in different organs to model scatter. Most software-based methods need a transmission image (not an emission image) to simulate scatter (Welch *et al* 1995a, Zeng *et al* 1999, Bai *et al* 2000, Laurette *et al* 2000, Floyd *et al* 1985, Liang *et al* 1992, Frey and Tsui 1993, Meikle *et al* 1994, Beekman *et al* 1996, 2002, Kadrmas *et al* 1998). Methods have been developed to understand the nature of scatter (Reutter *et al* 2003), to segment scatter from primary photons using principal component analysis (Toennies *et al* 2003), to identify and remove scatter artifacts (Toennies *et al* 2004) and to model scatter based upon the temporal information in dynamic SPECT data (Toennies *et al* 2003, Reutter *et al* 2004b). Two methods (Reutter *et al* 2004b) have also been proposed for modeling and estimating scatter jointly with tracer kinetic models. These methods exploit the fact that the scatter distribution from a volume of interest is spatially smooth, and has the same temporal kinetics as unscattered events from the volume. The first method treated scattered events as if they originated from scatter sites distributed in image space. For each volume of interest, the distribution of scatter sites was modeled with a smooth spatial function, and events from this effective scatter source distribution (ESSD) (Frey and Tsui 1997, Kadrmas *et al* 1998) were forward-projected along with unscattered events from the volume. The second method bypasses modeling an ESSD in image space and simply models the spatial projection of scatter to be a smooth function in projection space. Computer simulations of a dynamic ^{99m}Tc-teboroxime cardiac SPECT scan showed that unscattered and scattered events from the blood pool, myocardium and liver have distinct spatiotemporal signatures and that it is feasible to jointly estimate scatter amplitudes and time–activity curves for volumes of interest directly from projection data. This suggested that joint estimation of scatter, blood input function and compartmental model parameters is a well-posed problem and can lead to reduced bias in kinetic parameter estimates.

6.5. Dynamic information in a well-isolated bolus during the input phase

In general, the dynamic temporal/spatial distribution of tracers is complex and varies between different organs of the body. However, at the beginning of a study, soon after administration of the pharmaceutical, the activity is confined to major vessels, including the vena cava, right ventricle, pulmonary artery and vein, left ventricle and aortic arch. This may simplify the modeling of the initial dynamic uptake considerably. For example, the regions of the heart may be treated as compartments during that period, as in the approach described in section 5.3.1 or in Sitek *et al* (2001) and Hu *et al* (2008). More complex approaches that model bolus propagation can also be employed in which the bolus is modeled as a delta function propagated over time and confined to these major vessels. This considerably reduces ambiguity caused by insufficient angular sampling in tomographic reconstruction of these studies.

Computer simulations (Herrero *et al* 1989) have demonstrated that the compartment modeling approach is more sensitive to timing discrepancies—especially discrepancies between the arterial input function and the tissue time–activity curve—than it is to most physical sources of error. Computer simulations have also been employed to investigate the necessary timing resolution and input function shape required to minimize bias and variance of estimated kinetic parameters (Ross *et al* 1997b).

6.6. Potential for improved temporal sampling resolution with new fast dedicated cardiac SPECT systems

While dedicated brain SPECT cameras have existed for some time, results with new dedicated cardiac SPECT systems are showing improved image quality, higher signal-to-noise ratios and improved energy resolution. The GE dedicated cardiac SPECT camera (Volokh *et al* 2008, Garcia *et al* 2008, Esteves *et al* 2008, Buechel *et al* 2010) uses a stationary detector that views the myocardium from multiple directions with multiple modular cameras, each collimated with a single pinhole (see figure 3(b)). The GE system has no moving parts but requires reconstruction of pinhole data, whereas the Spectrum Dynamics system (Sharir *et al* 2007, 2008, Berman 2007, Gambhir *et al* 2009, Erlandsson *et al* 2009) (see figure 4) has parallel geometry with individual collimator–detector modules rotating axially. The GE and Spectrum Dynamics designs offer significant advantages in comparison to conventional SPECT systems with parallel-hole collimators that capture the heart on only a small fraction of the available active detector area. These systems have the option to be placed in tandem with volumetric CT (VCT) scanners for attenuation correction and correlated diagnostic information. The GE and Spectrum Dynamics cameras use new CdZnTe (CZT) technology (Barber *et al* 1993, 1994, James *et al* 1995, Darambara and Todd-Pokropek 2002, Feichtinger *et al* 2004, Verger *et al* 2004, Brzymialkiewicz *et al* 2005, Luke and Amman 2007). This development has the potential to lessen scatter acceptance and improve contrast. Despite the advances in CZT fabrication technology, a CZT detector is still very expensive and the availability of large-volume and large-area (>2 cm^2) CZT detectors continues to be limited.

6.7. Need for developing methods to analyze dynamic data for molecular imaging applications

Small-animal imaging studies associated with molecular imaging are rapidly expanding (Weissleder and Mahmod 2001, Massoud and Gambhir 2003). Dynamic SPECT has been used to evaluate myocardial fatty acid metabolism in rodents with hypertrophic cardiomyopathy (Hirai *et al* 2001, Hu *et al* 2005, 2008). For reviews of small animal imaging of single photon tracers, see Weber and Ivanovic (1999), Budinger (2002), Peremans *et al* (2005) and Beekman and van der Have (2007). The development of models, algorithms and data processing methods will become increasingly important. It has been demonstrated that SPECT imaging of small animals can be performed on commercial clinical imaging systems with specially designed pinhole collimators (Hirai *et al* 2001, Metzler *et al* 2005, Zhou *et al* 2005, Acton *et al* 2006, Forrer *et al* 2006, Hu *et al* 2008). This differs from dedicated small animal SPECT/CT systems (Furenlid *et al* 2004, Zeniya *et al* 2006, Vastenhouw and Beekman 2007). Molecular imaging facilitates the study of mechanisms and treatment of human diseases in animal models and permits longitudinal investigations that track physiologic changes over time in the same animal. The evaluation of radiopharmaceuticals in small animals is a major step in the process of the translational development of clinical radiotracers and requires new techniques of data acquisition and new algorithms for processing imaging data.

6.8. Advancements in patient care

The role of SPECT in radionuclide procedures for diagnosis and therapeutic planning continues to grow. Clinically, dynamic SPECT has been used for brain applications with specialized, dedicated brain scanners. However, the application of SPECT to imaging dynamic processes in the heart has not been fully realized. Dynamic SPECT has the potential to improve diagnostic accuracy over conventional SPECT with little, if any, increased cost. Continuing developments of mathematical and clinical tools, coupled with the developments of new agents and cameras, will make dynamic cardiac SPECT imaging clinically viable.

Acknowledgments

We want to thank the reviewers for their very helpful comments and suggestions, which helped make this a much more readable review. We also thank Sean Webb for editing the manuscript. We also want to thank Kathleen Gullberg for her helpful comments and edits. This work was supported by the National Institute of Biomedical Imaging and Bioengineering and the National Heart, Lung, and Blood Institute of the National Institutes of Health under grants R01EB007219 and R01HL50663, and by the Director, Office of Science, Office of Biological and Environmental Research, Medical Sciences Division of the US Department of Energy under contract DE-AC02-05CH11231.

Glossary

^{18}F	Fluorine-18 is a radioisotope of fluorine that emits a positron with a half-life of 109 min and is tagged to pharmaceuticals for PET imaging
^{18}FDG	2-Fluoro-2-deoxy-d-glucose (FDG) is a glucose analog used for metabolic imaging of brain function, heart metabolism and tumor growth
^{18}F-DOPA	Fluorine-18-l-dihydroxyphenylalanine (^{18}F-DOPA) is a PET tracer that is important in the diagnosis of motor disorders
$H_2{}^{15}O$	Radioactive water is used to measure perfusion of the brain and heart
^{123}I	Iodine-123 is a radioisotope of iodine with a predominant gamma emission of 159 keV (half-life of 13.22 h) and is tagged to pharmaceuticals for SPECT imaging
^{123}I-ADAM	[^{123}I] [2-((2-((dimethylamino)methyl)phenyl)thio)-5-iodophenylamine (ADAM)] is a very promising imaging ligand for the detection of serotonin transporters (SERT) in human brain because of its high specificity for SERT
^{123}I-altropane	2Beta-carbomethoxy-3beta-(4-fluorophenyl)-*n*-(1-iodoprop-1-en-3-yl) nortropane (IACFT, Altropane) is a cocaine analog with high affinity and selectivity for dopamine transporter (DAT) sites in the striatum. Dopamine transporter density declines in Parkinson's disease
^{123}I-beta-CIT	[^{123}I]beta-CIT is a sensitive marker of dopaminergic degeneration, and the degree of striatal binding reduction in Parkinson's disease correlates with disease severity
^{123}I-BMIPP	^{123}I-β-methyl-*p*-iodophenyl-pentadecanoic acid (BMIPP) is a modified long-chain fatty acid used for imaging metabolism in the myocardium. A methyl group on the β position of the carbon chain limits the complete oxidation of ^{123}I-BMIPP
^{123}I-FP-CIT	^{123}I is labeled to *N-o*–fluoropropyl-2,f-carbomethoxy-3,B(4-iodophenyl) tropane to produce a radioligand with fast kinetics used for imaging of the dopamine transporter in brain disorders (such as Parkinson's disease) with SPECT
^{123}I-hippuran	I-131-sodium 2-[(2-iodobenzoyl)amino]acetate (hippuran) is a radioactive iodine compound used in diagnostic studies of renal function
^{123}I-MIBG	[^{123}I]metaiodobenzyl guanidine ([^{123}I]MIBG) enables the quantification of postganglionic sympathetic cardiac innervation

^{123}I-IMP	*N*-Isopropyl-4-[^{123}I]iodoamphetamine is a lipophilic compound utilized for CBF measurements with SPECT
^{123}I-iodorotenone	Novel radiolabeled rotenone analogs (labeled with tritium, carbon-11, fluorine-18 and iodine-123, -125) display efficient myocardial uptake and adequate myocardial retention for clinical evaluation of myocardial blood flow. Rotenone binds to complex I of the mitochondrial electron transport chain
^{123}I-Iomazenil	[^{123}I]Iomazenil ([^{123}I]IMZ) is a ligand displaying high affinity for central-type benzodiazepine receptors, with high brain uptake and little nonspecific binding
^{123}IPPA	Iodine-123-phenylpentadecanoic acid (^{123}IPPA) is a synthetic long-chain fatty acid used for imaging fatty acid metabolism in the myocardium
^{13}N	Nitrogen-13 is a radioisotope of nitrogen that emits a positron with a half-life of just under 10 min and is tagged to pharmaceuticals for PET imaging
$^{13}NH_3$	^{13}N-labeled ammonia is used to measure perfusion of organs such as the heart and brain
^{15}O	Oxygen-15 is a radioisotope of oxygen that emits a positron with a half-life of 2.25 min and is tagged to pharmaceuticals for PET imaging
^{99m}Tc	Technetium-99m is a metastable nuclear isomer of technetium-99 that decays to ^{99}Tc, emitting a gamma ray of 140 keV with a half-life of 6 h, and is tagged to pharmaceuticals for SPECT imaging
^{99m}Tc-ECD	Technetium-99m ethyl cysteinate dimer (^{99m}Tc ECD) is used to image regional cerebral blood flow in patients
^{99m}Tc-HMPAO	Technetium-99m-labeled hexamethylpropyleneamineoxime (^{99m}Tc-HMPAO) is a gamma-emitting radionuclide imaging agent useful in the evaluation of regional cerebral blood flow. It has also been used to label leukocytes in the investigation of inflammatory bowel diseases
^{99m}Tc-MAG3	^{99m}Tc-Mercaptoacetyltriglycine (^{99m}Tc-MAG3) is a technetium-labeled radiopharmaceutical used in diagnostic studies of renal function
^{99m}Tc-N-NOET	^{99m}Tc-*N*-Ethoxy-*N*-ethyl-dithiocarbamato-nitrido is a neutral lipophilic ^{99m}Tc-labeled myocardial perfusion agent with a high first-pass extraction fraction
^{99m}Tc-sestamibi (^{99m}Tc-MIBI)	^{99m}Tc-hexakis-2-methoxy isobutyl isonitrile (^{99m}Tc-MIBI) is a synthetic molecule of the isonitrile family that diffuses through cell membranes and may preferentially accumulate within mitochondria (complex I). ^{99m}Tc-sestamibi is used for cardiac and tumor imaging
^{99m}Tc-teboroxime	^{99m}Tc-tris(1,2-bis(dimethoxyphosphino)ethane) is used for myocardial perfusion studies
^{99m}Tc-tetrofosmin	^{99m}Tc-tetrofosmin is a cardiac imaging agent useful in the diagnosis and localization of regions of reversible myocardial ischemia. 2-[bis(2-ethoxyethyl)phosphanyl]ethyl-bis(2-ethoxyethyl)phosphane

	(tetrofosmin) forms a complex with ^{99m}Tc to obtain the imaging agent ^{99m}Tc-tetrofosmin
^{99m}Tc-TRODAT	This is a ^{99m}Tc-labeled tropane derivative that binds to a dopamine transporter with high selectivity. Its chemical composition is [2-[[2-[[[3-(4-chlorophenyl)-8-methyl-8-azabicyclo[3,2,1]oct-2-yl]methyl](2-mercaptoethyl)amino]ethyl]amino] ethanethiolato(3-)-*N*2,*N*2′,*S*2,*S*2′]oxo-[1*R*-(exo-exo)] (TRODAT-1)
^{201}Tl	Thallium-201 (half-life 73 h) is a radioisotope of thallium that decays by electron capture, emitting Hg x-rays (~70–80 keV) and photons of 135 and 167 keV in lesser abundance. Tl-20l is used to image the heart and behaves similarly to potassium in transport across cell membranes
^{133}Xe	Xenon-133 is a radioisotope of xenon with a gamma emission of 81 keV and a half-life of 5.2 days. It is used in the study of pulmonary function and blood flow in organs such as the brain
^{133}Xe-rCBF	Xenon regional cerebral blood flow (rCBF) is a method that uses the clearance of xenon-133 (^{133}Xe) to quantify rCBF data
Adenosine	A nucleoside composed of a molecule of adenine attached to a ribose sugar molecule. Adenosine is used as a vascular dilator in nuclear cardiac rest/stress studies. It is used to mimic vascular dilation experienced under cardiac stress
B-spline	A function that has minimal support with respect to a given degree, smoothness and domain partition
Blind estimation	The estimation of kinetic model parameters for an organ without knowledge of the input function by assuming that the input function is identical for all tissue regions
Blood compartment	The blood compartment contains plasma and blood cells. Throughout this review, it has been assumed that this is one compartment with rapid exchange between plasma and blood cells
Compartment	A compartment is a volume where the tracer is uniformly distributed. The compartment may be a physical space, such as an organ, or may represent a metabolic or bound state of the tracer
Compartment model	A compartment model is a mathematical description (usually represented by a system of differential equations) of the interrelationships for the rate of exchange of a tracer between various compartments. The amount of tracer leaving a compartment is usually assumed to be proportional to the total amount in the compartment and the rate constant is the fraction of that compartment that leaves per unit time
Coronary flow reserve	The ratio of coronary flow under maximal drug-induced coronary vasodilation to coronary flow under resting conditions
Detector	A detector in the context of this review paper is most often a gamma ray detector optimally designed for imaging 140 keV photons. The detector consists of a lead collimator, a NaI(Tl) scintillator, photomultiplier tubes, and electronics for forming a picture of the emitting photons from the patient

Diamox	Acetazolamide, sold under the trade name Diamox, is a carbonic anhydrase inhibitor that is used, among other things, to vasodilate the cerebral vascular system in order to evaluate brain blood circulation integrity
Direct method of estimating kinetic model parameters	The kinetic model parameters are estimated directly from the projection data using a model that relates the kinetic compartment model to the projection data
Distribution volume	See volume of distribution
Extraction fraction	The extraction fraction is the fraction of a tracer that is extracted as blood flows through a tissue. It is the arterial concentration minus the venous concentration divided by the arterial concentration
Extravascular compartment	The extravascular compartment contains intracellular and extracellular components (interstitial) that are physically outside vessels
Factor	See factor basis function
Factor analysis	See factor analysis of dynamic structures
Factor analysis of dynamic structures	This is a method of estimation of factors and factor coefficients from a dynamic sequence
Factor basis function	A factor basis function is a discrete temporal function describing the time course of activity concentration for a particular organ or tissue in the image. This time course has physiological interpretation so elements of the factor curves have to be non-negative
Factor coefficients	These are coefficients of the linear combination of factors in the factor model. These coefficients have physiological interpretation and must be non-negative
Factor model	In a factor model of the dynamic data it is assumed that the time course of each volume element (e.g. voxel) is a linear combination of usually not more than three or four factor basis functions
5D	Five-dimensional tomography accounts for the dimension of motion in addition to 3D space and time (e.g. lung and heart)
Flow extraction product (flow times extraction)	Flow extraction product is the wash-in rate constant K_1 in the one-compartment perfusion model. It corresponds to the flow times extraction of the tracer from the plasma
Hyperemia	Hyperemia is the increase in blood flow to body tissues in response to the presence of metabolites and oxygen demand
Interictal	Interictal is the period of time between epilepsy seizures
Ischemia	Ischemia is a restriction in blood supply with probable resultant damage or dysfunction of body tissues
Kinetic model parameters	Kinetic model parameters are the rate constants expressing the rate of exchange between compartments. For linear kinetics, the parameters

	are the linear coefficients in the system of differential equations that model the kinetics of the physiological process
Level set method	The level set method is a numerical technique for tracking interfaces and involves numerical computations of curves and surfaces on a fixed Cartesian grid without their having to be parameterized
Microsphere	A microsphere is a particle with a diameter in the micrometer range (typically 1 μm to 1000 μm (1 mm)). Microspheres can be manufactured from various natural and synthetic materials: glass, polymers and ceramics. In nuclear medicine, microspheres are labeled with various isotopes: ^{95}Nb, ^{113}Sn, ^{103}Ru and ^{46}Sc are common. Microspheres are generally used in animal studies. They are administered intraarterially and are trapped in the small capillaries of the tissue. The tissue of interest is counted later, typically in a well counter, to quantify absolute blood follow to that particular tissue of interest
Multi-resolution	The spatial parameterization can involve multi-resolution (also referred to as multigridding in this review). This refers to a spatial parameterization where inside an organ boundary of interest the image intensity (tracer concentration) is represented by high-resolution voxels, and outside the organ the distribution is modeled with a coarser resolution
Partition coefficient	The partition coefficient is the ratio of concentrations of a tracer in the blood to the concentration of the tracer in the tissue
Positron emission tomography (PET)	This is a nuclear medicine imaging technique that produces a 3D image or picture of functional processes in the body. The imaging system detects pairs of gamma rays emitted at 180° from one another by a positron-emitting radionuclide (tracer), which is introduced into the body on a biologically active molecule
Rate constant	In biochemical kinetics, a rate constant quantifies the speed of a biochemical reaction. In the present work, the rate constant times the concentration of a tracer in a compartment is equal to the rate of change of the concentration of the tracer from one compartment to another compartment (see compartment model)
Redistribution	This is the process of a radiopharmaceutical changing its concentration distribution in different regions of an organ over time due to differences in wash-in and wash-out between regions
Ring detector system versus system of multiple-gamma camera heads	A ring detector refers to a nuclear imaging system where the scintillation detectors are arranged in a ring surrounding the patient. A system of multiple-gamma camera heads refers to a SPECT system with multiple planar gamma cameras surrounding the patient. The cameras are rotated to obtain projection data
Scintillation detector	A scintillation detector containing material such as NaI(Tl) emits photons when incoming gamma rays interact with the scintillation material. The emitted photons are converted into electronic signals usually by photomultiplier tubes
Semi-conductor detector	A semi-conductor detector converts gamma rays directly to electronic signal using materials such as CdZnTe

Semi-direct method of estimation of kinetic model parameters	Here, the time–activity curves for the blood and tissue are first estimated from the projection data. Then the kinetic model parameters are estimated from the estimated time–activity curves for the blood and tissue
Single photon emission computed tomography (SPECT)	A nuclear medicine imaging technique that produces a 3D image or picture of functional processes in the body. The imaging system differs from PET in that it detects single gamma rays emitted by a radionuclide (tracer), which is introduced into the body on a biologically active molecule
Sinogram	A sinogram is the distribution of projection data displayed as image intensity values with one Cartesian coordinate corresponding to the projection bin and the other to the angle of the projection
Sinotimogram	A sinotimogram is a sinogram of a time-varying distribution corresponding to projection data represented by three coordinates—the angle, the projection bin and the time
Slow versus fast camera rotation	Slow camera rotation refers to a SPECT system with a camera gantry rotation of approximately $5°s^{-1}$ versus a fast camera rotation of $24°s^{-1}$
Time–activity curve	A time–activity curve is multiple data points at different times generated from a region of interest from the 3D distribution of the radiotracer
Tracer	A tracer in the context of this review is a substance containing a radioisotope that is used for tracking the *in vivo* biochemical and physiological process
Volume of distribution	The volume of distribution (V_D), also known as distribution volume, is a term used to quantify the distribution of a tracer between the blood and the extravascular tissue in the body. It is defined as the volume of the extravascular space that would give the same tracer concentration as that in the blood. It is usually considered the same as the partition coefficient and is calculated from K_1/k_2

List of variables

$\boldsymbol{B(t)}$	activity concentration in the blood (Bq/cc)
$\boldsymbol{C_{EV}(t)}$	activity concentration in some extravascular space
$\boldsymbol{V_{EV}}$	volume of the extravascular space (compartment)
$\boldsymbol{P_1}$	permeability coefficient for flux out of the capillary (cm min^{-1})
$\boldsymbol{P_2}$	permeability coefficient for flux into the capillary (cm min^{-1})
$\boldsymbol{S}$	surface area of the capillary in the sampled voxel (cm^2)

K_1	rate of exchange from blood into the extravascular compartment (units of min^{-1}—volume per minute per extravascular volume V_{EV})
k_2	rate of exchange from extravascular compartment into blood (units of min^{-1}—volume per minute per extravascular volume V_{EV})
$V_D = \lambda V_{EV}$	apparent distribution volume
$\lambda = C_{EV}(\infty)/B(\infty)$	partition coefficient (ratio of the tracer concentration in the tissue to that in the blood at equilibrium)
$A_T = f_v\, B(t) + (1 - f_v)\, C_{EV}(t)$	model of the measured myocardial tissue activity concentration at time t in some region of interest (ROI)
f_v	vascular fraction of blood in the tissue
$(1 - f_v)$	fractional volume of the extravascular space
$C(t)=\int_0^t e^{-k_2(t-\tau)} B(\tau)\,d\tau$	intermediate function for a one-compartment model, where $C_{EV}(t) = K_1 C(t)$
$A(x, t) = \Sigma_{m,n}\, a_{mn} S^m(x) V^{mn}(t)$	activity concentration distribution as a function of space and time
$S^m(x)$	spatial basis functions $m = 1, \ldots, M$
$V^{mn}(t)$	temporal basis functions $n = 1, \ldots, N$; $m = 1, \ldots, M$
a_{mn}	coefficients of the basis functions $S^m(t)V^{mn}(t)$
$P(d(t), t) = \int_\chi F[x, d(t)] A(x, t)\, dx$	projection of the tracer distribution written as a function of the detector position $d(t)$ and time t
$F\,[x, d(t)]$	fraction of activity $A(x, t)$ at spatial position x and time t that projects into the detector bin at position $d(t)$
$U^m(d(t), t) = \int_\chi F[x, d(t)] S^m(x)\, dx$	projection of the spatial basis function $S^m(x)$ at the detector sampling position $d(t)$
$p_i(t_k)=\int_{t_k-\Delta t_k}^{t_k} P(d_i(t), t)\,dt$	projection of activity acquired over the time $t_k - \Delta t_k$ to t_k for the detector bin positions $d_i(t)$
I	number of projection rays per projection angle

$\boldsymbol{K}$	number of time samples
$\boldsymbol{p = Fa}$	column vector of *IK* elements of projection data values
$\boldsymbol{F}$	system matrix with dimensions (*IK*) × (*MN*), where *I* is the total number of projection measurements, *K* is the number of time samples, *M* is the number of spatial basis functions and *N* is the number of temporal basis functions
$f_{ik(mn)}=\int_{t_k-\Delta t_k}^{t_k} U^m(d_i(t),t)V^{mn}(t)\,\mathrm{d}t$	elements of the system matrix *F*
$\boldsymbol{a}$	column vector with *MN* elements of basis coefficients
$\boldsymbol{V^{mn}(t) = V^n(t)}$	the temporal representation is independent of the spatial index *m*
$\boldsymbol{A(x,t) = \Sigma_{m,n}\, a_{mn} S^m(x) V^n(t)}$	spatiotemporal representation of the activity where the temporal basis function $V^n(t)$ is independent of the spatial basis function $S^m(t)$
$V^{mn}(t)=f_v^m V^n(t)+(1-f_v^m)K_1^m\int_0^t V^n(\tau)\,\mathrm{e}^{-k_2^m(t-\tau)}\mathrm{d}\tau$	temporal basis function for where the tissue region *m* is represented as a one-compartment model
	assuming $B(t)=\sum_n a_n^B V^n(t)$
$A(x,t)=\sum_{m,n} a_{mn} S^m(x)[f_v^m V^n(t)+(1-f_v^m)K_1^m C_{mn}(t;k_2^m)]$	spatiotemporal representation of activity assuming a one-compartment model for each tissue region *m*
$C_{mn}(t;k_2^m)=\int_0^t V^n(\tau)\,\mathrm{e}^{-k_2^m(t-\tau)}\mathrm{d}\tau$	intermediate function for a one-compartment model, where $C_{\mathrm{EV}}^m(t;K_1^m,k_2^m)=K_1^m\sum_n a_n^B C_{mn}(t;k_2^m)$
$C_m(t;k_2^m)=\int_0^t B(\tau)\,\mathrm{e}^{-k_2^m(t-\tau)}\mathrm{d}\tau$	intermediate function for a one-compartment model, where $C_m(t;k_2^m)=\sum_n a_n^B C_{mn}(t;k_2^m)$ assuming $B(t)=\sum_n a_n^B V^n(t)$
$V^{mn}(t)=V^n(t)=\sum_{k=1}^K F_{nk}\chi_k(t)$	temporal basis representation for the factor model where the temporal representation is independent of the spatial index *n* and for each index *n* there is a factor F_{nk} ($k = 1, \ldots, K$) independent of the index *m* and χ_k (*t*) is a characteristic function with

	$\chi_k(t) = 1$ for $t_k - \Delta t_k \le t \le t_k$ and 0 otherwise
$\boldsymbol{A(x,t) = \Sigma_{m,n,k}\, a_{mn} F_{nk}\, S^m(x)\, \chi_k(t)}$	spatiotemporal representation of the activity for the factor model
$\boldsymbol{\chi_B(x)}$	characteristic function of the segmented blood input
$\boldsymbol{\chi_G(x)}$	characteristic function of the segmented background
$\boldsymbol{\chi_m(x)}$	characteristic function of the myocardial tissue region m
$\boldsymbol{g}$	ratio of the concentration in the blood to the concentration in the background tissue
$B(t)=\sum_n a_n^B V^n(t)$	blood input function expressed as a function of a set of temporal basis functions $V^n(t)$.
$A_T^m(t)=f_v^m B(t)+(1-f_v^m)K_1^m C_m(t;k_2^m)$	one-compartment model for activity in the tissue-type m
K_1^m	rate of exchange from blood to extravascular compartment for tissue-type m
f_v^m	fraction of vasculature blood in tissue-type m
$\boldsymbol{\theta(t)}$	projection angle sampled at precisely the time t
$\boldsymbol{U^B(d(t),t) = \int_{\chi}\chi_B(x)F[d(t),x]\,dx}$	fraction of segmented blood that projects at detector position $d(t)$
$\boldsymbol{U^m(d(t),t) = \int_{\chi}\chi_m(x)F[d(t),x]\,dx}$	fraction of segmented tissue-type m that projects at detector position $d(t)$
$\boldsymbol{U^G(d(t),t) = \int_{\chi}\chi_G(x)F[d(t),x]\,dx}$	fraction of segmented background that projects at detector position $d(t)$
$u_i^n(t_k)=\int_{t_k-\Delta t_k}^{t_k} V^n(t)U^B(d_i(t),t)\,dt$	fraction of blood activity acquired over a time period Δt_k for detector bin at positions $d_i(t)$
$v_i^n(t_k)=\int_{t_k-\Delta t_k}^{t_k} V^n(t)U^G(d_i(t),t)\,dt$	fraction of background activity acquired over a time period Δt_k for detector bin at positions $d_i(t)$
$w_i^{mn}(t_k)=\int_{t_k-\Delta t_k}^{t_k} V^n(t)U^m(d_i(t),t)\,dt$	fraction of activity from segmented tissue-type m acquired over a time period Δt_k for detector bin i at positions $d_i(t)$

$$\Gamma_i^{mn}(t_k;k_2^m)=\int_{t_k-\Delta t_k}^{t_k}\int_0^t V^n(\tau)\times e^{-k_2^m(t-\tau)}U^m(d_i(t),t)\,d\tau\,dt$$

fraction of activity of the extravascular response to a unit basis input function $V^n(t)$ for tissue-type m acquired over a time period Δt_k for detector bin at positions $d_i(t)$

References

Aarsvold JN, Barrett HH, Chen J, Landesman AL, Milster TD, Patton DD, Roney TJ, Rowe RK, Seacat RH III, Strimbu LM. Modular scintillation cameras: a progress report. Proc SPIE. 1988; 914:319–25.

Acton PD, Thomas D, Zhou R. Quantitative imaging of myocardial infarct in rats with high resolution pinhole SPECT. Int J Cardiovasc Imaging. 2006; 22:429–34. [PubMed: 16518671]

Akahira H, Shirakawa H, Shimoyama H, Tsushima M, Arima H, Nigawara K, Funyu T, Sato M, Suzuki T. Dynamic SPECT evaluation of renal plasma flow using technetium-99m MAG3 in kidney transplant patients. J Nucl Med Technol. 1999; 27:32–7. [PubMed: 10322572]

Allman KC, Berry J, Sucharski LA, Stafford KA, Petry NA, Wysor W, Schwaiger M. Determination of extent and location of coronary artery disease in patients without prior myocardial infarction by thallium-201 tomography with pharmacologic stress. J Nucl Med. 1992; 33:2067–73. [PubMed: 1460494]

Alpert NM, Eriksson L, Chang JY, Bergstrom M, Litton JE, Correia JA, Bohm C, Ackerman RH, Taveras JM. Strategy for the measurement of regional cerebral blood flow using short-lived tracers and emission tomography. J Cereb Blood Flow Metab. 1984; 4:28–34. [PubMed: 6607259]

Bai C, Zeng GL, Gullberg GT. A slice-by-slice blurring model and kernel evaluation using the Klein-Nishina formula for 3D scatter compensation in parallel and converging beam SPECT. Phys Med Biol. 2000; 45:1275–307. [PubMed: 10843105]

Barber DC. The use of principal components in the quantitative analysis of gamma camera dynamic studies. Phys Med Biol. 1980; 25:283–92. [PubMed: 7384214]

Barber HB, Augustine FL, Barrett HH, Dereniak EL, Matherson KL, Meyers TJ, Perry DL, Venzon JE, Woolfenden JM, Young ET. Semiconductor arrays with multiplexer readout for gamma-ray imaging: results for a 48×48 Ge array. Nucl Instrum Methods Phys Res A. 1994; 353:361–5.

Barber HB, Barrett HH, Dereniak EL, Hartsough NE, Perry DL, Roberts PCT, Rogulski MM, Woolfenden JM, Young ET. Design for a high-resolution SPECT brain imager using semiconductor detector arrays and multiplexer readout. Phys Medica. 1993; 9:135–45.

Bard, Y. Nonlinear Parameter Estimation. New York: Academic Press; 1974.

Barrett HH, Wilson DW, Tsui BMW. Noise properties of the EM algorithm: I. Theory. Phys Med Biol. 1994; 39:833–46. [PubMed: 15552088]

Bassingthwaighte, JB.; Raymond, GM.; Chan, JI. Nuclear Cardiology: State of the Art and Future Directions. Zaret, BL.; Beller, GA., editors. St Louis, MO: Mosby; 1993. p. 3-23.

Bauschke HH, Noll D, Celler A, Borwein JM. An EM algorithm for dynamic SPECT. IEEE Trans Med Imaging. 1999; 18:252–61. [PubMed: 10363703]

Beck, JV.; Arnold, KJ. Parameter Estimation in Engineering and Science. New York: Wiley; 1977.

Beekman F, Van Der Have F. The pinhole: gateway to ultra-high-resolution three-dimensional radionuclide imaging. Eur J Nucl Med Mol Imaging. 2007; 34:151–61. [PubMed: 17143647]

Beekman FJ, de Jong HWAM, van Geloven S. Efficient fully 3-D iterative SPECT reconstruction with Monte Carlo-based scatter compensation. IEEE Trans Med Imaging. 2002; 21:867–77. [PubMed: 12472260]

Beekman FJ, Kamphuis C, Viergever MA. Improved SPECT quantitation using fully three-dimensional iterative spatially variant scatter response compensation. IEEE Trans Med Imaging. 1996; 15:491–9. [PubMed: 18215930]

Ben-Heim S, Kacperski K, Hain S, Van Gramberg D, Hutton BF, Erlandsson K, Sharir T, Roth N, Waddington WA, Berman DS, Ell PJ. Simultaneous dual-radionuclide myocardial perfusion imaging with a solid-state dedicated cardiac camera. Eur J Nucl Med Mol Imaging. 201010.1007/s00259-010-1441-1

Berman, DS. Advances in instrumentation: dedicated cardiac SPECT cameras Syllabus ASNC2007. 12th Annual Scientific Session of the American Society of Nuclear Cardiology; San Diego, CA. 2007. p. 60-7.

Boutchko R, Sitek A, Gullberg GT. Three-dimensional reconstruction of dynamic cardiac SPECT data on a point cloud grid (abstract). J Nucl Med. 2006a; 47:59.

Boutchko, R.; Sitek, A.; Hu, J.; Reutter, BW.; Gullberg, GT.; Botvinick, EH. Quantitative processing of cardiac dynamic patient data with slow camera rotation. 2006 IEEE Nuclear Science Symp. and Medical Imaging Conf; San Diego, CA. 2006b. p. 2933-5.

Boutchko R, Sitek A, Reutter BW, Gullberg GT. Adaptive optimization of point cloud grids for SPECT imaging. J Nucl Med. 2007; 48:100P. [PubMed: 17204705]

Bremner JD, et al. Quantitation of benzodiazepine receptor binding with PET [11C]iomazenil and SPECT [123]iomazenil preliminary results of a direct comparison in healthy human subjects. Psychairty Res. 1999; 91:79–91.

Brownlee, KA. Science and Engineering. 2. Malabar, FL: Robert E Kreiger; 1984. Statistical Theory and Methodology.

Brzymialkiewicz CN, Tornai MP, McKinley RL, Bowsher JE. Evaluation of fully 3-D emission mammotomography with a compact cadmium zinc telluride detector. IEEE Trans Med Imaging. 2005; 24:868–77. [PubMed: 16011316]

Budinger, TF. Advances in the instruments dedicated to imaging single photon radiopharmaceuticals. 6th Int. Symp. on Technetium in Chemistry and Nuclear Medicine; Bressanone, Italy. 4–7 September 2002; 2002. p. 617-36.

Budinger TF, Araujo L, Ranger N, Coxson P, Klein G, Huesman RH, Alavi A. Dynamic SPECT feasibility studies (abstract). J Nucl Med. 1991; 32:955P.

Buechel RR, et al. Ultrafast nuclear myocardial perfusion imaging on a new gamma camera with semiconductor technique: first clinical validation. Eur J Nucl Med Mol Imaging. 2010; 4:773–8. [PubMed: 20107783]

Buvat I, Benali H, Frouin F, Bazin J, Di Paola R. Target apex-seeking in factor analysis of medical sequences. Phys Med Biol. 1993; 38:123–37. [PubMed: 8426863]

Calnon DA, Ruiz M, Vanzetto G, Watson DD, Beller GA, Glover DK. Myocardial uptake of ^{99m}Tc-N-NOET and ^{201}Tl during dobutamine infusion. Comparison with adenosine stress. Circulation. 1999; 100:1653–9. [PubMed: 10517738]

Carson RE. A maximum likelihood method for region-of-interest evaluation in emission tomography. J Comput Assist Tomogr. 1986a; 10:654–63. [PubMed: 3488338]

Carson, RE. Positron Emission Tomography and Autoradiography: Principles and Applications for the Brain and Heart. Phelps, ME., et al., editors. New York: Raven; 1986b. p. 347-90.

Carson RE, Huang SC, Green MV. Weighted integration method for local cerebral blood flow measurements with positron emission tomography. J Cereb Blood Flow and Metab. 1986; 6:245–58. [PubMed: 3485644]

Celler AM, Farncombe TH, Bever CA, Noll D, Maeght J, Harrop R, Lyster D. Performance of the dynamic single photon emission computed tomography (dSPECT) method for decreasing or increasing activity changes. Phys Med Biol. 2001; 45:3525–43. [PubMed: 11131182]

Chang W, Ordonez C, Liang H, Holcomb M, Li Y, Liu J. C-SPECT/CT-2: design concepts and performance potential. J Nucl Med. 2008; 49:124P.

Chen, C-T. Linear System Theory and Design. New York: Holt, Rinehart and Winston; 1984.

Chen K, Huang SC, Yu DC. The effects of measurement errors in the plasma radioactivity curve on parameter estimation in positron emission tomography. Phys Med Biol. 1991; 36:1183–200. [PubMed: 1946602]

Chen W, Silverman DHS. Advances in evaluation of primary brain tumors. Semin Nucl Med. 2008; 38:240–50. [PubMed: 18514080]

Cherry, SR.; Sorenson, JA.; Phelps, ME. Physics in Nuclear Medicine. 3. Philadelphia, PA: Saunders; 2003.

Chiao P-C, Ficaro EP, Dayanikli F, Rogers WL, Schwaiger M. Compartmental analysis of technetium-99m-teboroxime kinetics employing fast dynamic SPECT at rest and stress. J Nucl Med. 1994a; 35:1265–73. [PubMed: 8046477]

Chiao P-C, Rogers WL, Clinthorne NH, Fessler JA, Hero AO. Model-based estimation for dynamic cardiac studies using ECT. IEEE Trans Med Imaging. 1994b; 13:217–26. [PubMed: 18218498]

Chiao P-C, Rogers WL, Fessler JA, Hero AO. Model-based estimation with boundary side information or boundary regularization. IEEE Trans on Med Imaging. 1994c; 13:227–34.

Choi Y, Hawkins RA, Huang SC, Gambhir SS, Brunken RC, Phelps MC, Schelbert HR. Parametric images of myocardial metabolic-rate of glucose generated from dynamic cardiac PET and 2-[f-18]fluoro-2-deoxy-d-glucose studies. J Nucl Med. 1991; 32:733–8. [PubMed: 2013815]

Choi Y, Huang SC, Hawkins RA, Kuhle WG, Dahlbom M, Hoh CK, Czernin J, Phelps ME, Schelbert HR. A simplified method for quantification of myocardial blood-flow using nitrogen-13-ammonia and dynamic PET. J Nucl Med. 1993; 34:488–97. [PubMed: 8280197]

Chua T, Kiat H, Germano G, Takemoto K, Fernandez G, Biasio Y, Friedman J, Berman D. Rapid back to back adenosine stress/rest technetium-99m teboroxime myocardial perfusion SPECT using a triple-detector camera. J Nucl Med. 1993; 34:1485–93. [PubMed: 8355068]

Coates C. Isotope lung imaging. Curr Opin Radiol. 1992; 4:79–86. [PubMed: 1326312]

Coxson P, Huesman RH, Borland L. Consequences of using a simplified kinetic model for dynamic PET data. J Nucl Med. 1997; 38:660–7. [PubMed: 9098221]

Cunningham VJ, Jones T. Spectral analysis of dynamic PET studies. J Cereb Blood Flow Metab. 1993; 13:15–23. [PubMed: 8417003]

Darambara DG, Todd-Pokropek A. Solid state detectors in nuclear medicine. Q J Nucl Med. 2002; 46:3–7. [PubMed: 12072840]

Dargham A, et al. SPECT measurement of benzodiazepine receptors in human brain with iodine-123-iomazenil: kinetic and equilbrium paradigms. J Nucl Med. 1994; 35:228–38. [PubMed: 8294990]

de Berg, M.; Cheong, O.; van Kreveld, M.; Overmars, M. Computational Geometry: Algorithms and Applications. New York: Springer; 2008.

Defrise M, Townsend D, Geissbuhler A. Implementation of three-dimensional image reconstruction for multi-ring positron tomographs. Phys Med Biol. 1990; 35:1361–72. [PubMed: 2243841]

Deutsch, R. Estimation Theory. Englewood Cliffs, NJ: Prentice-Hall; 1965.

Di Bella EV, Clackdoyle R, Gullberg GT. Blind estimation of compartmental model parameters. Phys Med Biol. 1999; 44:765–80. [PubMed: 10211809]

Di Bella EV, Ross SG, Kadrmas DJ, Khare HS, Christian PE, McJames S, Gullberg GT. Compartmental modeling of technetium-99m-labeled teboroxime with dynamic single-photon emission computed tomography: comparison with static thallium-201 in a canine model. Invest Radiol. 2001; 36:178–85. [PubMed: 11228582]

Di Bella EVR, Gullberg GT, Barclay AB, Eisner RL. Automated region selection for analysis of dynamic cardiac SPECT data. IEEE Trans Nucl Sci. 1997; 44:1355–61.

Di Paola R, Bazin JP, Aubry F, Auengo A, Cavailloles F, Herry Y, Kahn E. Handling of dynamic sequences in nuclear medicine. IEEE Trans Nucl Sci. 1982; 29:1310–21.

Dixon, WJ.; Massey, FJ. Introduction to Statistical Analysis. New York: McGraw-Hill; 1969.

Draper, NR.; Smith, H. Applied Regression Analysis. New York: Wiley; 1966.

Eberl, S. Graduate School of Biomedical Engineering. Sydney, Australia: University of New South Wales; 2000. Quantitative physiologocal parameter estimation from dynamic single photon emission computed tomography (SPECT).

Ercan MT, Ulutuncel N, Naldoken S. Evaluation of 99mTc-labelled alpha-d-glucose 1-phosphate aerosols for SPECT ventilation lung imaging. Nucl Med Commun. 1993; 14:433–8. [PubMed: 8321483]

Erlandsson K, Kacperski K, van Gramberg D, Hutton BF. Performance evaluation of D-SPECT: a novel SPECT system for nuclear cardiology. Phys Med Biol. 2009; 54:2635–49. [PubMed: 19351981]

Esteves, FP.; Raggi, P.; Folks, RD.; Keidar, Z.; Askew, JW.; Rispler, S.; O'Connor, MK.; Verdes, L.; Garcia, EV. Novel ultrafast cardiac camera in myocardial perfusion SPECT: initial multicenter comparison with standard dual detector cameras. Proc. Annual Scientific Session of the American Society of Nuclear Cardiology—Late-Breaking Clinical Trials; Boston, MA. 2008.

Farncombe T, Noll D, Maeght J, Harrop R. Dynamic SPECT imaging using a single camera rotation (dSPECT). IEEE Trans Nucl Sci. 1999; 46:1055–61.

Farncombe, TH. Functional Dynamic SPECT Imaging Using a Single Slow Camera Rotation. Vancouver, BC, Canada: University of British Columbia; 2000.

Farncombe, TH.; Blinder, S.; Celler, A.; Noll, D.; Maeght, J.; Harrop, R. A dynamic expectation maximization algorithm for single camera rotation dynamic SPECT (dSPECT). 2000 IEEE Nuclear Science and Medical Imaging Conference ; Lyon, France. 2000. p. 15/31-15/35.

Farncombe TH, Celler AM, Bever CA, Noll D, Maeght J, Harrop R. The incorporation of organ uptake into dynamic SPECT (dSPECT) image reconstruction. IEEE Trans Nucl Sci. 2001; 48:3–9.

Farncombe, TH.; Feng, B.; King, MA.; Leppo, JA. Investigating acquisition protocols for gated, dynamic myocardial imaging in PET and SPECT. 2003 IEEE Nuclear Science Symp. and Medical Imaging Conf. Record; Portland, Oregon. 19–25 October 2003; 2003a. p. 3272-5.

Farncombe, TH.; Feng, B.; Narayanan, MV.; Wernick, MN.; Celler, AM.; King, MA.; Leppo, JA. Toward 5 dimensional SPECT reconstruction: determining myocardial blood flow and wall motion in a single study. In: Bizais, Y., editor. Proc. 2003 International Meeting on Fully Three-Dimensional Image Reconstruction in Radiology and Nuclear Medicine; Saint Malo, France. 29 June–4 July 2003; 2003b. p. 218-21.

Feichtinger J, Schrottner T, Schwaiger M, Kindl P. Characterisation of selected cadmium–zinc–telluride detectors. Appl Radiat Isot. 2004; 61:113–5. [PubMed: 15177330]

Feng B, Pretorius PH, Farncombe TH, Dahlberg ST, Narayanan MV, Wernick MN, Celler AM, King MA, Leppo JA. Imaging time-varying Tc-99m teboroxime localization and cardiac function simultaneously by five-dimensional (5D) gated-dynamic SPECT imaging and reconstruction (abstract). J Nucl Cardiol. 2003a; 2:S11–S2.

Feng B, Pretorius PH, Farncombe TH, Dahlberg ST, Narayanan MV, Wernick MN, Celler AM, Leppo JA, King MA. Simultaneous assessment of cardiac perfusion and function using 5-dimensional imaging with Tc-99m teboroxime. J Nucl Cardiol. 2006; 13:354–61. [PubMed: 16750780]

Feng D, Huang SC, Wang X. Models for computer simulation studies of input functions for tracer kinetic modelling with positron emission tomography. Int J Bio-Med Comput. 1993; 32:95–110.

Feng H, Karl WC, Castanon DA. A curve evolution approach to object-based tomographic reconstruction. IEEE Trans Image Process. 2003b; 12:44–57. [PubMed: 18237878]

Fessler J. Mean and variance of implicitly defined biased estimators (such as penalized maximum likelihood): applications to tomography. IEEE Trans Image Process. 1996; 5:493–506. [PubMed: 18285134]

Fick A. Sitzungsbder Phys-Med Geszu Wurzburg. 1870:36.

Flamen P, Bossuyt A, Franken PR. Technetium-99m-tetrofosmin in dipyridamole-stress myocardial SPECT imaging: intraindividual comparison with technetium-99m-sestamibi. J Nucl Med. 1995; 36:2009–15. [PubMed: 7472590]

Floyd CE, Jaszczak RJ, Coleman RE. Inverse Monte Carlo: a unified reconstruction algorithm for SPECT. IEEE Trans Nucl Sci. 1985; 32:779–85.

Fluckiger JU, Schabel MC, DiBella EVR. Model-based blind estimation of kinetic parameters in DCE-MRI. Magn Reson Med. 2009; 62:1477–86. [PubMed: 19859949]

Formiconi AR. Least squares algorithm for region-of-interest evaluation in emission tomography. IEEE Trans Med Imaging. 1993; 12:90–100. [PubMed: 18218397]

Formiconi AR, Pupi A, Passeri A. Compensation of spatial system response in SPECT with conjugate gradient reconstruction technique. Phys Med Biol. 1989; 34:69–84. [PubMed: 2784572]

Forrer F, Valkema R, Bernard B, Schramm NU, Hoppin JW, Rolleman E, Krenning EP, de Jong M. *In vivo*radionuclide uptake quantification using a multi-pinhole SPECT system to predict renal function in small animals. Eur J Nucl Med Mol Imaging. 2006; 33:1214–7. [PubMed: 16832630]

Frey EC, Tsui BMW. A practical method for incorporating scatter in a projector-backprojector for accurate scatter compensation in SPECT. IEEE Trans Nucl Sci. 1993; 40:1107–16.

Frey, EC.; Tsui, BMW. A new method for modeling the spatially-variant, object-dependent scatter response function in SPECT. IEEE 1996 Nuclear Science Symp. and Medical Imaging Conf. Record; 1997. p. 1082-6.

Furenlid LR, Wilson DW, Chen YC, Kim H, Pietraski PJ, Crawford MJ, Barrett HH. FastSPECT II: a second-generation high-resolution dynamic SPECT imager. IEEE Trans Nucl Sci. 2004; 51:631–5. [PubMed: 20877439]

Gambhir SS, Berman DS, Ziffer J, Nagler M, Sandler M, Patton J, Hutton B, Sharir T, Ben Haim B, Ben Haim S. A novel high-sensitivity rapid-acquisition singe-photon cardiac imaging camera. J Nucl Med. 2009; 50:635–43. [PubMed: 19339672]

Gambhir SS, Schwaiger M, Huang SC, Krivokapich J, Schelbert HR, Nienaber CA, Phelps ME. Simple noninvasive quantification method for measuring myocardial glucose utilization in humans employing positron emission tomography and fluorine-18 deoxyglucose. J Nucl Med. 1989; 30:359–66. [PubMed: 2786939]

Garcia EV, Tsukerman L, Keidar Z. A new solid state, ultrafast cardiac multi-detector SPECT system (abstract). J Nucl Cardiol. 2008; l:15, S3.

Genna S, Smith AP. The development of ASPECT, an annular single crystal bain camera for high efficency SPECT. IEEE Trans Nucl Sci. 1988; 35:654–8.

Gill SS, Patel NK, Hotton GR, O'Sullivan K, McCarter R, Bunnage M, Brooks DJ, Svendsen CN, Heywood P. Direct brain infusion of glial cell line-derived neurotrophic factor in Parkinson disease. Nat Med. 2003; 9:589–95. [PubMed: 12669033]

Gioia G, Milan E, Giubbini R, DePace N, Heo J, Iskandrian AS. Prognostic value of tomographic rest-redistribution thallium 201 imaging in medically treated patients ventricular dysfunction. J Nucl Cardiol. 1996; 3:150–6. [PubMed: 8799240]

Glick SJ, Penney BC, King MA, Byrne CL. Non iterative compensation for the distance-dependent detector response and photon attenuation in SPECT imaging. IEEE Trans Med Imaging. 1994; 13:363–74. [PubMed: 18218512]

Goffin K, Dedeurwaerdere S, van Laere K, van Paesschen W. Neuronuclear assessment of patients with epilepsy. Semin Nucl Med. 2008; 38:227–39. [PubMed: 18514079]

Gravier E, Yang Y, Jin M. Tomographic reconstruction of dynamic cardiac image sequences. IEEE Trans Imaging Process. 2007; 16:932–42.

Gullberg, GT.; Boutchko, R.; Sitek, A.; Reutter, BW.; Botvinick, EH. Dynamic cardiac SPECT with slow camera rotation (abstract). 8th Int. Conf. of Nuclear Cardiology; Prague, Czech Republic. 29 April–2 May 2007; 2007a.

Gullberg, GT.; Budinger, TF.; Maltz, JS. Dynamic cardiac SPECT imaging of photon tracers. American Society of Nuclear Cardiology 5th Invitational Conf; Bar Harbor, Maine. 2000.

Gullberg, GT.; Hu, J.; Sitek, A.; Reutter, BW.; Huesman, RH.; Hanrahan, SM.; VanBrocklin, HF.; Brennan, KM.; Qi, J.; Feng, Y. A study of changes in glucose and fatty acid metabolism in the heart as a function of hypertrophy in SHR models using microPET and microSPECT technology. 53rd Annual Meeting of the Society of Nuclear Medicine Conf. Record; San Diego, CA. 2006. p. 72

Gullberg, GT.; Huesman, RH.; DiBella, EVR.; Reutter, BW. Clinical Nuclear Cardiology: State of the Art and Future Directions. 3. Zaret, BL.; Beller, GA., editors. Philadelphia, PA: Elsevier/Mosby; 2004. p. 117-39.

Gullberg GT, Huesman RH, Malko JA, Pelc NJ, Budinger TF. An attenuated projector-backprojector for iterative SPECT reconstruction. Phy Med Biol. 1985; 30:799–816.

Gullberg, GT.; Huesman, RH.; Ross, SG.; DiBella, EVR.; Zeng, GL.; Reutter, BW.; Christian, PE.; Foresti, SA. Nuclear Cardiology: State of the Art and Future Directions. Zaret, BL.; Beller, GA., editors. St. Louis, MO: Mosby; 1999. p. 137-87.

Gullberg, GT.; Veress, A.; Sitek, A.; Boutchko, R.; Reutter, BW.; Huesman, RH. Tomographic Reconstruction of Tracer Kinetics in the Heart Using a Spatiotemporal Mechanical Model. Proc. 9th Int. Meeting on Fully Three-Dimensional Image Reconstruction in Radiology and Nuclear Medicine; Lindau, Germany. 9–13 July 2007; 2007b. p. 425-8.

Gullberg GT, Zeng GL, Tsui BMW, Hagius JT. An iterative reconstruction algorithm for single photon emission computed tomography with cone beam geometry. Int J of Imag Sys & Techn. 1989; 1:169–86.

Gunn RN, Gunn SR, Cunningham VJ. Positron emission tomography compartmental models. J Cereb Blood Flow Metab. 2001; 21:635–52. [PubMed: 11488533]

Hamilton WF, Moore JW, Kinsman JM. Simultaneous determination of the pulmonary and systemic circulation times in man and of a figure related to the cardiac output. Am J Physiol. 1928; 84:338–44.

Hansen L, Marzilli LG, Eshima D, Malveaux EJ, Folks R, Taylor AJ. Evaluation of technetium-99m-triamide-mercaptide complexes designed to identify properties favoring renal tubular transport. J Nucl Med. 1994; 35:1198–205. [PubMed: 8014683]

Hebber E, Oldenburg D, Farncombe T, Celler A. Direct estimation of dynamic parameters in SPECT tomography. IEEE Trans on Nucl Sci. 1997; 44:2425–30.

Heller GV, Calnon D, Dorbala S. Recent advances in cardiac PET and PET/CT myocardial perfusion imaging. J Nucl Cardiol. 2009; 6:962–9. [PubMed: 19756909]

Henkin, RE.; Bova, D.; Dillehay, GL.; Karesh, SM.; Halama, JR.; Wagner, RH.; Zimmer, AM. Nuclear Medicine. 2. St Louis, MO: Mosby; 2006.

Herrero P, Markham J, Bergmann SR. Quantitation of myocardial blood flow with $H_2{}^{15}O$ and positron emission tomography: assessment and error analysis of a mathematical approach. J Comput Assist Tomogr. 1989; 13:862–73. [PubMed: 2789240]

Hicks K, Ganti G, Mullani N, Gould KL. Automated quantitation of three-dimensional cardiac positron emission tomography for routine clinical use. J Nucl Med. 1989; 30:1787–97. [PubMed: 2809743]

Hirai T, Nohara R, Ogoh S, Chen LG, Kataoka K, Li XH, Fujita M, Matsumori A, Taguchi S, Sasayama S. Serial evaluation of fatty acid metabolism in rats with myocardial infarction by pinhole SPECT. J Nucl Cardiol. 2001; 8:472–81. [PubMed: 11481570]

Hirose Y, Ikeda Y, Higashi Y, Koga K, Hattori H, Kanno I, Miura Y, Miura S, Uemura K. A hybrid emission CT Headtome II. IEEE Trans Nucl Sci. 1982; 29:520–5.

Houston AS, Sampson WFD. A quantitative comparison of some FADS methods in renal dynamic studies using simulated and phantom data. Phys Med Biol. 1997; 42:199–217. [PubMed: 9015818]

Hu, J.; Boutchko, R.; Sitek, A.; Reutter, BW.; Huesman, RH.; Gullberg, GT. LBNL Report No LBNL-60008. Berkeley: Lawrence Berkeley National Lab; 2008. Dynamic molecular imaging of cardiac innervation using a dual head pinhole SPECT system.

Hu, J.; Sitek, A.; Reutter, BW.; Huesman, RH.; Gullberg, GT. A new approach of dynamic pinhole SPECT imaging for evaluation of sympathetic nervous system function in animal models of cardiac hypertrophy. Conf. Record of the 2005 IEEE Nuclear Science Symp. and Medical Imaging Conf; Puerto Rico. 2005. p. 2542-6.

Huang, S-C.; Phelps, ME. Positron Emission Tomography and Autoradiography: Principles and Applications for the Brain and Heart. Phelps, ME., et al., editors. New York: Raven; 1986. p. 287-346.

Hudson, HM.; Walsh, C. Density deconvolution using spectral mixture models. Proc. 2nd World Congress of the IASC; Pasadena, CA. 1997. p. 593-9.

Huesman RH. A new fast algorithm for the evaluation of regions of interest and statistical uncertainty in computed tomography. Phys Med Biol. 1984; 29:543–52. [PubMed: 6610883]

Huesman, RH.; Knittel, BL.; Mazoyer, BM.; Coxson, PG.; Salmeron, EM.; Klein, GJ.; Reutter, BW.; Budinger, TF. BNL Report No LBNL-37621. Berkeley: Lawrence Berkeley National Laboratory; 1995. Notes on RFIT: a program for fitting compartment models to region-of-interest dynamic emission tomography data.

Huesman RH, Mazoyer BM. Kinetic data analysis with a noisy input function. Phys Med Biol. 1987; 32:973–82.

Huesman RH, Reutter BW, Zeng GL, Gullberg GT. Kinetic parameter estimation from SPECT cone-beam projection measurements. Phys Med Biol. 1998; 43:973–82. [PubMed: 9572520]

Hutton BF, Hudson HM, Beckman FJ. A clinical perspective of accelerated statistical reconstruction. Eur J Nucl Med. 1997; 24:797–808. [PubMed: 9211768]

Iida H, Bloomfield PM, Miura S, Kanno I, Murakami M, Uemure K, Amano M, Tanaka K, Hirose Y, Yamamoto S. Effect of real-time weighted integration system for rapid calculation of functional images in clinical positron emission tomography. IEEE Trans Med Imag. 1995a; 14:116–21.

Iida H, Eberl S. Quantitative assessment of regional myocardial blood flow with thallium-201 and SPECT. J Nucl Cardiol. 1998; 5:313–31. [PubMed: 9669586]

Iida H, Eberl S, Kim K-M, Tamura Y, Ono Y, Nakazawa M, Sohlberg A, Zeniya T, Hayashi T, Watabe H. Absolute quantitation of myocardial blood flow with ^{201}Tl and dynamic SPECT in canine: optimization and validation of kinetic modelling. Eur J Nucl Med Mol Imaging. 2008; 35:896–905. [PubMed: 18202845]

Iida H, Hayashida K, Nakazawa M, Katabuchi T. Multicenter evaluation of quantitative SPECT reconstruction package—QSPECT & DTARG. J Nucl Med. 2006; 47:121. abstract.

Iida H, Itoh H, Nakazawa M, Hatazawa J, Nishimura H, Onishi Y, Uemura K. Quantitative mapping of regional cerebral blood flow using iodine-123-IMP and SPECT. J Nucl Med. 1994; 35:2019–30. [PubMed: 7989987]

Iida H, Rhodes CG, de Silva R, Araujo LI, Bloomfield PM, Lammertsma AA, Jones T. Use of the left ventricular time-activity curve as a noninvasive input function in dynamic oxygen-15-water positron emission tomography. J Nucl Med. 1992; 33:1669–77. [PubMed: 1517842]

Iida H, Rhodes CG, de Silva R, Yamamoto Y, Araujo LI, Maseri A, Jones T. Myocardial tissue fraction correction for partial volume effects and measure of tissue viability. J Nucl Med. 1991; 32:2169–75. [PubMed: 1941156]

Iida H, Takahashi A, Yoshikazu Tamura Y, Ono Y, Lammertsma AA. Myocardial blood flow: comparison of oxygen-15-water bolus injection, slow infusion and oxygen-15-carbon dioxide slow inhalation. J Nucl Med. 1995b; 36:78–35. [PubMed: 7799088]

Iida I, Hayashi T, Eberl S, Saji H. Quantification in SPECT cardiac imaging. J Nucl Med. 2003; 44:40–2. [PubMed: 12515875]

Iihara K, Okawa M, Hishikawa T, Yamada N, Fukushima K, Iida H, Miyamoto S. Slowly progressive neuronal death associated with postischemic hyperfusion in cortical laminar necrosis after high-flow bypass for a carotid intracavenous aneurysm (abstract). J Neurosurg. 2009; 112:1254–8. [PubMed: 19877803]

Imaizumi M, et al. Misery perfusion with split-dose I[123]iodoamphetamine single-photon emission computed tomography in patients with carotid occlusive diseases. Stroke. 2002; 33:2217–23. [PubMed: 12215590]

Ito K, Momose T, Kotaki H, Kojima Y, Yamamoto K, Katashima M, Sawada Y, Saski Y, Iga T. Pharmacokinetic analysis of benzodiazepine receptor binding of [123]iomazenil in human brain. Phar Res. 1997; 8:999–1003.

Jagust WJ, Haan MN, Reed BR, Eberling JL. Brain perfusion imaging predicts survival in Alzheimer's disease. Neurology. 1998; 51:1009–13. [PubMed: 9781521]

Jagust WJ, Landau SM, Shaw LM, Trojanowski JQ, Koeppe RA, Reiman EM, Foster NL, Petersen RC, Weiner MW, Price JC, Mathis CA. Alzheimer's Disease Neuroimaging Initiative. Relationships between biomarkers in aging and dementia. Neurology. 2009; 73:1193–9. [PubMed: 19822868]

Jagust WJ, Thisted R, Devous MD, VanHeertum R, Mayberg H, Jobst K, Smith D, Borys N. SPECT perfusion imaging in the diagnosis of Alzheimer's disease: a clinical-pathological study. Neurology. 2001; 56:950–6. [PubMed: 11294935]

James, RB.; Schlesinger, TE.; Lund, J.; Schieber, M. Semiconductors for Room Temperature Nuclear Detector Applications Semiconductors and Semimetals. Schlesinger, TE.; James, RB., editors. San Diego: Academic; 1995. p. 335-81.

Jin, M.; Yang, Y.; Wernick, MN.; King, MA. Reconstruction of dynamic gated cardiac SPECT. Conf. Record of the 2005 IEEE Nuclear Science Symp. and Medical Imaging Conf; San Juan, Puerto Rico. 26–29 October 2005; 2005. p. 2342-45.

Jin, M.; Yang, Y.; Wernick, MN.; King, MA. Fully 5D reconstruction of gated dynamic cardiac SPECT images. Conf. Record of the 2006 IEEE Nuclear Science Symp. and Medical Imaging Conf; San Diego, CA. 29 October–1 November; 2006a. p. 3445-8.

Jin, M.; Yang, Y.; Wernick, MN.; King, MA. Motion-compensated dynamic image reconstruction for gated cardiac SPECT. Proc. of IEEE Int. Symp. Biomed Imaging: Macro to Nano; 2006b. p. 267-70.

Johnson G III, Allton IL, Nguyen KN, Lauinger JM, Beju D, Pasqualini R, Duatti A, Okada RD. Clearance of technetium 99m N-NOET in normal, ischemic-reperfused, and membrane-disrupted myocardium. J Nucl Cardiol. 1996; 3:42–54. [PubMed: 8799227]

Kadrmas DJ, Di Bella EVR, Huesman RH, Gullberg GT. Analytical propagation of errors in dynamic SPECT: estimators, degrading factors, bias, and noise. Phys Med Biol. 1999; 44:1997–2014. [PubMed: 10473210]

Kadrmas DJ, Frey EC, Karimi SS, Tsui BMW. Fast implementations of reconstruction-based scatter compensation in fully 3D SPECT image reconstruction. Phys Med Biol. 1998; 43:857–74. [PubMed: 9572510]

Kadrmas DJ, Gullberg GT. 4D maximum a posteriori reconstruction in dynamic SPECT using a compartmental model-based prior. Phys Med Biol. 2001; 46:1553–74. [PubMed: 11384070]

Kety SS, Schmidt CF. The nitrous oxide method for the quantitative determination of cerebral blood flow in man: theory, procedure and normal values. J Clin Invest. 1948; 27:476–83.

Kimura K, et al. A new apparatus for brain imaging: four-head rotating gamma camera single-photon emission computed tomograph. J Nucl Med. 1990; 31:603–9. [PubMed: 2341896]

King MA, Tsui BMW, Pan T-S. Attenuation compensation for cardiac single-photon emission computed tomographic imaging: part 1. Impact of attenuation and methods of estimating attenuation maps. J Nucl Cardiol. 1995; 2:513–24. [PubMed: 9420834]

King MA, Tsui BMW, Pan T-S, Glick SJ, Soares EJ. Attenuation compensation for cardiac single-photon emission computed tomographic imaging: part 2. Attenuation compensation algorithms. J Nucl Cardiol. 1996; 3:55–64. [PubMed: 8799228]

Komatani A, Sugai Y, Hosoya T. Development of ‘super rapid dynamic SPECT,’ and analysis of retention process of ^{99m}Tc-ECD in ischemic lesions: comparative study with ^{133}Xe SPECT. Annals Nucl Med. 2004; 18:489–94.

Kordower JH. Neurodegeneration prevented by lentiviral vector delivery of GDNF in primate models of Parkinson’s disease. Science. 2000; 290:767–73. [PubMed: 11052933]

Kuhl DE, Edwards RQ. Image separation radioisotope scanning. Radiology. 1963; 80:653–62.

Kuhl DE, Edwards RQ, Ricci AR, Yacob RJ, Mich TJ, Alavi A. The Mark IV system for radionuclide computed tomography of the brain. Radiology. 1976; 121:405–13. [PubMed: 981619]

Kung HF, Kung MP, Choi SR. Radiopharmaceuticals for single-photon emission computed tomography brain imaging. Semin Nucl Med. 2003; 33:2–13. [PubMed: 12605353]

Laforest R, Sharp TL, Engelbach JA, Fettig NM, Herrero P, Kim J, Lewis JS, Rowland DJ, Tai YC, Welch M. Measurement of input functions in rodents: challenges and solutions. J Nucl Med Biol. 2005; 7:679–85.

Lanczos, C. Applied Analysis. Englewood Cliffs, NJ: Prentice-Hall; 1956.

Lange K, Carson RE. EM reconstruction algorithms for emission and transmission tomography. J Comput Assist Tomogr. 1984; 8:306–16. [PubMed: 6608535]

Laurette I, Zeng GL, Welch A, Christian PE, Gullberg GT. A three-dimensional ray-driven attenuation, scatter and geometric response correction technique for SPECT in inhomogeneous media. Phys Med Biol. 2000; 45:3459–80. [PubMed: 11098917]

Leppo JA, DePuey EG, Johnson LL. A review of cardiac imaging with sestamibi and teboroxime. J Nucl Med. 1991; 32:2012–22. [PubMed: 1833519]

Leppo JA, Meerdink D. Comparison of the myocardial uptake of a technetium-labeled isonitrile analogue and thallium. J Circ Res. 1989; 65:632–9.

Levitan E, Herman GT. A maximum a posteriori probability expectation maximization algorithm for image reconstruction in emission tomograpjy. IEEE Trans Med Imaging. 1987; 6:185–92. [PubMed: 18244020]

Liang Z, Turkington TG, Gilland DR, Jaszczak RJ, Coleman RE. Simultaneous compensation for attenuation, scatter, and detector response for SPECT reconstruction in three dimensions. Phys Med Biol. 1992; 37:587–603. [PubMed: 1565692]

Lim Y, et al. Triangular SPECT system for 3D total organ volume imaging: design concept and preliminary results. IEEE Trans Nucl Sci. 1985; 32:741–7.

Limber MA, Limber MN, Celler A, Barney JS, Borwein JM. Direct reconstruction of functional parameters for dynamic SPECT. IEEE Trans Nucl Sci. 1995; 42:1249–56.

Lodge MA, Braess H, Mahmoud F, Suh J, Englar N, Geyser-Stoops S, Jenkins J, Bacharach SL, Dilsizian V. Developments in nuclear cardiology: transition from single photon emission computed tomography to positron emission tomography-computed tomography. J Invasive Cardiol. 2005; 17:491–6. [PubMed: 16145241]

Logan J. Graphical analysis of PET data applied to reversible and irreversible tracers. Nucl Med Biol. 2000; 27:661–70. [PubMed: 11091109]

Luke PN, Amman M. Room-temperature replacement for Ge detectors—are we there yet? IEEE Trans Nucl Sci. 2007; 54:834–42.

Maguire RP, Calonder C, Leenders KL. An investigation of multiple time graphical analysis applied to projection data: theory and validation. J Comput Assist Tomogr. 1997; 21:327–31. [PubMed: 9071312]

Maltz JS. Direct recovery of regional tracer kinetics from temporally inconsistent dynamic ECT projections using dimension-reduced time-activity basis. Phys Med Biol. 2000a; 45:3413–29. [PubMed: 11098914]

Maltz JS. Region resolvability versus noise level characteristics for joint spatial and kinetic parameter estimation in inconsistent projection dynamic ECT. IEEE Trans Nucl Sci. 2000b; 47:1143–8.

Maltz JS. Optimal time-activity basis selection for exponential spectral analysis: application to the solution of large dynamic emission tomographic reconstruction problems. IEEE Trans Nucl Sci. 2001; 48:1452–64.

Maltz JS. Parsimonious basis selection in exponential spectral analysis. Phys Med Biol. 2002; 47:2341–65. [PubMed: 12164591]

Maltz JS, Budinger TF. Multiresolution constrained least-squares algorithm for direct estimation of time activity curves from dynamic ECT projection data. Proc SPIE. 2000; 3979:586–98.

Maltz, JS.; Polak, E.; Budinger, TF. Multistart optimization algorithm for joint spatial and kinetic parameter estimation from dynamic ECT projection data. IEEE Nuclear Science Symp. and Medical Imaging Conf.; Toronto, Canada. 1998. p. 1567-73.

Marshall RC, Powers-Risius P, Reutter BW, Taylor SE, VanBrocklin HF, Huesman RH, Budinger TF. Kinetic analysis of ^{125}I-iodorotenone as a deposited myocardial flow tracer: comparison with ^{99m}Tc-sestamibi. J Nucl Med. 2001; 42:272–81. [PubMed: 11216526]

Massoud TF, Gambhir SS. Molecular imaging in living subjects; seeing fundamental biological processes in a new light. Genes Dev. 2003; 17:545–80. [PubMed: 12629038]

Matthews J, Bailey D, Price P, Cunningham V. The direct calculation of parametric images from dynamic PET data using maximum-likelihood iterative reconstruction. Phys Med Biol. 1997; 42:1155–73. [PubMed: 9194135]

Maublant JC, Marcaggi X, Lusson J-R, Boire J-Y, Cauvin J-C, Jacob P, Veyre A, Cassagnes J. Comparison between thallium-201 and technetium-99m methoxyisobutyl isonitrile defect size in single-photon emission computed tomography at rest, exercise and redistribution in coronary artery disease. Am J Cardiol. 1992; 69:183–7. [PubMed: 1731457]

Maublant JC, Moins N, Gachon P, Renoux M, Zhang Z, Veyre A. Uptake of technetium-99m-teboroxime in cultured myocardial cells: comparison with thallium-201 and technetium-99m-sestamibi. J Nucl Med. 1993; 34:255–9. [PubMed: 8429344]

Maunoury C, Chen CC, Chua KB, Thompson CJ. Quantification of left ventricular function with thallium-201 and technetium-99m-sestamibi myocardial gated SPECT. J Nucl Med. 1996; 38:958–61. [PubMed: 9189150]

McCarthy AW, Miller MM. Maximum likelihood SPECT in clinical computation times using mesh-connected parallel computers. IEEE Trans Med Imaging. 1991; 10:426–36. [PubMed: 18222845]

Meier P, Zierler KL. On the theory of the indicator-dilution method for measurement of blood flow and volume. J Appl Physiol. 1954; 6:731–44. [PubMed: 13174454]

Meikle SR, Hutton BF, Bailey DL. A transmission-dependent method for scatter correction in SPECT. J Nucl Med. 1994; 35:360–67. [PubMed: 8295011]

Meikle SR, Matthews J, Cunningham VJ, Bailey DL, Livieratos L, Jones T, Price P. Parametric image reconstruction using spectral analysis of PET projection data. Phys Med Biol. 1998; 43:651–66. [PubMed: 9533143]

Meikle, SR.; Matthews, JC.; Cunningham, VJ.; Bailey, DL.; Livieratos, L.; Jones, T.; Price, P. Spectral analysis of PET projection data. 1996 IEEE Nuclear Science Symp. and Medical Imaging Conf; Anaheim, CA. 1996. p. 1888-92.

Metzler SD, Jaszczak RJ, Patil NH, Vemulapalli S, Akabani G, Chin BB. Molecular imaging of small animals with a triple-head SPECT system using pinhole collimation. IEEE Trans Med Imaging. 2005; 24:853–62. [PubMed: 16011314]

Meyer JH. Applying neuroimaging ligands to study major depressive disorder. Semin Nucl Med. 2008; 38:287–304. [PubMed: 18514084]

Moore SC, Mueller SP. Inversion of the 3D radon transform for a multidetector, point-focused SPECT brain scanner. Phys Med Biol. 1986; 31:207–21. [PubMed: 3487093]

Moriwaki H, Matsumoto M, Hashikawa K, Oku N, Ishida M, Seike Y, Fukuchi K, Hori M, Nishimura T. Iodine-123-iomazenil and iodine-123-lodoamphetamine SPECT in major cerebral artery occlusive disease. J Nucl Med. 1998; 39:1348–53. [PubMed: 9708504]

Nakajima K, Taki J, Bunko H, Matsudaira M, Muramori A, Matsunari I, Hisada K, Ichihara T. Dynamic acquisition with a three-headed SPECT system: application to technetium-99m-SQ30217 myocardial imaging. J Nucl Med. 1991; 32:1273–7. [PubMed: 2045946]

Nakamura M, Suzuki Y, Kobayashi S. A method for recovering physiological components from dynamic radionuclide images using the maximum entropy principle: a numerical investigation. IEEE Trans Biomed Eng. 1989; 36:906–16. [PubMed: 2673986]

Nakano S, Kinoshita K, Jinnouchi S, Hoshi H, Watanabe K. Dynamic SPECT with iodine-123 IMP in meningiomas. J Nucl Med. 1988; 29:1627–32. [PubMed: 3262724]

Narra RK, Feld RT, Nunn AD. Absorbed radiation dose to humans from technetium-99m-teboroxime. J Nucl Med. 1992; 33:88–93. [PubMed: 1731003]

Nichols, TE.; Qi, J.; Leahy, RM. Continuous time dynamic PET imaging using list mode data. In: Kuba, A., et al., editors. Information Processing in Medical Imaging: Proc. 16th Int. Conf; 1999. p. 98-111.

Nijran KS, Barber DC. Towards automatic analysis of dynamic radionuclide studies using principal-components factor analysis. Phys Med Biol. 1985; 30:1315–25. [PubMed: 3911221]

Ogasawara K, Konno H, Yasuda S, Yukawa H, Ogawa A. Very early and standard Tc-99m ethyl cysteinate dimer SPECT imaging in a patient with reperfusion hyperemia after acute cerebral embolism. Clin Nucl Med. 2002a; 27:105–8. [PubMed: 11786739]

Ogasawara K, Ogawa A, Ezura M, Konno H, Doi M, Kuroda K, Yoshimoto T. Dynamic and static ^{99m}Tc-ECD SPECT imaging of subacute cerebral infarction: comparison with ^{133}Xe SPECT. J Nucl Med. 2001a; 42:543–7. [PubMed: 11337539]

Ogasawara K, Ogawa A, Koshu K, Konno H, Suzuki M, Yoshimoto T. Hypofixation and hyperfixation of ^{99m}Tc-hexamethyl propyleneamine oxime in subacute cerebral infarction. J Nucl Med. 2000; 41:795–9. [PubMed: 10809194]

Ogasawara K, Yasuda S, Beppu T, Kobayashi M, Doi M, Kuroda K, Ogawa A. Brain PET and technetium-99m-ECD SPECT imaging in Lhermitte-Duclos disease. Neuroradiology. 2001b; 43:993–6. [PubMed: 11760808]

Ogasawara K, Yasuda S, Yukawa H, Yamagata M, Kin M, Ogawa A. Atypical finding of brain Tc-99m-ECD SPECT imaging in herpes simplex encephalitis. Ann Nucl Med. 2002b; 5:347–50.

Okizakia A, Shuke N, Sato J, Sasaki T, Hasebe N, Kikuchi K, Aburano T. A compartment model analysis for investigation of myocardial fatty acid metabolism in patients with hypertrophic cardiomyopathy. Nucl Med Commun. 2007; 28:726–35. [PubMed: 17667752]

Onishi Y, Yonekura Y, Nishizawa S, Tanaka F, Okazawa H, Ishizu K, Fujita T, Konishi J, Mukai T. Noninvasive quantification of iodine-123-Iomazenil SPECT. J Nucl Med. 1996; 37:374–8. [PubMed: 8667079]

Ordonez C, Sheng J, Li Y, Chang W. Simulated imaging studies of C-SPECT/CT. J Nucl Med. 2008; 49(Suppl):407P.

Osher S, Fedkiw RP. Level set methods: an overview and some recent results. J Comput Phys. 1999; 169:463–502.

Osher S, Sethian J. Fronts propagation with curvature-dependent speed: algorithms based on Hamilton-Jacobi formulations. J Comput Phys. 1988; 79:12–49.

Patlak CS, Blasberg RG. Graphical evaluation of blood-to-brain transfer constants from multiple-time uptake data: generalizations. J Cereb Blood Flow Metab. 1985; 5:584–90. [PubMed: 4055928]

Patlak CS, Blasberg RG, Fenstermacher JD. Graphical evaluation of blood-to-brain transfer constants from multiple-time uptake data. J Cereb Blood Flow Metab. 1983; 3:1–7. [PubMed: 6822610]

Patton JA, Slomka PJ, Germano G, Berman DS. Recent technologic advances in nuclear cardiology. J Nucl Cardiol. 2007; 14:501–13. [PubMed: 17679058]

Penney BC, King MA, Knesaurek K. A projector, back-projector pair which accounts for the two-dimensional depth and distance dependent blurring in SPECT. IEEE Trans Nucl Sci. 1990; 37:681–86.

Peremans K, Cornelissen B, Van Den Bossche B, Audenaert K, Van de Wiele C. A review of small animal imaging planar and pinhole SPECT gamma camera imaging. Vet Radiol Ultrasound. 2005; 46:162–70. [PubMed: 15869162]

Phelps, ME.; Mazziotta, JC.; Schelbert, HR. Positron Emission Tomography and Autoradiography: Principles and Applications for the Brain and Heart. New York: Raven; 1986.

Pimlott SL, Ebmeier MA. SPECT imaging in dementia. Brit J Radiol. 2007; 80:S153–9. [PubMed: 18445745]

Pretorius PH, King MA, Tsui BMW, LaCroix KJ, Xia W. A mathematical model of motion of the heart for use in generating source and attenuation maps for simulating emission imaging. Med Phys. 1999; 26:2323–32. [PubMed: 10587213]

Qi J. A unified noise analysis for iterative image estimation. Phys Med Biol. 2003; 48:3505–19. [PubMed: 14653559]

Qi J, Leahy RM. Resolution and noise properties of MAP reconstruction for fully 3D PET. IEEE Trans Med Imaging. 2000; 19:493–506. [PubMed: 11021692]

Reich, JG. Kinetic Data Analysis: Design and Analysis of Enzyme and Pharmacokinetic Experiments. Endrenyi, L., editor. New York: Plenum; 1981. p. 39-60.

Resnick SM, Sojkova J, Zhou Y, An Y, Ye W, Holt DP, Dannals RF, Mathis CA, Klunk WE, Ferrucci L, Kraut MA, Wong DF. Longitudinal cognitive decline is associated with fibrillar amyloid-beta measured by [11C] PiB. Neurology. 2010; 74:807–15. [PubMed: 20147655]

Reutter, BW.; Gullberg, GT.; Boutchko, R.; Balakrishnan, K.; Botvinick, EH.; Huesman, RH. Fully 4-D dynamic cardiac SPECT image reconstruction using spatiotemporal B-spline voxelization. 2007 IEEE Nuclear Science Symp. and Medical Imaging Conf; Honolulu, HI. 2007a. p. 4217-21.

Reutter, BW.; Gullberg, GT.; Boutchko, R.; Balakrishnan, K.; Botvinick, EH.; Huesman, RH. Regularized least-squares SPECT image reconstruction using multiresolution spatial B-splines and a negativity penalty. 9th Int. Meeting on Fully Three-Dimensional Image Reconstruction in Radiology and Nuclear Medicine; Lindau, Germany. 2007b. p. 305-8.

Reutter BW, Gullberg GT, Huesman RH. Kinetic parameter estimation from attenuated SPECT projection measurements. IEEE Trans Nucl Sci. 1998a; 45:3007–13.

Reutter, BW.; Gullberg, GT.; Huesman, RH. Kinetic parameter estimation from dynamic cardiac patient SPECT projection measurements. 1998 IEEE Nuclear Science Symp. and Medical Imaging Conf. Record; Toronto, Ontario, Canada. 8–14 November; 1998b. p. 1953-8.

Reutter BW, Gullberg GT, Huesman RH. Direct least squares estimation of spatiotemporal distributions from dynamic SPECT projections using a spatial segmentation and temporal B-splines. IEEE Trans Med Imaging. 2000; 19:434–50. [PubMed: 11021687]

Reutter BW, Gullberg GT, Huesman RH. Effects of temporal modeling on the statistical uncertainty of spatiotemporal distributions estimated directly from dynamic cone-beam SPECT projections. Phys Med Biol. 2002; 47:2673–83. [PubMed: 12200931]

Reutter, BW.; Gullberg, GT.; Huesman, RH. Effects of scatter modeling on time-activity curves estimated directly from dynamic SPECT projections. 2003 IEEE Nuclear Science Symp. and Medical Imaging Conf. Record; Portland, OR. 19–25 October 2003; 2003.

Reutter BW, Gullberg GT, Huesman RH. Accuracy and precision of compartmental model parameters obtained from directly estimated dynamic SPECT time-activity curves. IEEE Trans Nucl Sci. 2004a; 51:170–6.

Reutter, BW.; Gullberg, GT.; Huesman, RH. Spatiotemporal scatter models for dynamic SPECT. Conf. Record of the 2004 IEEE Nuclear Science Symp. and Medical Imaging Conf; Rome, Italy. 2004b. p. 4092-6.

Reutter, BW.; Gullberg, GT.; Sitek, A.; Boutchko, R.; Botvinick, EH.; Huesman, RH. Modeling spatial smoothness in fully 3D SPECT image reconstruction using multiresolution B-splines. 2006 IEEE Nuclear Science Symp. and Medical Imaging Conf; San Diego, CA. 2006. p. 1757-61.

Reutter BW, Klein GJ, Huesman RH. Automated 3D segmentation of respiratory-gated PET transmission images. IEEE Trans Nucl Sci. 1997; 44:2473–6.

Reutter, BW.; Oh, S.; Gullberg, GT.; Huesman, RH. Improved quantitation of dynamic SPECT via fully 4D joint estimation of compartmental models and blood input function directly from projections. Conf. Record of the 2005 IEEE Nuclear Science Symp. and Medical Imaging Conf; Puerto Rico. 2005. p. 2337-41.

Riabkov DY, DiBella EVR. Blind identification of the kinetic parameters in three-compartment models. Phys Med Biol. 2004; 49:639–64. [PubMed: 15070194]

Rogers WL, Clinthorne NH, Shao L, Chiao P, Ding Y, Stamos JA, Koral KF. SPRINT II: a second-generation single photon ring tomograph. IEEE Trans Med Imaging. 1988; MI-7:291–7. [PubMed: 18230481]

Rogers WL, Linthorne NH, Stramos JA, Koral KF, Mayans R, Keyes JWJ, Williams JJ, Snapp WP, Knoll GF. SPRINT: a stationary detector single photon ring tomograph for brain imaging. IEEE Trans Med Imaging. 1982; MI-1:63–8. [PubMed: 18238259]

Rose CP, Goresky CA, Bach GG. The capillary and sarcolemmal barriers in the heart. Circ Res. 1977; 41:515–33. [PubMed: 902358]

Rosenspire KC, Rumsey WL, Jurisson S, Hirth W, Narra RK. [99mTc] teboroxime and [99mTc]Cl(DMG)3B2MP: binding characteristics and metabolism of two [99mTc]BATOs in blood and tissues. Nucl Med Biol. 1993; 20:395–400. [PubMed: 8504281]

Ross SG, Gullberg GT, Huesman RH. The effect of heart motion on kinetic parameter estimates for dynamic cardiac SPECT. IEEE Trans Nucl Sci. 1997a; 44:1409–16.

Ross SG, Welch A, Gullberg GT, Huesman RH. An investigation into the effect of input function shape and image acquisition interval on estimates of washin for dynamic cardiac SPECT. Phys Med Biol. 1997b; 42:2193–213. [PubMed: 9394407]

Rowe RK, Aarsvold JN, Barrett HH, Chen JC, Klein WP, Moore BA, Pang IR, Patton DD, White TA. A stationary hemispherical SPECT imager for three-dimensional brain imaging. J Nucl Med. 1993; 34:474–80. [PubMed: 8441043]

Rowe, RK.; Aarsvold, JN.; Barrett, HH.; Chen, J.; Hall, JN.; Landesman, AL.; Mar, LS.; Milster, TD.; Moore, BA.; Patton, DD.; Roney, TJ. The design and implementation of modular SPECT imaging systems. In: Todd-Pokropek, A.; Viergever, MA., editors. Medical Images: Formation, Handling and Evaluation(NATO-ASI Series F. Vol. 98. Portugal: Springer; 1992.

Rudzinski W, Swiat M, Tomaszewski M, Krejza J. Cerebral hemodynamics and investigation of cerebral blood flow regulation. Nucl Med Rev. 2007; 10:29–42.

Rumsey WL, Rosenspire KC, Nunn AD. Myocardial extraction of teboroxime: effects of teboroxime interaction with blood. J Nucl Med. 1992; 33:94–101. [PubMed: 1530970]

Sakaji K, Akiyama M, Umeda H, Nakazawa Y, Takenaka H, Shinozuka A. Lung function assessment using Xe-133 dynamic SPECT in dual-camera system. Japan J Radiol Technol. 2001; 57:1138–44.

Seibyl JP. Single-photon emission computed tomography and positron emission tomography evaluations of patients with central motor disorders. Semin Nucl Med. 2008; 38:274–86. [PubMed: 18514083]

Seike Y, Hashikawa K, Oku N, Moriwaki H, Yamamoto H, Fukuchi K, Watanabe Y, Matsumoto M, Hori M, Nishimura T. Evaluation of the use of a standard input function for compartment analysis of [123]imomazenil data: factors influencing the quantitative results. Ann Nucl Med. 2004; 18:563–72. [PubMed: 15586629]

Sethian, J. Level Set Methods: Evolving Interface in Geometry, Fluid Mechanics, Computer Vision and Material Science. Cambridge, MA: Cambridge University Press; 1996.

Sharir T, Ben-Haim S, Merzon K, Prochorov V, Dickman D, Ben-Haim S, Berman DS. High-speed myocardial perfusion imaging: initial clinical comparison with conventional dual detector Anger camera imaging. J Am Coll Cardiol Imaging. 2008; 1:156–63.

Sharir T, Merzon K, Prochorov V, Dickman D, Nir Y, Ben Haim S, Berman D. D-SPECT: high speed myocardial perfusion imaging: a comparison with dual detector Anger camera (A-SPECT). J Nucl Med. 2007; 48:51.

Sharir T, Slomka PJ, Hayes SW, DiCarti MF, Ziffer JA, Martin WH, Dickman D, Ben-Haim S, Berman DS. Multicenter trial of high-speed versus conventional single-photon emission computed tomography imaging quantitative results of myocardial perfusion and left ventricular function. J Am Coll Cardiol. 2010; 55:1965–74. [PubMed: 20430269]

Shi Y, Karl WC. Tomographic reconstruction of dynamic objects. Proc SPIE. 2003; 5016:151–60.

Shi, Y.; Karl, WC. Level set methods for dynamic tomography. 2004 IEEE Int. Symp. on Biomedical Imaging: Macro to Nano; Washington, DC. 15–18 April 2004; 2004. p. 620-3.

Sitek A, Di Bella EVR, Gullberg GT. Factor analysis of dynamic structures in dynamic SPECT imaging using maximum entropy. IEEE Trans Nucl Sci. 1999a; 46:2227–32.

Sitek, A.; Di Bella, EVR.; Gullberg, GT. Lecture Notes in Computer Science. Kuba, A., et al., editors. New York: Springer; 1999b. p. 436-41.

Sitek A, Di Bella EVR, Gullberg GT. Factor analysis with a priori knowledge–application in dynamic cardiac SPECT. Phys Med Biol. 2000; 45:2619–38. [PubMed: 11008961]

Sitek A, Di Bella EVR, Gullberg GT, Huesman RH. Removal of liver activity contamination in teboroxime dynamic cardiac SPECT imaging using factor analysis. J Nucl Cardiol. 2002a; 9:197–205. [PubMed: 11986565]

Sitek A, Gullberg GT, Di Bella EVR, Celler A. Reconstruction of dynamic renal tomographic data acquired by slow rotation. J Nucl Med. 2001; 42:1704–12. [PubMed: 11696643]

Sitek A, Gullberg GT, Huesman RH. Correction for ambiguous solutions in factor analysis using a penalized least squares objective. IEEE Trans Med Imaging. 2002b; 21:216–25. [PubMed: 11989846]

Sitek A, Huesman RH, Gullberg GT. Tomographic reconstruction using an adaptive tetrahedral mesh defined by a point cloud. IEEE Trans Med Imaging. 2006; 25:1172–9. [PubMed: 16967802]

Sitek A, Klein GJ, Gullberg GT, Huesman RH. Deformable model of the heart with fiber structure. IEEE Trans Nucl Sci. 2002c; 49:789–93.

Sitek, A.; Klein, GJ.; Reutter, BW.; Huesman, RH.; Gullberg, GT. Measurement of the biomechanics of 3D cardiac function with gated nuclear medicine studies. Conf. Record of the 2005 IEEE Nuclear Science Symp. and Medical Imaging Conf; San Juan, Puerto Rico. 2005. p. 2346-9.

Smith AM, Gullberg GT, Christian PE. Experimental verification of technetium 99m-labled teboroxime kinetic parameters in the myocardium with dynamic single-photon emission computed tomography: reproducibility, correlation to flow, and susceptibility to extravascular contamination. J Nucl Cardiol. 1996; 3:130–42. [PubMed: 8799238]

Smith AM, Gullberg GT, Christian PE, Datz L. Kinetic modeling of teboroxime using dynamic SPECT imaging of a canine model. J Nucl Med. 1994; 35:484–95. [PubMed: 8113904]

Stayman JW, Fessler JA. Regularization for uniform spatial resolution properties in penalized-likelihood image reconstruction. IEEE Trans Med Imaging. 2000; 19:601–15. [PubMed: 11026463]

Stewart J. GN Researches on the circulation time and on the influences which affect it: IV. The output of the heart. Physiology. 1897; 22:159–83.

Stewart RE, Schwaiger M, Hutchins GD, Chiao P-C, Gallagher KP, Nguyen N, Petry NA, Rogers WL. Myocardial clearance kinetics of technetium-99m-SQ30217: a marker of regional myocardial blood flow. J Nucl Med. 1990; 31:1183–90. [PubMed: 2362197]

Stoddart HF, Stoddart HA. A new development in single gamma transaxial tomography Union Carbide focused collimator scanner. IEEE Trans Nucl Sci. 1979; NS-26:2710.

Stokely EM, Sveinsdottir E, Lassen NA, Rommer P. A single photon dynamic computer assisted tomograph (DCAT) for imaging brain function in multiple cross sections. J Comput Assist Tomog. 1980; 4:230–40.

Su Y, Welch MJ, Shoghi KI. The application of maximum likelihood factor analysis (MLFA) with uniqueness constraints on dynamic cardiac microPET data. Phys Med Biol. 2007; 52:2313–34. [PubMed: 17404471]

Sugihara H, Yonekura Y, Kataoka K, Fukai D, Kitamura N, Taniguchi Y. Estimation of coronary flow reserve with the use of dynamic planar and SPECT images of Tc-99m tetrofosmin. J Nucl Cardiol. 2001; 8:575–9. [PubMed: 11593222]

Takeishi YY, Arimoto T, Kubota I. Dynamic I-123 MIBG SPECT reflects sympathetic nervous integrity and predicts clinical outcome in patients with chronic heart failure (abstract). J Nucl Cardiol. 2005; 12:S6.

Tan K, Hutton BF, Feng D. A new approach for parameter estimation in SPECT dynamic using a rotating camera (abstract). Eur J Nucl Med. 1994; 21:S29.

Taylor, JR. An Introduction to Error Analysis—The Study of Uncertainties in Physical Measurements. Oxford: Oxford University Press; 1982.

Toennies, KD.; Celler, A.; Blinder, S.; Moeller, T.; Harrop, R. Scatter segmentation in dynamic SPECT images using principal component analysis. SPIE Medical Imaging 2003; San Diego, CA. 2003.

Toennies, KD.; Prang, C.; Celler, A. Local identification and removal of scatter artefacts based on the temporal information in dynamic SPECT images. Cambridge 17th Int. Conf on Pattern Recognition; 2004; Cambridge. 2004.

Toyama H, et al. Evaluation of the clinical usefulness of super dynamic ^{99m}Tc-HM-PAO SPECT in ischemic cerebral vascular disease—detection of hypo- and hyperperfusion area (article in Japanese). Kaku Iqaku. 1996; 33:521–9.

Tsuchida T, Yonekura Y, Sadato M, Takahashi N, Yamamoto H, Ishii Y. Prediction of improvement of cerebral perfusion with I-123 iomazenil SPECT. Ann Nucl Med. 1999; 13:265–8. [PubMed: 10510884]

Tsui BMW, Hu HB, Gilland DR, Gullberg GT. Implementation of simultaneous attenuation and detector response correction in SPECT. IEEE Trans Nucl Sci. 1988; 35:778–83.

Tsui BMW, Terry JA, Gullberg GT. Evaluation of cardiac cone-beam single photon emission computed tomography using observer performance experiments and receiver operating characteristic analysis. Invest Radiol. 1993; 28:1101–12. [PubMed: 8307713]

van Elmbt L, Walrand S. Simultaneous correction of attenuation and distance-dependent resolution in SPECT: an analytical approach. Phys Med Biol. 1993; 38:1207–17.

Vanzi E, Formiconi AR, Bindi D, La Cava G, Pupi A. Kinetic parameter estimation from renal measurements with a three-headed SPECT system: a simulation study. IEEE Trans Med Imaging. 2004; 23:363–73. [PubMed: 15027529]

Vastenhouw B, Beekman F. Submillimeter total-body murine imaging with U-SPECT-I. J Nucl Med. 2007; 48:487–93. [PubMed: 17332628]

Veress AI, Gullberg GT, Weiss JA. Measurement of strain in the left ventricle during diastole with cine-MRI and deformable image registration. J Biomech Eng. 2005; 127:1195–207. [PubMed: 16502662]

Verger L, Gentet M, Gerfault L, Guillemaud R, Mestais C, Monnet O, Montemont G, Petroz G, Rostaing JP, Rustique J. Performance and perspective of CdZnTe-based gamma camera for medical imaging. IEEE Trans Nucl Sci. 2004; 51:3111–7.

Volkow ND, Fowler JS, Wang GJ. Positron emission tomography and single-photon emission computed tomography in substance abuse research. Semin Nucl Med. 2003; 33:114–28. [PubMed: 12756644]

Volkow ND, Fowler JS, Wang GJ, Baler R, Telang F. Imaging dopamine's role in drug abuse and addiction. Neuropharmacology. 2009; 56(Suppl 1):3–8. [PubMed: 18617195]

Volokh L, Lahat C, Beilin L, Hugg J, Blevis I, Jansen FP, Shai E, Hasegawa BH. Initial performance evaluation of an ultra-fast cardiac SPECT camera—a phantom study (abstract). J Nucl Cardiol. 2008; 15:S5.

Wagner, HN., Jr; Szabo, Z.; Buchanan, JW., editors. Principles of Nuclear Medicine. 2. Philadelphia: Saunders; 1995.

Wallin A. Constructing surfaces from CT data. IEEE Comput Graph Appl. 1991; 11:28–33.

Wang G, Fu L, Qi J. Maximum a posteriori reconstruction of Patlak parametric image from sinograms in dynamic PET. Phys Med Biol. 2008; 53:593–604. [PubMed: 18199904]

Wang W, Gindi G. Noise analysis of MAP-EM algorithms for ECT. Phys Med Biol. 1997; 42:2215–32. [PubMed: 9394408]

Weber DA, Ivanovic M. Ultra-high-resolution imaging of small animals: implications for preclinical and research studies. J Nucl Cardiol. 1999; 6:332–4. [PubMed: 10385189]

Weissleder R, Mahmod U. Molecular imaging. Radiology. 2001; 219:316–33. [PubMed: 11323453]

Welch A, Gullberg GT, Christian PE, Datz FL, Morgan HT. A transmission-map-based scatter correction technique for SPECT in inhomogeneous media. Med Phys. 1995a; 22:1627–35. [PubMed: 8551987]

Welch A, Smith AM, Gullberg GT. An investigation of the effect of finite system resolution and photon noise on the bias and precision of dynamic cardiac SPECT parameters. Med Phys. 1995b; 22:1829–36. [PubMed: 8587537]

Wells RG, Farncombe T, Chang E, Nicholson RL. Reducing bladder artifacts in clinical pelvic SPECT images. J Nucl Med. 2004; 45:1309–14. [PubMed: 15299054]

Williams KA, Taillon LAJ. Reversible ischemia in severe stress technetium 99m-labeled sestamibi perfusion defects assessed from gated single-photon emission computed tomographic polar map Fourier analysis. Nucl Cardiol. 1995; 2:199–206.

Wolfe N, Reed BR, Eberling JL, Jagust WJ. Temporal lobe perfusion on single photon emission computed tomography predicts the rate of cognitive decline in Alzheimer's disease. Archives of Neurology. 1995; 52:257–62. [PubMed: 7872878]

Yonekura Y, Senda M, Fujita T, Hirose Y, Tanada S, Tamaki N, Mukai T, Yamamoto K, Torizuka K. System design and performance characteristics of newly developed whole-body multislice single photon emission computed tomograph (abstract). J Nucl Med. 1985; 26:11.

Zar, JH. Biostatistical Analysis. Englewood Cliffs, NJ: Prentice-Hall; 1984.

Zeng GL, Bai C, Gullberg GT. A projector/backprojector with slice-to-slice blurring for efficient 3D scatter modeling. IEEE Trans Med Imaging. 1999; 18:722–32. [PubMed: 10534054]

Zeng GL, Gullberg GT, Huesman RH. Using linear time-invariant system theory to estimate kinetic parameters directly from projection measurements. IEEE Trans Nucl Sci. 1995; 42:2339–46.

Zeng GL, Gullberg GT, Tsui BMW, Terry JA. Three-dimensional iterative reconstruction algorithms with attenuation and geometric point response correction. IEEE Trans Nucl Sci. 1991; 38:693–702.

Zeng GL, Hsieh Y-L, Gullberg GT. A rotating and warping projector-backprojector pair for fan-beam and cone-beam iterative algorithms. IEEE Trans Nucl Sci. 1994; 41:2807–11.

Zeniya T, et al. Use of a compact pixellated gamma camera for small animal pinhole SPECT imaging. Ann Nucl Med. 2006; 20:409–16. [PubMed: 16922469]

Zhou R, Thomas DH, Qiao H, Bal HS, Choi SR, Alavi A, Ferrari VA, Kung HF, Acton PD. *In vivo*detection of stem cells grafted in infarcted rat myocardium. J Nucl Med. 2005; 46:816–22. [PubMed: 15872356]

Zierler KL. Equations for measuring blood flow by external monitoring of radioisotopes. Circ Res. 1965; 16:309–21. [PubMed: 14270567]

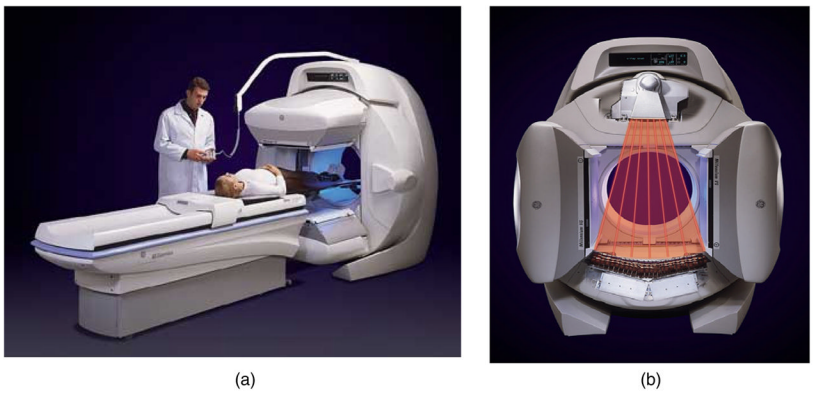

(a) (b)

Figure 1.

SPECT/CT camera manufactured by GE Healthcare (Haifa, Israel) (image from GE Healthcare with permission). (a) The system is composed of two large field-of-view gamma ray detectors and (b) an x-ray CT system. Photons that should be counted by the detector but are not (due to scatter or absorption by the tissue) are stated to be attenuated. Photons that travel further through tissue will have a higher likelihood of being attenuated. Information from the CT image is used to correct for the attenuation and to provide information about scatter to obtain a better estimate of the quantitative distribution of the injected radioisotope.

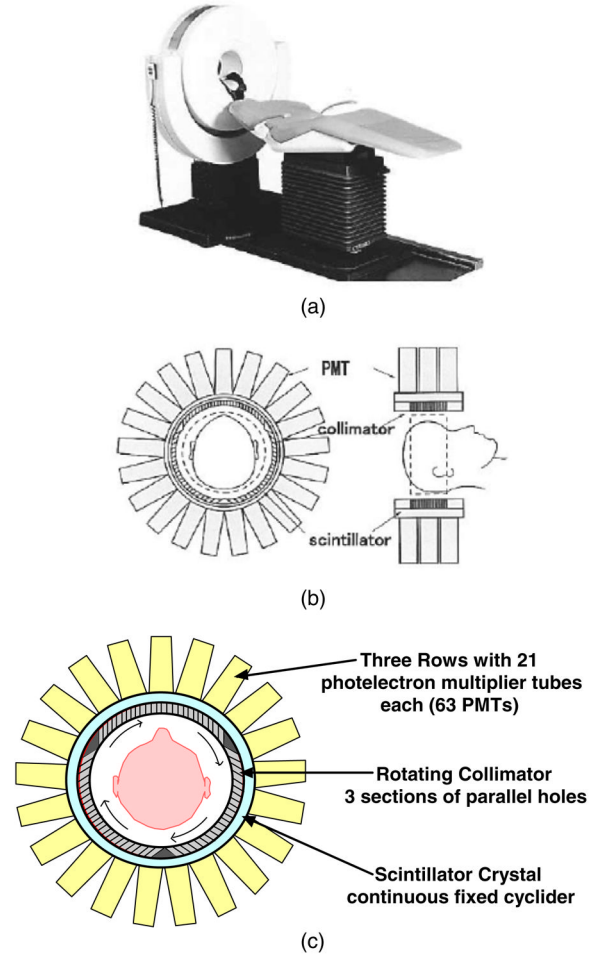

Figure 2.

The CERASPECT dedicated brain system was manufactured by DSI, Inc. (Waltham, MA). (a) Picture of the scanner with patient bed. (b) Drawing illustrating the collimator, scintillator, and PMTs (from figure 1 of Komatani *et al* (2004), with permission). (c) Diagram of camera detector redrawn to better illustrate the arrangement of the collimator holes in the rotating collimator.

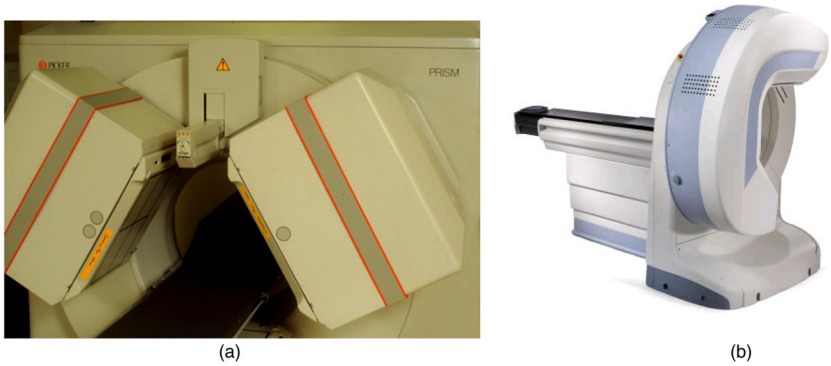

Figure 3.

(a) Triple-headed SPECT system manufactured by Picker (Cleveland, OH). The system consists of an external line source of radioactivity (^{153}Gd) used to obtain a transmission image used for attenuation correction. (b) Dedicated cardiac SPECT system manufactured by GE Healthcare (Discovery NM 530c, GE Healthcare, Haifa, Israel) (image from GE Healthcare with permission). The system consists of a half ring of CZT detectors.

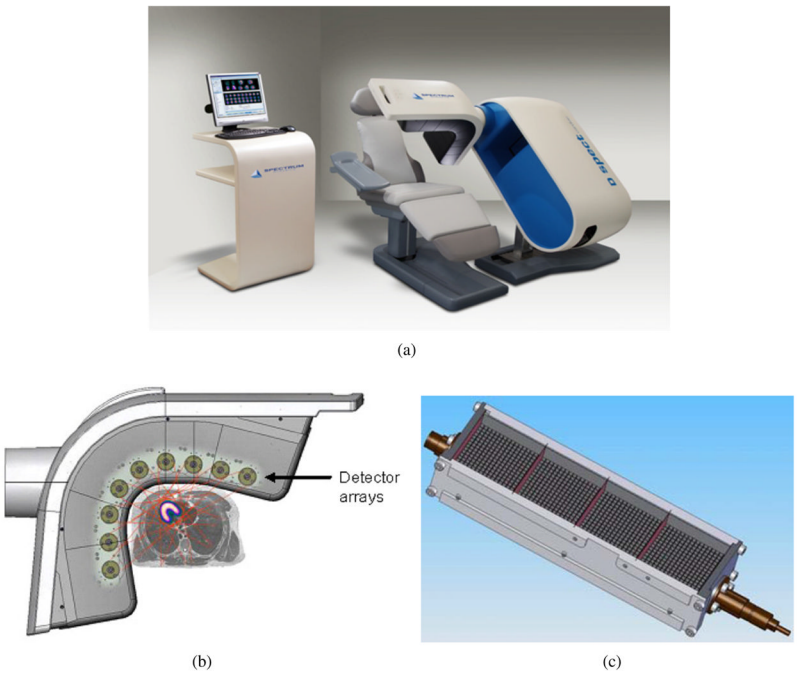

Figure 4.

(a) Dedicated cardiac SPECT camera manufactured by Spectrum Dynamics (Caesarea, Israel) (image from Spectrum Dynamics with permission). (b) The camera consists of nine pixellated cadmium zinc telluride (CZT) detector arrays mounted in a vertical column, each rotating in synchrony and acquiring at multiple angles as the detectors are swept through the imaging field of view (image from figure 1 of Erlandsson *et al* (2009) with permission). (c) Each detector column consists of an array of 16 × 64 CZT semi-conductor elements (2.46 × 2.46 × 5 mm), collimated by a parallel-hole tungsten collimator with a hole size of 2.46 × 2.46 mm, the same as a detector element (Patton *et al* 2007). The collimator hole length is shorter than the LEHR collimator with a significant gain in sensitivity. The cadmium zinc telluride provides improved energy resolution and image contrast. The improved geometric sensitivity allows for myocardial perfusion imaging studies of 2 min stress and 4 min rest acquisition times. Reconstruction is performed with a proprietary version of an OSEM-based reconstruction software package developed and implemented by Spectrum Dynamics (image from Spectrum Dynamics with permission).

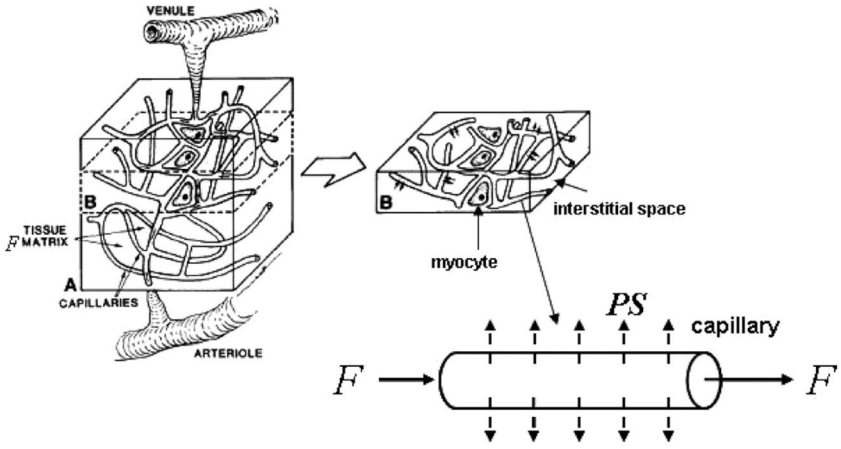

Figure 5.

Intravascular blood and extravascular compartments. The intravascular blood compartment is the arteries and capillaries, and the extravascular compartment contains the physical space occupied by myocytes and interstitial space. The blood compartment contains plasma and blood cells. The models presented in this review assume that the tracers exchange between the extravascular spaces and the plasma in the blood in the arteries and capillaries. The models also assume in most cases that the tracers in the blood are in equilibrium between the plasma and the blood cells (see section 2.3).

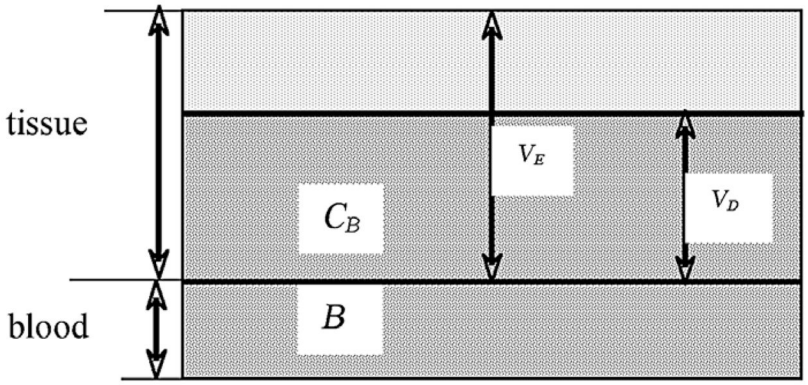

Figure 6.
Distribution volume. The distribution volume V_D is the volume of the extravascular space that would give the same tracer concentration as that in the blood. The partition coefficient λ is the ratio of the concentration in the blood to that in the extravascular space at equilibrium. The distribution volume is generally given the same value as the partition coefficient, as K_1/k_2. (The figure is adapted from figure 20-2 of Cherry *et al* (2003) with permission.)

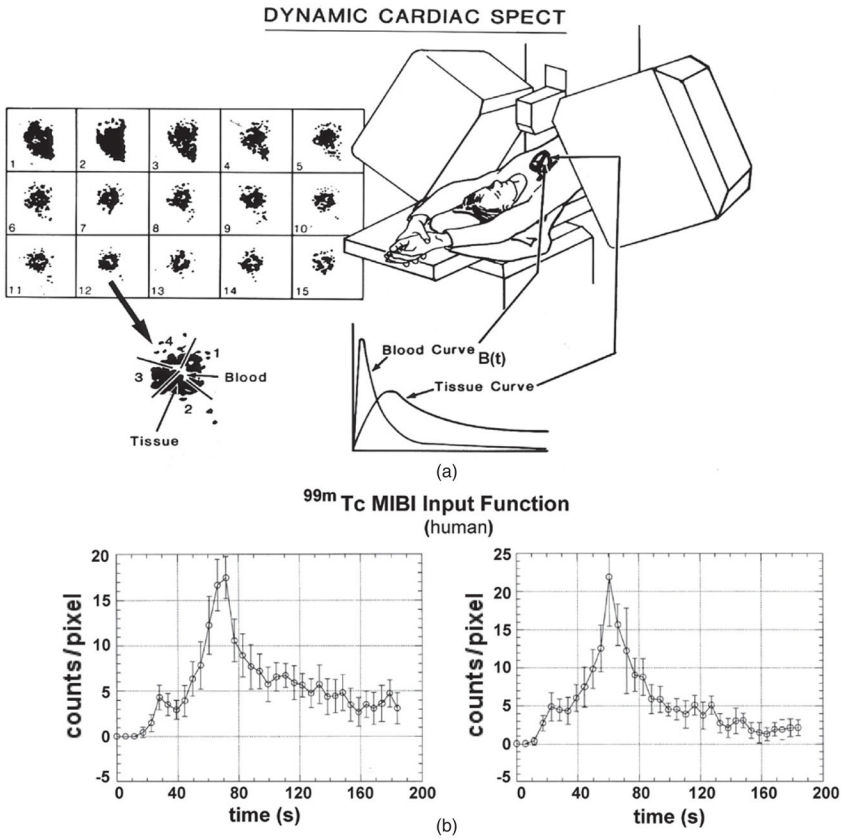

Figure 7.

(a) Concept of dynamic cardiac SPECT imaging using a fast-rotating detector system. Here, projections are acquired rapidly in order to reconstruct a dynamic sequence of 3D data acquisitions, each one acquired for 5 s. Regions of interest (ROIs) in the 3D reconstructed images are identified for blood and tissue, and curves for these regions are extracted. These curves are fitted to a one-compartment model. (b) Actual time activity curves generated from a dynamic sequence of 5 s reconstructions (Budinger *et al* 1991). The plot on the left is for an ROI in the left ventricle and the plot on the right is for an ROI in the atrium.

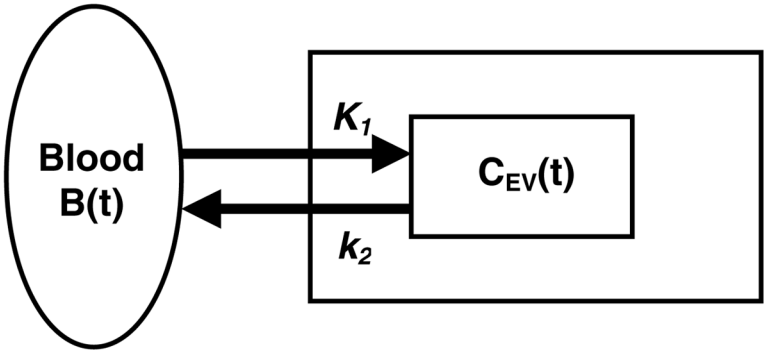

Figure 8.
One-compartment model. The blood is not a separate compartment because it is assumed to be a known quantity. K_1 is the wash-in rate constant (flow times extraction) and k_2 is the wash-out rate constant.

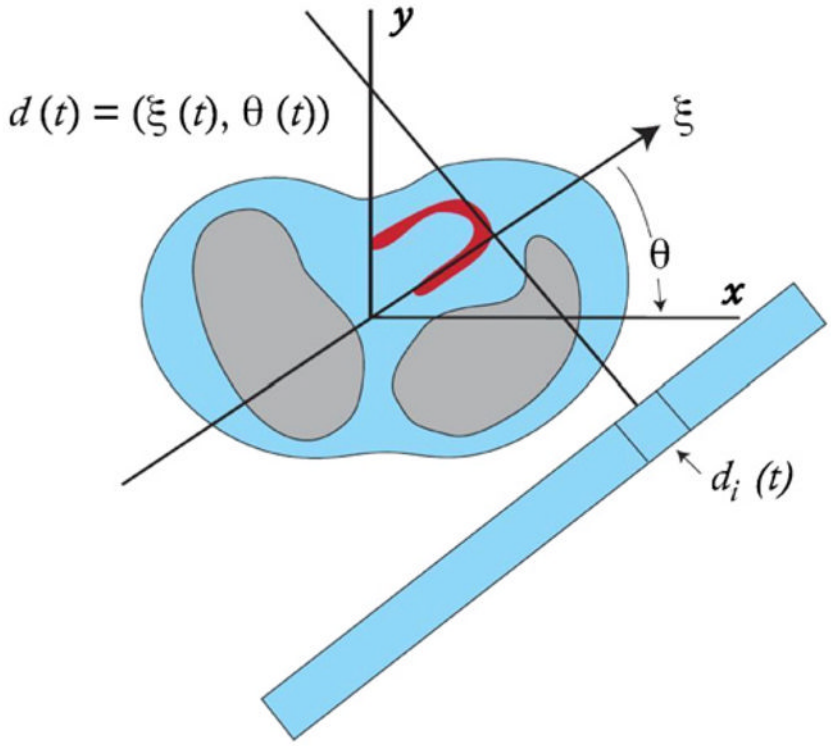

Figure 9.
The SPECT detector head is assumed to rotate continuously so that the detector coordinate $d(t)$ has a particular angle $\theta(t)$ and spatial coordinate $\xi(t)$. The projection measurements $p_i(t_k)$ are the activity acquired over a time period $t_k - \Delta t_k$ to t_k for the detector bin $d_i(t)$.

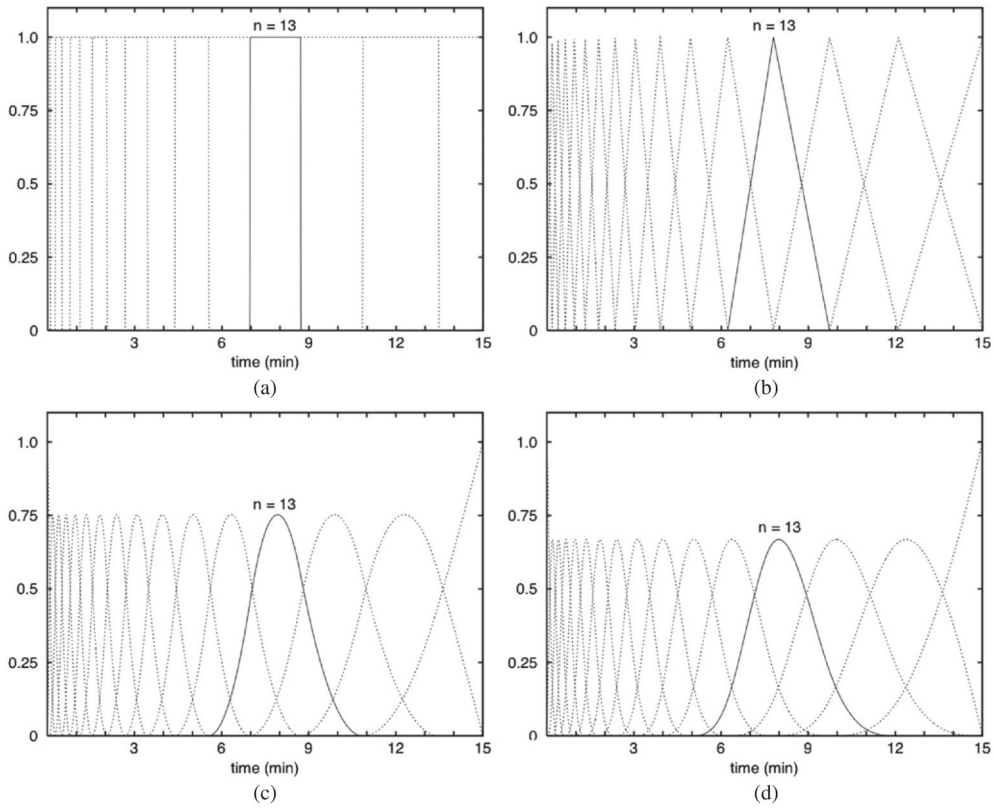

Figure 10.

Examples of piecewise (a) constant, (b) linear, (c) quadratic and (d) cubic B-spline basis functions. Sixteen splines were used to span 15 time segments that have geometrically increasing lengths. The 13th spline is shown as a solid curve. The initial time segment length for the splines shown here is 10 s.

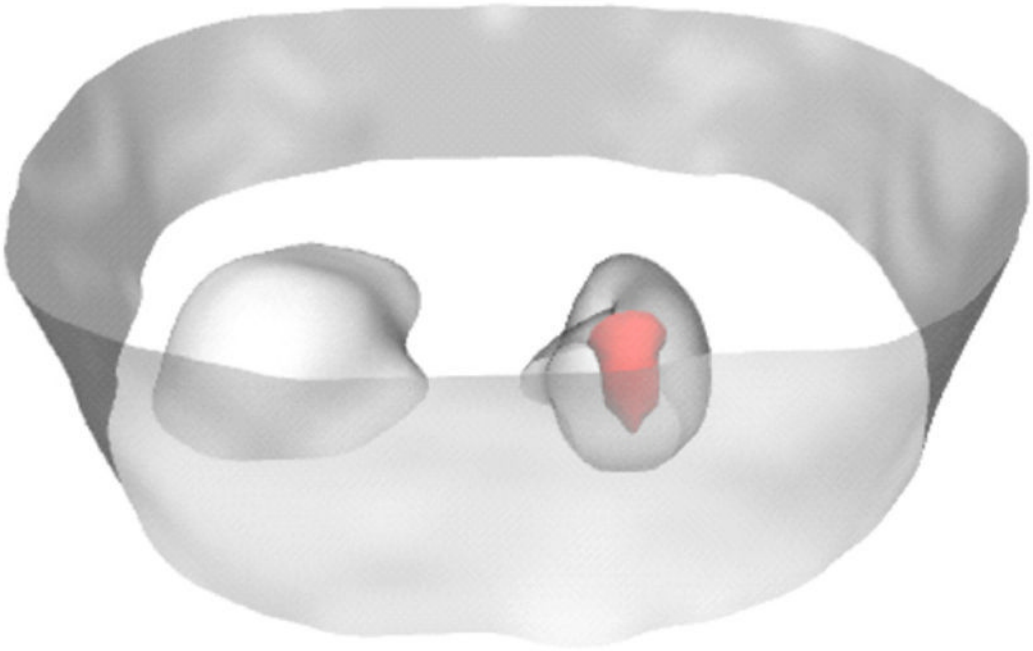

Figure 11.
Segmentation of heart, blood pool (red), liver and torso from a dynamic cardiac SPECT study using ^{99m}Tc-teboroxime (Reutter *et al* 1998b). Attenuation-corrected emission results were reconstructed using 20 iterations of the ML-EM algorithm. A 4D second directional derivative operator was applied to the attenuation-corrected dynamic image data set containing ninety 10 s frames to segment the regions of the myocardial tissue, intraventricular blood and background tissue. Shown here is the segmentation at time frame 31 (corresponding to the interval 300–310 s) after injection.

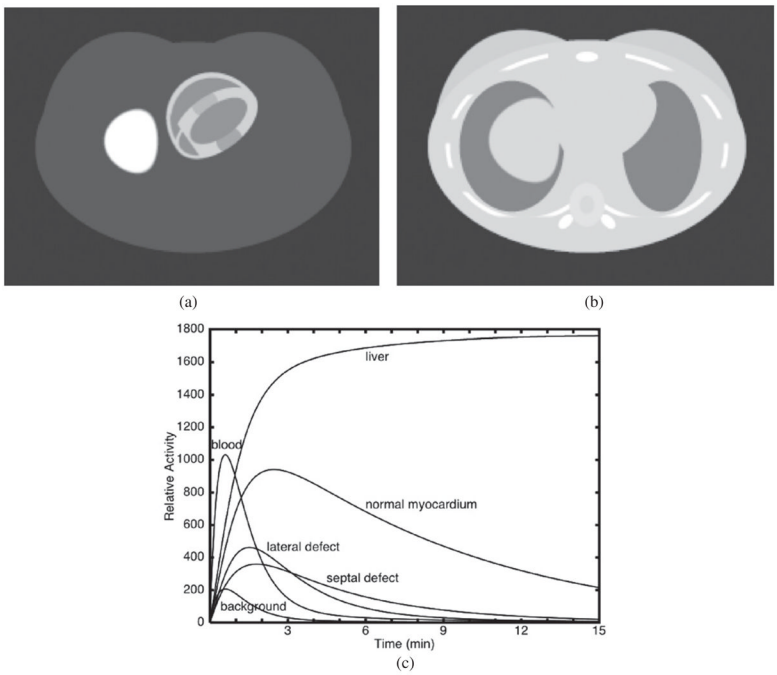

Figure 12.

Phantom and time–activity curves used in computer simulations comparing conventional, semi-direct and direct methods of estimation of kinetic parameters. (a) The MCAT emission phantom shown with lateral and septal defects. (b) The attenuator assumed in generating the projection data. (c) Time–activity curves used to generate the dynamic emission data for different organs. The myocardial tissue curves were generated assuming a one-compartment model (figure 8).

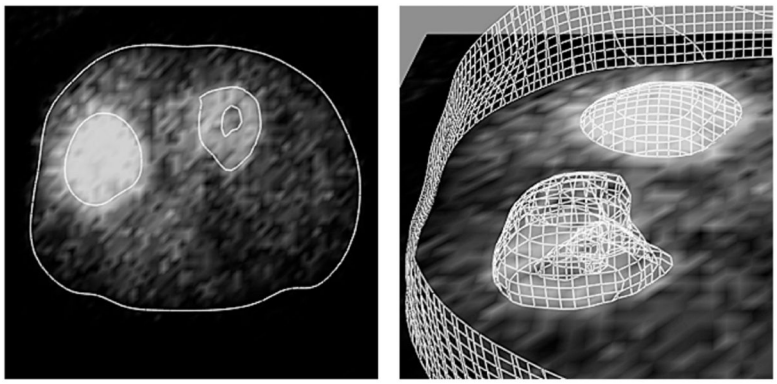

Figure 13.

Segmentation of a patient study (fast rotation) used in modeling the projection data for estimating the dynamic parameters directly from projections. The image on the left shows the boundaries of the liver (left) and the myocardium (right) resulting from the automatic segmentation of the attenuation-corrected reconstruction at time frame 31 of the sequence of dynamic reconstructions. The image on the right shows anatomical surfaces of the dome of the liver (upper) and myocardium (lower), which were constructed by linking together zero-crossings of the second directional derivative (Reutter *et al* 1998b).

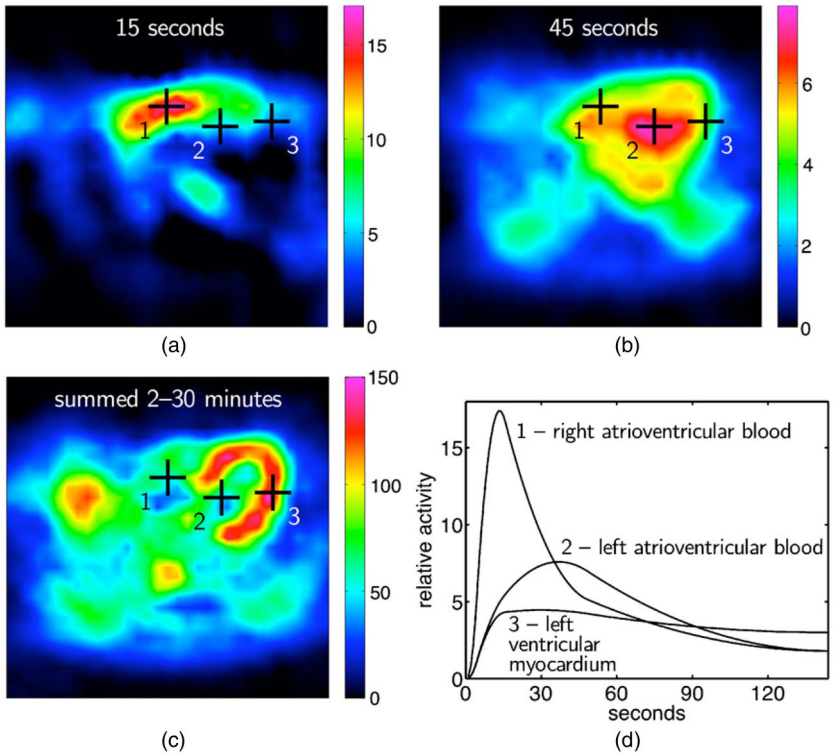

Figure 14.

Estimation of time–activity curves from projections acquired with slow camera rotation (patient study, slow rotation). Reconstructed images and time–activity curves for a human dynamic Tc-99m-sestamibi cardiac SPECT study. Kinetics of tracer in blood and myocardium are evident in fully 4D reconstructed dynamic images sampled at (a) 15 s and (b) 45 s; (c) in late summed image and (d) in directly estimated quadratic B-spline time–activity curves. Black crosses in (a)–(c) denote spatial positions at which time–activity curves were obtained (Reutter *et al* 2007a).

(a)

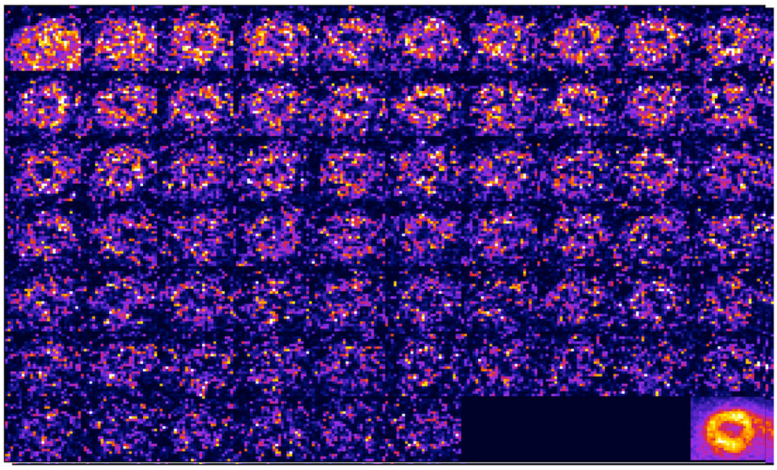

(b)

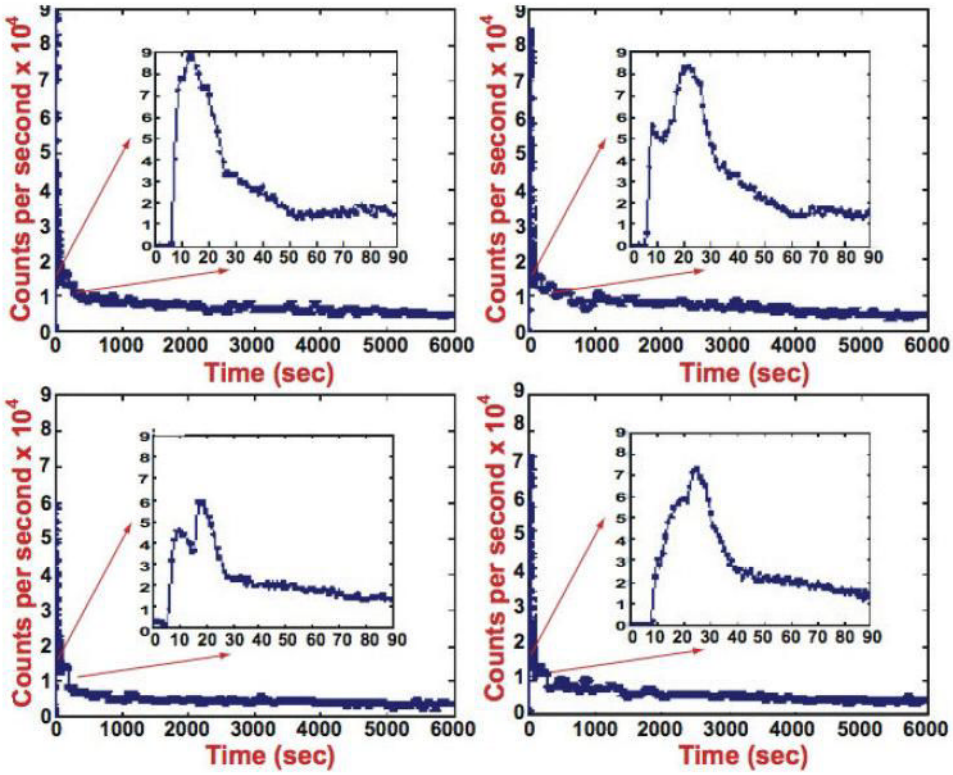

Figure 15.

Input functions of factors estimated from projections (rat study, slow rotation). (a) Pinhole collimators (tungsten insert with 1.5 mm aperture, 25 cm focal length with a magnification of approximately 5) mounted on the GE Millennium VG3 Hawkeye SPECT-CT system used in the rat studies. The camera rotated continuously with a pinhole to rotation axis distance of between 5.5 and 5.8 cm. (b) Sequence of dynamic reconstructions and reconstruction of the sum of all of the projections after the first 180 s for one transaxial slice of a rat study. (c) Input functions estimated by factor analysis for four ^{123}I-MIBG studies in rats using two factors. The curves are the convolution of the input injection (5 s) with the circulation function. The double peaks are due to a fast recirculation time of 6–8 s (Hu *et al* 2008).

Table 1

Estimates of myocardial uptake and wash-out parameters and volume fraction f_v of blood in the tissue obtained using conventional and direct compartmental model parameter estimation from projections, as well as results of fitting compartmental models to directly estimated spline time–activity curves (the semi-direct method). These are compared with the truth used in the simulations (Reutter *et al* 1998a, 2000).

	Parameter	Truth	Conventional	Direct	Semi-direct
Normal myocardium	K_1	0.700	0.665	0.700	0.700
	k_2	0.150	0.149	0.150	0.150
	f_v	0.150	0.160	0.150	0.151
Lateral defect	K_1	0.500	0.218	0.500	0.507
	k_2	0.600	0.247	0.600	0.607
	f_v	0.100	0.278	0.100	0.092

Units for K_1 and k_2 are in min^{-1}; f_v is dimensionless.

Table 2

Estimates of myocardial uptake and wash-out parameters and their uncertainties obtained using direct compartmental model parameter estimation from projections, as well as results of fitting compartmental models to directly estimated spline time–activity curves (the semi-direct method) (Reutter *et al* 1998b).

	Parameter	Direct	Error	Semi-direct	Error[a]
Myocardium	K_1	0.835	0.055	0.852	–
	k_2	0.178	0.002	0.172	–

Units are in min^{-1}. The errors for the direct method were estimated as twice the inverse of the Hessian matrix associated with the chi-square criterion in equation (52), where the weights were assumed to be the reciprocal of the measured projections.

[a]The issue of estimating errors using spline curves is complicated because the curves are correlated in time, so this remains an unsolved problem. This example illustrates why direct estimation of kinetic compartment model parameters is much more desirable.

Table 3

Comparison of sample means and sample standard deviations of compartmental model parameters estimated semi-directly and directly with joint estimation of the blood input function. The means and standard deviations were estimated from 400 noise realizations. The standard error of the sample mean is approximately 0.05 times the sample standard deviation. Units for the wash-in rate K_1^m and wash-out rate k_2^m are min^{-1}; the vascular fraction f_v^m is dimensionless (Reutter *et al* 2005).

	Parameter	Truth	Semi-direct (mean ± SD)	Direct joint (mean ± SD)
Normal myocardium	K_1^3	0.7	0.7001 ± 0.0061	0.6998 ± 0.0056
	k_2^3	0.15	0.1500 ± 0.0016	0.1499 ± 0.0016
	f_v^3	0.15	0.1501 ± 0.0121	0.1511 ± 0.0097
Septal defect	K_1^4	0.3	0.314 ± 0.077	0.312 ± 0.061
	k_2^4	0.3	0.311 ± 0.064	0.310 ± 0.053
	f_v^4	0.1	0.100 ± 0.119	0.097 ± 0.081
Lateral defect	K_1^4	0.5	0.554 ± 0.222	0.514 ± 0.132
	k_2^5	0.6	0.639 ± 0.172	0.616 ± 0.120
	f_v^5	0.1	0.075 ± 0.162	0.100 ± 0.102
Liver	K_1^6	0.9	0.9001 ± 0.0050	0.9001 ± 0.0049
	k_2^6	0.002	0.0020 ± 0.0004	0.0020 ± 0.0004
	f_v^6	0.2	0.2001 ± 0.0046	0.2002 ± 0.0036

Table 4

Estimates of the kinetic model parameters for a one-compartment model using the input functions in figure 15(c). The data were acquired on 29 November 2005 (Hu *et al* 2008).

Animal identifier	Kinetic parameters	Mean	Standard deviation
G1 normal	K_1 (s^{-1})	7.15×10^{-3}	6.37×10^{-4}
	k_2 (s^{-1})	2.64×10^{-3}	2.53×10^{-4}
G1 hypertensive	K_1 (s^{-1})	6.74×10^{-3}	7.24×10^{-4}
	k_2 (s^{-1})	3.44×10^{-3}	3.92×10^{-4}
G2 normal	K_1 (s^{-1})	7.41×10^{-3}	7.21×10^{-4}
	k_2 (s^{-1})	2.48×10^{-3}	2.60×10^{-4}
G2 hypertensive	K_1 (s^{-1})	5.52×10^{-3}	5.55×10^{-4}
	k_2 (s^{-1})	2.96×10^{-3}	2.78×10^{-4}